OBLIQUE WING REMOTELY PILOTED RESEARCH AIRCRAFT

FINAL REPORT

VOLUME I - DEVELOPMENT

NAS 2-7211 CR 114723

April 1974

TABLE OF CONTENTS

1. INTRODUCTION 1

1. All Wing Configuration 1

2. Yawed Wing 2

3. Plastic Material 2

4. Crash Survivable/Repairable 2

5. Payload - 160 lbs. 3

6. Giballed T.V. System With Wide Angle and Zoom Lens 3

7. Parachute Recovery Capability 3

8. Autopilot 3

9. Ducted Prop 3

10. Catapult Launch 4

PROJECT ORGANIZATION 5

TABLE I 6

2. VEHICLE CONFIGURATION AND AERODYNAMICS 8

2.1 Configuration 8
2.2 Aerodynamics 11

2.2.1 Theoretical Analysis 11
2.2.2 Wind Tunnel Tests 14

TABLE II 15

2.2.3 Glider Tests 32
2.2.4 Final Configuration Aerodynamics 33

TABLE III 35

2.2.5 Flying Without A Horizontal Tail 42

3. AVIONICS 43

TABLE IV 43

3.1 Airborne System 44

3.1.1 Command Package 44

TABLE V 45

TABLE VI 46

3.1.2 Electrical 52
3.1.3 Instrument Package and Nose Camera 53
3.1.4 Control Logic Summary 54

TABLE VII 55

3.2 Ground Equipment 55

3.2.1 Command Control 55
3.2.2 Video Display 57
3.2.3 Tracking System 58

4. PROPULSION 59

TABLE VIII 60

TABLE IX 61

5. PERFORMANCE 62

6. STRUCTURE 65

6.1 Materials 65
6.2 Wing Structure 65
6.3 Duct 67
6.4 Tail Surfaces 68
6.5 Landing Gear 69

7. PRELIMINARY TESTING 70

1. INTRODUCTION

The NASA Ames/DSI oblique wing remotely piloted research aircraft, shown in Figure (1.1), is a highly unusual, variable remotely piloted vehicle whose configuration and capabilities are the result of certain initial design guidelines that, in terms of conventional aircraft structures and configurations, would be considered to be contradictory and unachievable. Accordingly, the novel design of the yawed wing RPV is at odds in many respects with conventional aircraft practice. Novelty, then, forms the first, unwritten, design guideline. This design is intended to move away from convention in geometry, structure, and materials.

The following are the specific guidelines followed in the design of the yawed wing RPV along with a short discussion of the impact of each on the configuration of the vehicle.

1. ALL WING CONFIGURATION

All wing is taken to mean no fuselage and no tail. To this end the engine and payload are housed in the wing. One feature unique to all wing configurations is an increasing structural "g" limit with the addition of payload up to the point where the mass distribution matches the lift distribution.

A short coupled tail structure is incorporated in the design to provide static stability while yawed. Provisions are made for removing the tail structure if flights with relaxed stability are to be made.

2. YAWED WING

Wing yawing was the preeminent design requirement. Combined with the all-wing guideline, the requirement to yaw the wing forms a most difficult set of requirements. To accommodate wing yaw, the structure is designed such that the engine is housed in a rotating turntable. To the turntable is attached the short tail structure and a small fuselage to house a forward viewing television camera.

3. PLASTIC MATERIAL

The use of conventional plastics was ruled out by the high stress level produced in the unconventional geometry of the RPV. Had stress levels been lower, the development of the necessary technology to fully utilize plastic materials would still have been beyond scope (and budget) of this program in light of the other unusual requirements placed on this vehicle. The material used is fiberglass/epoxy which, in common with plastics, has the advantages of low radar signature and high energy absorption capabilities.

4. CRASH SURVIVABLE/REPAIRABLE

Crash survivability is a product of the all wing configuration. It was found in early model tests that tail structures and surface represent the highest liability during launch and recovery operations. Tailless models easily survived without damage in net and snag recoveries that would have rendered tailed models unflyable.

Repairability accrues from the use of epoxy for 90 percent of the structure. Field repairs will be possible in many cases. Particularly vulnerable items such as the wing tips, the horizontal tail and the vertical tip are frangeable and are easily replaced in the field.

5. PAYLOAD - 160 LBS.

Wing area and power available allow for a payload of well above the required figure. Payload volume available in the removable leading edge is 8 ft^3.

6. GIMBALLED T.V. SYSTEM WITH WIDE ANGLE AND ZOOM LENS

The T.V. system tilts $\pm$ 80 degrees. A 10:1 zoom lens provides a field of view from 5.3 to 53 degrees in width. A separate wide angle lens is not provided since the wide field of the zoom is considered adequate.

7. PARACHUTE RECOVERY CAPABILITY

A fast deploying parachute system is provided for emergency use. A certain amount of damage will be sustained in a parachute recovery, but will not extend to the primary structure.

8. AUTOPILOT

A two-axis autopilot with altitude hold capability is selected from the ground. Bank and pitch changes may be commanded while in autopilot mode.

9. DUCTED PROP

A 50 inch diameter duct shrouds the propeller. The duct improves low speed thrust and adds a degree of safety to ground handling operations.

10. CATAPULT LAUNCH

Wheeled takeoff is used for initial flights. Catapult launch capability is not provided at this time but may be added at a later time.

The rest of this report is organized to provide a reasonably detailed examination of the efforts expended under this contract starting with the project task organization and ending with ground testing of the RPV. There are two companion volumes to this report: Volume II is a compilation of all drawings and schematics created for purpose of fabricating the RPV; Volume III is a short, Operations Manual.

PROJECT ORGANIZATION

Project tasks were organized into three parallel efforts. These were airframe design and fabrication, avionics development and construction, and propulsion development and testing. These efforts and their component tasks are illustrated in Table I.

Each effort underwent an initial definition phase. These necessary design guidelines were changed drastically between the time the proposal was generated and the start of the program. In addition, the engine that was to be used initially was not available and a suitable replacement had to be chosen.

Since the static stability of a yawing all wing aircraft could not be evaluated theoretically with much confidence, finalization of the configuration and structural design could not begin until the completion of wind tunnel testing. The tests resulted in several modifications to the initial configuration. A design review was held after the design concepts had been further refined and resulted in further changes. As shown in Table I the original completion period was nearly half spent before detail design could begin.

Avionics development was a continuous effort from the beginning of the program. While every effort was made to use commercially available components where possible, it was necessary to develop circuits for most functions.

PROJECT ORGANIZATION

TABLE I

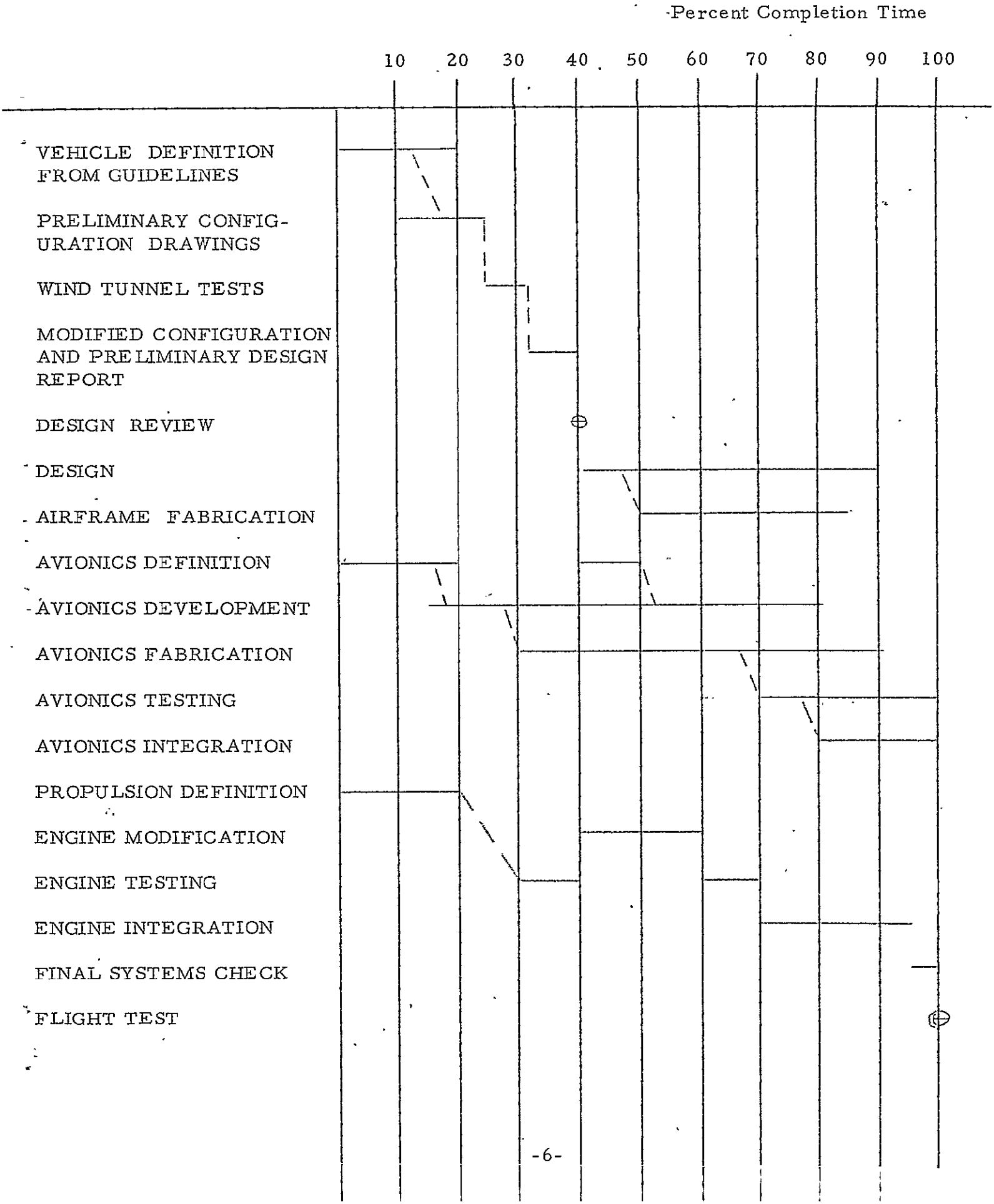

A number of unique circuits were designed in the course of this development which are described in the technical section of this report

Engine development consisted of the examination of a number of candidate engines and purchase of and modifications to the chosen unit. Integration into the unconventional airframe presented as much a problem in this area as the engine modifications themselves.

Overall system integration, once the components were completed, presented very little problem since constant interaction occured during design of the individual components. Nevertheless, component mounting, interwiring, final testing and trouble shooting proved to be a time consuming phase.

2. VEHICLE CONFIGURATION AND AERODYNAMICS

2.1 Configuration

Design guidelines call for an all-wing vehicle capable of flying at wing yaw angles between $0 < \Lambda < 45^{o}$. Early aerodynamic analysis indicated that it might be difficult, if not impossible, to achieve longitudinal static aerodynamic stability without a horizontal tail. This was later borne out by more detailed theoretical and experimental analysis. Thus, as presently configured, the aircraft is fitted with a "T" tail with removeable horizontal surfaces. The craft can be flown in the zero-to-moderate yaw configuration without the elevator, but is statically unstable without it in the 45^{o} yaw configuration.

Figure (2.1) shows a three-view of the vehicle with elevator attached. The craft has a wing span of 22.7 ft. and an overall length of 13.4 ft. Other basic data are listed later for both the wind tunnel and the final configurations.

The vehicle is controlled largely by a pair of elevons which are operable both differentially (as ailerons) and together (as an elevator). The aileron/elevator command functions are achieved electronically rather than mechanically. Actuation is by servos based on lightweight gear motors direct-coupled to the elevons.

The horizontal tail is operated by a separate servo commanded by the same circuit as the elevons' elevator functions. Thus, the tail can be removed and the craft flown as a flying wing when desired while still utilizing the elevator function of the elevons.

The 21% thick reflexed wing airfoil section is shown in Figure (2.2), and is constant over the entire untwisted $\mathcal{R} = 5.0$ elliptic planform. The thick wing was selected on the basis of the payload housing requirement specified by NASA and structural requirements.

The outboard leading edge of the wing is largely non-structural and is removable for installation and removal of payload. The wing is "dished" near the center (producing the flared spanwise thickness distribution shown in Figure (2.1)) to permit yawing of the fuselage with respect to the wing without breaking the contour of the fuselage/wing mating surfaces. The trailing wing is fitted with a vertical stabilizer which provides weathercock stability at the larger wing yaw angles. The wing tips and tip stabilizer are frangeable to minimize damage at recovery. The wing structure is discussed in a later section.

The fuselage consists of the nose, the central disc or "cookie", and the tail assembly.

The nose contains the television scanner and related zoom and tilt mechanisms, as well as the flight instrumentation and instrumentation camera, command receiver, yaw, roll and pitch gyros and transmitters for the television signal, and UHF tracking. Also contained in the nose is the battery, fuel tank, and vacuum pump.

The "cookie" (so nicknamed since it is in essence a circular disc of constant thickness (6.9")), contains the 90 H.P. engine, a 46.5 ft. paraform chute, and related equipment. A spanwise slit through the cookie accommodates the propeller disc.

Attached to the cookie is a 48" inside diameter propeller duct of symmetrical 18% thick airfoil section. The propeller duct improves static thrust and thrust at low speeds, permitting a high cruise speed prop to be used while still achieving satisfactory takeoff and climb performance. The duct also reduces propeller tip noise, and protects operators from the spinning propeller.

Drawings in Volume II show the chute deployment arrangement. Deployment of the chute occurs automatically when the command signal is lost. The craft can also be deliberately recovered by this method in response to a command signal from the ground.

The horizontal tail is mounted in the "T" arrangement to minimize aerodynamic interference with the wing at the high wing yaw angles. It is constructed of a thin layer of epoxy-fiberglass backed by a foam filling and is frangeable to minimize recovery damage. The tip part of the vertical tail is also constructed of this material and is also frangeable. The vertical tail is fitted with a controllable rudder.

The vertical/horizontal tail components are supported by a large diameter tube structure designed to accommodate the wing yawing motion. Two additional braces are "Veed" from the duct to the tail to stiffen the tail assembly in torsion, thereby minimizing the danger of flutter. These braces are carried through the duct and continued upstream to the fuselage nose. Another tube connects the nose to the bottom of the propeller duct for support, and to deflect the arresting cable in the case of a low approach when using a horizontal-cable snag recovery system.

2.2 Aerodynamics

Oblique-wing aircraft configurations have a number of unique aerodynamic features and problems. This is especially true for tailless and short tailed configurations where the oblique-wing problems assume first order prominence. To date, aerodynamicists have had little experience with solving these problems so that at the present time, few design guidelines exist. Therefore, as part of the present development program, it was necessary to explore in detail the idiosyncrasies of oblique-wing configurations, establish the needed guidelines, and incorporate them into the RPV design.

This task was approached both theoretically and experimentally through the use of the DSI-Neumann potential flow computer programs and wind tunnel tests performed by DSI at NASA-Ames.

The axis system used is a wing fixed or stability axis system shown in Figure (2.3).

2.2.1 Theoretical Analysis

In order to provide a deeper understanding into oblique-wing aerodynamics as well as to permit extrapolation of wind tunnel data, the RPV wing was analyzed using the DSI-Neumann lifting-latice computer program. As originally constructed, this program was restricted to bodies with planes of symmetry, so that it was necessary to re-write the program to accommodate assymmetrical bodies such as the oblique-wing.

Figure (2.4) shows the calculated lift as a function of angle of attack for four wing yaw angles (Λ = 0, 15°, 30°, and 45°) for the RPV wing camber and planform geometry. As expected, the lift-slope decreases with increasing Λ (Figure 2.5).

Figure (2.6) shows the influence of wing yaw angle on the position of the aerodynamic center, X_{ac}, at zero Mach number as computed with the Neumann program for the DSI RPV wing. As can be seen, the aerodynamic center* moves forward by a considerable amount as Λ increases to 45°.

To obtain static aerodynamic stability throughout the range $0 < \Lambda < 45°$ with a tailless airplane it would be necessary either to continuously move the c.g. of the aircraft forward to match the movement of the aerodynamic center with Λ, or to initially set the airplane c.g. ahead of the maximum forward a.c. position corresponding to the maximum Λ.

The first solution proves to be impractical, although it must be noted that by offsetting the wing c.g. from the plane of initial symmetry in the direction of the forward-moving wing, an appreciable forward motion of the total aircraft c.g. can be achieved in cases where $\frac{W_w}{W_f}$ is of order unity. On the other hand, if the center of gravity of the wing itself is ahead of the wing pivot point,

---

*As measured from the L.E. of the Λ = 0 wing.

and no such initial offset of the wing c.g. is provided, the total airplane c.g. will move rearward further compounding the stability problem when $W_w/W_f = 0$ [1].

In the present aircraft design, the payload must be carried in the wing structure, and the payload c.g. must be located on the craft center of gravity which in turn must be forward of the quarter chord point. Thus, the wing c.g. is necessarily ahead of the pivot point and also, $W_w/W_f = 0$ [1] (specifically, with full payload, $W_w/W_f = 0.5$).

This, of course, can be minimized by laterally offsetting the c.g. in the direction of the leading wing, but this solution obviously creates the necessity for corrective aileron trim to maintain level flight at $\Lambda = 0$.

The second possible solution mentioned above to deal with the stability problem (i.e., setting the initial c.g. ahead of the maximum forward a.c. position corresponding to $\Lambda = \Lambda_{max}$) creates serious trim problems for $\Lambda = 0$.

Finally, with an all-wing type of configuration, in practice it is difficult to obtain a c.g. location much further forward than about 25% chord, which requires that all payload and most of the propulsion system be located forward of the quarter chord.

Thus, in conclusion, with true tailless oblique wing aircraft configurations, it is either necessary to provide substantial initial lateral center of gravity offset to obtain static longitudinal stability, or to equip the craft with an artificial stability system.

2.2.2 Wind Tunnel Tests

Model and Tunnel

An unpowered wind tunnel model (Figure (2.7)) was constructed on a scale of 0.1794 (model span = 48"). By comparing values in Table II it is seen that the model configuration tested differs somewhat from the final configuration. These changes resulted from the findings of the tests themselves. All computations made in this section relate to the model as tested rather than to the vehicle.

The model was fitted with a six-component wind tunnel balance mounted to the "cookie" so that the balance was fixed with respect to the tunnel support system and sting, and the wing moved with respect to the balance/sting/support system. The reference moment center was locate at the position corresponding to the 1/4-chord point of the $\Lambda = 0$ wing. Tests were performed in the Army-Ames 7' x 10' wind tunnel at a speed of 170 ft/sec.*

Experiments were performed at two wing-yaw angle settings ($\Lambda = 0^{\circ}$ and 45°) with variable elevon settings, (both differential and together) as well as with and without horizontal tail and various horizonta tail angles.

*$\mathrm{Re} = \frac{V_c}{\nu} \approx 10^6$ and $q = \frac{1}{2}\rho V^2 \approx 35$ #/ft^2.

TABLE II

RPV AND MODEL DIMENSIONS

NOMENCLATURE		WIND TUNNEL MODEL	FINAL CONFIGURATION	RATIO FINAL/MODEL
Span	b	48.25 in.	268 in.	
Chord	c	12.25 in.	68.3 in.	
Wing Area	S	464 $in.^2$	99.8 $ft.^2$	
Aspect Ratio	A	5.02	5.00	.996
Tail Length, Horizontal	lt	9.75 in.	74.25 in.	
	l/t/c	0.796	1.087	1.366
Tail Height	ht	4.50 in.	28.5 in.	
	ht/c	0.367	0.417	1.136
Fuselage length L.E. to nose	lf	10.25 in.	63.5 in.	
	lf/c	0.837	0.930	1.111
Fuselage Diameter	D_f	3.0 in.	18.0 in.	
	D_f/c	0.122	0.132	1.082
Tail Length Vertical	lv	7.75 in.	68.75 in.	
	lv/c	0.633	1.007	1.591
Elevon area	Se	45.5 $in.^2$	11.75 $ft.^2$	1.204
	Se/S	.098	.118	
Elevator area	St	50.3 $in.^2$	12.9 $ft.^2$	
	St/S	0.108	0.129	1.194
Vertical area	Sv	18.0 $in.^2$	5.56 $ft.^2$	
	Sv/S	0.0387	0.0556	1.437
L.E. to center of rotation	d	6.125 in.	29.25 in.	
	d/c	0.50	0.428	0.856
Duct diameter	D	8.625 in.	50.5 in.	
	D/c	0.352	0.370	1.051
Horzontal tail volume		.086	.140	1.63
m	ht/b/z	.19	.21	
r	lt/b/z	.41	.55	
downwash at tail		.53	.49	0.925

Flow-Visualization

Before presenting the force data, it is useful at this point to examine some tuft photographs taken of the model under various conditions. These photographs will help to explain many of the phenomena observed in the force balance results.

Figures (2.8a) and 2.8b) show the model RPV with $\Lambda = 0$ at angles of attack of $\alpha = 0^{\circ}$ and 15° (near stall) respectively. These results are substantially what is to be expected. It is noted from Figure (2.8b) that stall occurs first at the root which is a desirable condition.

By way of contrast, Figures (2.9a) and 2.9b) show dramatically different behavior at $\alpha = 10^{\circ}$ and 20° (stall for the $\Lambda = 45^{\circ}$ wing). In particular, even when the wing is at a relatively low angle of attack (Figure (2.9a)), the flow aft of the elevon hinge lines is seen to be predominately spanwise, particularly on the trailing wing. This would suggest that the elevon would not be too effective, either in roll or pitch control at this value of Λ.

At $\alpha = 20^{\circ}$, the spanwise flow completely dominates the picture as can be seen from Figure (2.9b).

Further flow visualization studies showed that the tufts attached to the propeller duct (top and bottom) indicated no tendency toward separation despite the small nose radius of curvature of the duct. This would suggest that the flow turning was accomplished wholly by the wing and that the effective local angle of attack of the duct (and hence its loading) did not vary appreciably with craft angle of attack.

Drag Polar

Figure (2.10) shows the experimentally measured drag polars for the $\Lambda = 0$ and $\Lambda = 45^{\circ}$ configurations without elevator in the range $0 < C_L < C_{L_{max}}$. The slope of these curves gives the effective aspect ratio of the lifting surfaces (independent of any particular theoretical assumption) in the linear range of the C_D vs C_L^2 curves. The following values may be determined from Figure (2.10).

$$AR_e = 5.0 \qquad (\Lambda = 0)$$

and $$AR_e = 2.4 \qquad (\Lambda = 45^{\circ})$$

Since the $\Lambda = 0$ geometrical aspect ratio is 5.0, this implies that Oswald's efficiency factor for the elliptic wing is $e = 1.0$. Also, since geometrically,

$$(AR)_{\Lambda} = (AR)_{\Lambda = 0} \cos^2 \Lambda \qquad \text{(approximately)}$$

$$(AR)_{45} = 5.0\,(.707)^2 = 2.5$$

Then, for $\Lambda = 45^{\circ}$, $e = \frac{2.4}{2.5} = 0.96$

It is also noted from Figure (2.10) that the parasitic drag coefficient C_{D_p} for the $\Lambda = 0^\circ$ configuration is

$$C_{D_p} = 0.026$$

while for the $\Lambda = 45^\circ$ configuration,

$$C_{D_p} = 0.020$$

The reason for this 30% drag difference is not really clear, although it is suspected that in yawing the wing, some of the gaps and openings in the model required to accommodate the motion of the wing relative to the "cookie" were better sealed in the 45° configuration than in the $\Lambda = 0^\circ$ one.

Adding the horizontal tail increased the parasitic drag coefficient to a value of

$$C_{D_p} = 0.028$$

which constituted about a 5% increase in drag.

The high drag values at $\Lambda = 0$ result from the geometrical compromises associated with the requirement of variable wing yaw angle. If it were not necessary to yaw the wing, the aerodynamic cleanness could be improved at $\Lambda = 0$. Alternatively, it could be possible in practice to design sliding fairings to keep the geometry clean throughout the wing-yaw range. To determine the effectiveness of such fairings, the gaps and openings required to accommodate the wing motion in the model were sealed with

modeling clay in the $\Lambda = 0^{\circ}$ configuration. The result was

$$C_{D_p} = 0.0217 \text{ (with tail)}$$

$$C_{D_p} = 0.0208 \text{ (without tail - estimated)}$$

a reduction of about 23% over the unfaired craft geometry drag.

However, it is noted that this parasitic drag coefficient is still about 4 percent higher than that of the unfaired $\Lambda = 45^{\circ}$ configuration.

Longitudinal Forces ($\Lambda = 0$)

Figures (2.11) and (2.12) show the pitching moment coefficient about the 1/4-chord point, and the lift coefficient as functions of angle of attack and four different elevon settings for the $\Lambda = 0$ wing yaw tailless configuration.

The elevons are seen to have a powerful pitching effect with little sacrifice in $C_{L_{max}}$ for the elevon up condition, even for $\delta_e = -20^{\circ}$ (positive sign denotes elevon trailing edge down).

A straight line approximation was made to the data shown in Figure (2.11) in the range $0 < \alpha < 9$ degrees for elevon angles of -10, 0, and 10 degrees. These slopes were averaged to arrive at

$$\frac{\partial C_{m\ 1/4}}{\partial \alpha} = .0015 \text{ per degree.}$$

Also,

$$\frac{\partial C_L}{\partial \alpha} = 0.064 \text{ per degree}$$

Since

$$X_{ac} = 0.25 - \frac{\partial C_{m\ 1/4} / \partial \alpha}{\partial C_L / \partial \alpha}$$

Then

$$X_{ac} = 0.227$$

varying only slightly with δ_e for the $\Lambda = 0$ configuration with no horizontal tail. Let us note in passing that the experimental results of Figure (2.11) show a real problem for elevon deflections of -20 degrees with no elevator.

Now, adding a horizontal tail will move the aerodynamic center aft by an amount

$$\Delta X_{ac} = \frac{a_t}{a_w} \left(1 - \frac{d\epsilon}{d\alpha}\right) \frac{l_t}{c} \frac{S_t}{S_w} \qquad \text{-----(1)}$$

For the tail location on the wind tunnel model shown in Figure (2.7), the nondimensional horizontal and vertical tail a.c. locations with respect to the wing a.c. become, respectively,

$$r = \frac{2\ l_t}{b} = 0.405$$

and

$$m = \frac{2\ h_t}{b} = 0.183$$

From Perkins and Hage (reference (1) - pp 224), using data for AR = 3 as representative of the elliptic wing,

$$\frac{d\epsilon}{d\alpha} = 0.53$$

for these values of r and m

Recalling that

$$a_w = 0.065$$

and noting that the tail aspect ratio is

$$AR = 4.94$$

then, for $a_{o_t} = 0.107$ (reference (1))

$$a_t = \frac{a_{o_t}}{1 + \frac{57.3\ a_{o_t}}{\pi AR}} = \frac{.107}{1 + \frac{57.3\ (.107)}{\pi\ (4.94)}} = 0.076$$

From equation (1),

$$\Delta X_{ac} = \frac{0.076}{0.065}\ (1 - 0.53)\ (.796)\ \left(\frac{11}{100}\right) = 0.0481$$

Thus, the calculated aerodynamic center of the model with the horizontal tail (i.e., the stick fixed neutral point) is

$$X_{ac} = 0.227 + 0.048 = \underline{0.275}\ \text{(theoretically)}$$

From the experimental results of Figure (2.13) for the model with tail it is seen that

$$\frac{\partial C_{m\ 1/4}}{\partial \alpha} = -.0015 \quad 0<\alpha<5$$

From the same tests $\frac{\partial C_L}{\partial \alpha} = .0705$.

Thus,

$$X_{ac} = 0.25 - \left(\frac{-.0015}{.0705}\right) = 0.25 + .0212$$

$$= 0.278$$

Which is in good agreement with the theoretical prediction ($X_{ac} = 0.275$). Thus, even with such a short coupled horizontal tail, the simplified theoretical approach used above gives realistic results, and can be used confidently in making any modifications to the design, at least for the case of the $\Lambda = 0$ configuration.

Longitudinal Forces ($\Lambda = 45^{o}$)

Figures (2.14), (2.15), and (2.16) show the experimentally obtained longitudinal behavior of the $\Lambda = 45^{o}$ configured model. The Neumann theoretically predicted behavior is included hwere appropriate for comparison. From Figure (2.14) it is seen that the tailless $\Lambda = 45^{o}$ configuration achieves about the same maximum lift coefficient ($C_{L_{max}} = 0.98$) as the $\Lambda = 0^{o}$ configuration; although at a higher angle of attack (24^{o} instead of about 15^{o}). The lift-curve slope for this configuration is seen to be

$$a_w = 0.042 \quad \text{(per degree)}$$

From the experimental results of Figure (2.15), it may be determined that for the $\Lambda = 45^{o}$ tailless configuration in the linear range of the data, ($-9^{o} < \alpha < 9^{o}$)

$$\frac{\partial C_{m\ 1/4}}{\partial \alpha} = .0034$$

and that this slope is sensibly independent of the elevon angle.

Thus, in this α range, the aerodynamic center is located at the fixed position

$$X_{ac} = 0.25 - \frac{0.0034}{0.042}$$

$$= 0.25 - 0.081$$

$$= 0.169$$

The Neumann predicted result for the $\Lambda = 45^{\circ}$ configuration is $X_{ac} = 0.246$, suggesting that the influence of the nose is possibly

$$\Delta X_{ac} = 0.246 - 0.169 = 0.077$$

for the $\Lambda = 45^{\circ}$ configuration in this α range. A faired curve based on the theory for the aerodynamic center travel is shown in Figure (2.16).

In the range $9^{\circ} < \alpha < 18^{\circ}$, before stall, the moment drops off sharply and the a.c. moves to

$$X_{ac} = 0.25 - \frac{-0.00384}{.042}$$

$$= 0.25 + 0.091$$

$$= \underline{0.341}$$

In the stall region of this wing ($\alpha > 18^{\circ}$) the curve again reverses, putting the a.c. very far forward and giving an unstable stall.

Referring again to the flow visualization photos, this would suggest that as the stall begins, the trailing wing becomes almost completely

ineffective due to the rearward drift of the boundary layer (i.e., the trailing stalls before the leading wing). The sudden reversal in the region ($10^{o}<\alpha<18^{o}$) is yet unexplained.

Now, comparing Figures (2.15) and (2.11), it is also seen that the effectiveness of the elevons in generating pitching moments at $\Lambda = 45^{o}$ is drastically decreased in comparison with their effectiveness at $\Lambda = 0$, even though the net centroid of the elevon area with respect to the balance center remains essentially unchanged longitudinally. However, since the leading elevon moves ahead of the balance center and retains its aerodynamic effectiveness, while the aft-moving trailing elevon rapidly loses its effectiveness, the result is a reduction in pitching moment for given elevon settings, especially at the higher angles of attack as is clearly seen in Figure (2.15).

We shall now attempt to test the accuracy of the theoretical approach to predicting the effect of the horizontal tail on the craft stability for the $\Lambda = 45^{o}$ configuration. This is likely to be crude indeed, since at present we have little in the way of proven downwash information on yawed wings. However, we shall continue undaunted to use straight wing information to achieve the answers, and check the results obtained with the present experiments to determine the magnitude of the resulting errors.

From equation (1)

$$\Delta X_{ac} = K \frac{a_t}{a_w} \left(1 - \frac{d\epsilon}{d\alpha}\right) \frac{l_t}{c} \frac{S_t}{S_w}$$

where the empirical constant K is now inserted to account for the yawed wing effect.

$$\Delta X_{ac} = K \frac{0.076}{0.042} (1 - .53) (.796) \frac{11}{100} = 0.0744$$

Now, from the experiments with the elevators in place ($\delta = -6$ deg.) in the range $-9^{o} < \alpha < 9^{o}$.

$$C_{m_{\alpha}} = .0012$$

Thus, the aerodynamic center for the yawed wing model with horizontal tail is

$$X_{ac} = 0.25 - \frac{.0012}{.042} = 0.25 - .0286 = 0.2214$$

Since the original a.c. location in this range was

$$(X_{ac})_{tailless} = 0.169$$

then

$$\Delta X_{ac} = .0524$$

Solving for K

$$K = \frac{0.0524}{0.0744} = 0.704$$

Which is a result that will be used in aerodynamic modifications to obtain the final design.

In the range $9^{o} < \alpha < 18^{o}$, the experimental data gives

$$X_{ac} = 0.25 - \frac{-0.00334}{0.042}$$

$$= 0.25 + .080 = 0.330.$$

Corresponding to

$$X_{ac} = 0.341 - 0.330 = 0.011$$

which means that in this range, the tail is not nearly as effective in stabilizing the craft as it is in the range $-9^{o} < \alpha < 9^{o}$. However, in this range, the craft is very stable anyway.

Lateral Results $\Lambda = 0$

The experimental results of interest here are the yaw restoring moments due to sideslip angle and the aileron power.

As a benchmark for the yaw behavior, the theoretical yaw restoring derivative C_{N_β} is ideally

$$\frac{\partial C_N}{\partial \beta} = a_v \frac{l_v}{c} \frac{S_t}{S}$$

For the model under consideration

$$\frac{S_V}{S} = 0.36 , \frac{l_v}{c} = 0.55 , AR_v = \frac{b_v^2}{S_v} = 1$$

$$a_v = \frac{a_{o_v}}{1 + \frac{57.3\, a_{o_v}}{2\pi AR_v\, c}} = \frac{.107}{1 + \frac{57.3\,(.107)}{2\pi(1)}} \doteq .055$$

where the 2 accounts for the imaging affect of the wing on the vertical tail aspect ratio, since on the original model, the two overlapped. Thus, theoretically,

$$\frac{\partial C_N}{\partial \beta} = 0.036\,(.55)\,(.036) = 0.0010 .$$

The experimental results of Figure (2.17) show that for the model without the horizontal tail, the yaw restoring moments due to vertical tail are

$$\frac{\partial C_N}{\partial \beta} = 0.0009$$

The agreement of this experimental value with the calculated effect of the tail indicates that, contrary to the results in pitch, the nose has little de-stabilizing effect in yaw. This is propably due, in part, to the fact that there exists a horizontal slot in the nose (to accommodate wing yawing) which permits fluid to flow through the nose when it is yawed relative to the stream, thereby reducing its lifting effectiveness. This slot does not affect the lift generation of the nose in pitch. Additional stabilizing moment is contributed by the duct, making the de-stabilizing contribution of the nose somewhat larger than indicated.

For the case with horizontal tail attached to the vertical tail, the experimental results show that for $\Lambda = 0$

$$0.0010 \quad \frac{\partial C_N}{\partial \beta} \quad 0.0022$$

depending on the craft angle of attack. Values are quite close to results without the elevator in the same range of α.

The following formula is suggested in reference (1) for a desirable value of yaw restoring moment

$$\left(\frac{\partial C_N}{\partial \beta}\right)_{\text{desirable}} = 0.0005 \sqrt{\frac{W}{b^2}}$$

For the present RPV then,

$$\left(\frac{\partial C_N}{\partial \beta}\right)_{\text{desirable}} 0.0005 \sqrt{\frac{900}{(22)^2}} .0007$$

The restoring moment we assured is therefore sufficient.

Figure (2.18) shows the effectiveness of differential elevon deflection in generating rolling moment. From the data it can be found that

$$\left|\frac{\partial C_R}{\partial \delta \alpha}\right| = .0062.$$

Lateral Results $\Lambda = 45^\circ$

Figure (2.19) shows the yawing moments as a function of a sideslip angle for the $\Lambda = 45^\circ$ configuration at different angles of attack with and without horizontal tail. The data shows that the effect of angle of attack is much stronger than the restoring ability of the tail. The striking difference at $\alpha = 6$, $0 < \beta < 5$ between configurations with and without the elevator appears somewhat odd but may be explained in part by an end plating effect of the elevator.

Although this data is somewhat sketchy, and the results are a bit curious, the matter is somewhat academic since the craft cannot be trimmed in yaw at practical sideslip angles according to Figure (2.19) with the use of a short-coupled vertical tail at this value of Λ.

Thus, experiments were performed on the use of a vertical tip stabilizer as shown in Figure (2.20). This surface measured 3" x 3" and was airfoil-shaped and nominally symmetrical.

Assuming for simplicity that the aerodynamic center of the tip stabilizer is located precisely at the tip along a spanwise line drawn through the center of gravity, and that the stabilizer drag can be neglected with respect to its lift for the larger yaw angles, the yawing moment about the c.g. can theoretically be expressed as:

$$N = N_o - L_{t_s} \frac{b}{2} \sin \Lambda$$

where N_o is the yawing contribution of the wing/fuselage alone in the neighborhood of $\beta = 0^o$.

But,

$$L_{t_s} = C_{L_{t_s}} q S_{t_s}$$

$$= a_{t_s} (i - \beta) q S_{t_s}$$

and since,

$$\frac{b}{c} = \frac{\pi}{4} AR$$

then

$$C_N = C_{N_o} - a_{t_s} (i-\beta) \frac{S_{ts}}{S} \cdot \frac{\pi}{8} AR \sin \Lambda$$

Thus, the tip stabilizer incidence angle to give zero de-yawing at $\beta = o$ is

$$i_{trim} = \frac{C_{N_o}}{a_{t_s} \frac{S_{ts}}{S} \frac{\pi}{8} AR \sin \Lambda} \qquad \text{----(2)}$$

and, the yaw stability resulting from the tip stabilizer is, assuming

$$\frac{\partial C_N}{\partial \beta} = \frac{\partial C_{N_o}}{\partial \beta} + a_{t_s} \frac{S_{ts}}{S} \frac{\pi}{8} AR \sin \Lambda \qquad \text{----(3)}$$

For the i= 0, 3" x 3" tip stabilizer used in the $\Lambda = 45^o$ model the tests;

$AR\, t_s \approx 2.0$ (since the wing acts like a plane of symmetry for the tip stabilizer)

thus,

$$a_{t_s} = \frac{a_o}{1 + \frac{57.3\, a_o}{\pi\, AR}} = \frac{0.107}{1 + \frac{57.3 \times .107}{\pi (2)}} = 0.054$$

Now

$$S = 460.8 \text{ in.}^2, \quad \frac{S_{ts}}{S} = .0194$$

Therefore, from equation (2)

$$i_{trim} = \frac{C_{N_o}}{.054\ (.0194)\ \frac{\pi}{8}\ (5)\ (.707)} = 688\ C_{N_o}$$

Getting the $C_{N_o}(\alpha)$ from Figure (2.19) the theoretical plot of i_{eq} vs α is shown in Figure (2.21), where the experimental points are also presented. The agreement is seen to be reasonable, except @ $\alpha = 0$. From the figure, it is seen that the tip stabilizer will stall before the wing, resulting in de-yawing at the higher angles of attack.

Having demonstrated the applicability of the theory (it gives conservative results), we will employ equations (2) and (3) to size the tip stabilizer for the flying article to avoid the stall problem.

Figure (2.22) shows the rolling moment generated about the balance axis as a function of the craft angle of attack for different differential elevon (aileron) settings, δ_a. It is seen that the moment is a strong and nearly linear function of angle of attack. The Neumann theoretical preductions are also included for comparison for the $\delta_a = O$ case. An important point to note is that the elevons have sufficient control power to overcome the wing-induced rolling moment throughout the entire range.

This data is approximately expressible by the linear synthesis

$$C_R = C_{R_o} + \frac{\partial C_R}{\partial \alpha} \alpha + \frac{\partial C_R}{\partial \delta_a} \delta_a \quad \delta_a$$

where

$$C_{R_o} = 0.014$$

$$\frac{\partial C_R}{\partial \alpha} = 0.00217 \text{ per degree}$$

$$\frac{\partial C_R}{\partial \delta_a} = 0.001 \text{ per degree}$$

The elevon differential equilibrium angle is defined as

$$\delta_a = \delta_{a_{eq}} \quad \text{where} \quad C_R = 0$$

Then,

$$\delta_{a_{eq}} = \frac{\left(C_{R_o} + \frac{\partial C_R}{\partial \alpha} \alpha \right)}{\frac{\partial C_R}{\partial \delta_a}}$$

$$\delta_{a_{eq}} = -(7 + 1.1\,\alpha).$$

Which is plotted as a function of α in Figure (2.23). Now, it must be noted as discussed previously, that this is only true for the case where the wing is pivoted at the 50% chord point. On the final craft design, the pivot point will be placed at 42.6% chord which is shown in Section (2.2.4) give rolling moment independent of lift.

2.2.3 Glider Tests

An unpowered all-wing model was constructed and flown as a preliminary investigation of the aerodynamics and control of yawed all-wing aircraft. A launcher was also constructed which further served to provide a better understanding of launch methods and problems. Photographs of

the model are shown in Figure (2.24).

Basic data on this model are listed below:

Wing Area	3 ft^2
Aspect Ratio	8
Weight	2 lbs

The model was flown with wing yaw angles of 30 and 60 degrees. It was found that the elevons provided sufficient control to trim the model at all angles. It was not clear, however, that the model was statically stable at 60 degrees.

Tip rudders were used on this model. The rudders were set parallel to the fuselage. At $\Lambda = 60^{\circ}$ it was found that these rudders were ineffective in controlling the de-yawing tendencies of the model. The result was that after launch the model would de-yaw at which time the differential trim which had been applied caused the model to roll.

The trends revealed in these model tests later proved to be found in the wind tunnel results. The tests were therefore valuable in providinga "quick look" at these effects.

2.2.4 Final Configuration Aerodynamics

The wind tunnel data and related theoretical results were applied to modify the tested model configuration to achieve the desired flight characteristics of the RPV. In particular, improvements were sought aimed at moving the neutral point farther aft to provide static stability in all flight configurations, sizing the tip fin for the needed yaw trim, and reducing the influence of

angle of attack on roll trim. Thus, changes affecting the aerodynamics consisted of tail size and position, tip fin size and wing pivot position. A dimensional comparison is made between the model and final configuration in Table II.

Horizontal Tail

Changes made in the initial tail design (TableIII) were an increase in area of almost 20 percent, an increase in the tail length of 37 percent*, and a small increase in the height of the horizontal surface.

Recalling that the increase in X_{ac} is given by

$$\Delta\bar{X}_{ac} = K \frac{l_t}{a} \frac{a_t}{a_w} \frac{S_t}{S_w} \left(1 - \frac{d\epsilon}{d\alpha}\right)$$

Then,

$$\frac{(\Delta\bar{X}_{ac})_f}{(\Delta\bar{X}_{ac})_m} = \frac{(l_t)_f}{(l_t)_m} \frac{(S_t)_f}{(S_t)_m} \frac{\left(1 - \frac{d\epsilon}{d\alpha}\right)_f}{\left(1 - \frac{d\epsilon}{d\alpha}\right)_m}$$

Applying the dimensions from Table I,

$$\frac{(\Delta X_{ac})_f}{(\Delta X_{ac})_m} = (1.366)(1.194) \frac{(1-.49)}{(1-.53)} = 1.77.$$

This value is used to predict the aerodynamic centers for the modified configurations. Results are presented in Table III.

---

*The resulting length is still in keeping with the concept of a short coupled tail and the ultimate objective of tailless flight.

TABLE III

LONGITUDINAL SUMMARY

NEUTRAL POINT

Λ DEG.	CONFIGURATION	MODEL $\bar{X}_{ac}$	FINAL DESIGN $\bar{X}_{ac}$
0	No elevator	.227	.227
0	With elevator	.271	.303
45	No elevator	.169	.169
45	With elevator	.221	.263

Vertical Tail

The increased horizontal tail length and height result in greater vertical tail length and span respectively. This is desirable in that the yaw restoring derivative, $\frac{\partial C_N}{\partial \beta}$, was just barely adequate as tested and will be reduced somewhat on the final design as streamlining is added that blocks the slot in the fuselage.

The improvement in yaw stability due to tail length and span is given by

$$\frac{\Delta \partial C_N}{\partial \psi} = \left(\frac{\partial C_N}{\partial \psi}\right)_f - \left(\frac{\partial C_N}{\partial \psi}\right)_m$$

$$= \left(a_t \frac{l_v}{c} \frac{S_t}{S}\right)_f - \left(a_t \frac{l_v}{c} \frac{S_t}{S}\right)_m$$

$$= \left(\frac{a_{t_f}}{a_{t_m}} \frac{l_{v_f}}{l_{v_m}} \frac{S_{t_f}}{S_{t_m}} - 1\right)\left(a_t \frac{l_v}{c} \frac{S_t}{S}\right)_m$$

We have already increased the tail length by a factor of 1.59 in connection with the longitudinal stability. We now increase the vertical tail span by 33 percent and its area by 44 percent corresponding to the final configurational. The aspect ratio has then been increased by 54%. According to lifting line theory, this results in an increase of the lift slope of

$$\frac{a_{t_f}}{a_{t_m}} = \frac{.0655}{.055} = 1.19.$$

$$\frac{\Delta \partial C_N}{\partial \beta} = + (1.19 \times 1.59 \times 1.44 - 1) \quad (.0009)$$

$$= .00155$$

There is a great deal of uncertainty in this value since the de-stabilizing effect of the nose is unknown. Never the less, the value indicated is well within the desire range.

Tip Stabilizer

It is economical to have the tip stabilizer be identical to one half of the elevator since a large proportion of the cost of these parts is in the molds used to make them.

This surface has an effective aspect ratio (assuming that the wing acts like a plane of symmetry as previously considered)

$$AR = 2 \frac{b_{ts}^2}{S} = 3.6$$

and an area $S = 6.5 \text{ ft}^2$

$$a_{ts} = \frac{.107}{1 + \frac{57.3(.107)}{(3.6)}} = 0.07$$

$$i_{eq} = \frac{C_{N_o}}{.07(.075)\frac{\pi}{8}5(.707)}, \quad (\Lambda = 45^\circ)$$

$$i_{eq} = 103 \; C_{N_o}$$

This result is plotted in Figure (2.25)

The re-designed device is seen to provde powerful trim control. The pulley system which yaws the tip stabilizer along with the wing is geared such that an incidence of 3° is obtained when Λ reaches 45°. This will give an over-yawing tendency at $\alpha < 7.5^\circ$ and a de-yawing tendency at $\alpha > 7.5^\circ$ although this stabilizer will never let the craft de-yaw very much,

Wing Pivot

It is seen in Figure (2.22) that rolling moment increases with angle of attack, requiring corrective trim. There exists an axis parallel to the existing roll reference axis about which the rolling moment is invariant with C_L. The lateral distance to this axis from the axis used for the wind tunnel testing is given by:

$$S = \frac{\partial C_R}{\partial C_L} = \frac{\partial C_R}{\partial \alpha} \left(\frac{\partial C_L}{\partial \alpha} \right)^{-1}$$

where C_R is about the original (.50 c pivot) axis.

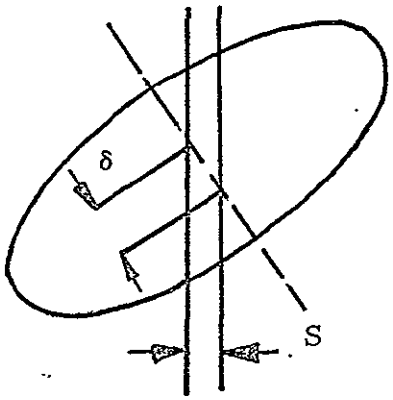

$$\delta = \sqrt{2}\, S$$

Experimental and theoretical values for $\frac{dC_R}{dC_L}$ are compared below. New values for the wing pivot, given by

$$\frac{x}{c} \text{ pivot} = 1 - \frac{2S + .5}{c} \text{ are included}$$

	$\frac{d C_R}{d C_L}$	$\frac{x}{c}$ pivot
Experiment	.052	.426
Theory	.050	.429

The difference between these two values amounts to only 0.2 inches difference. The experimental value has been adopted for the RPV design.

Wing Yaw Direction

The RPV wing is designed to yaw in only one direction -- port wing forward. This direction was selected on the basis of power-plant torque and slipstream rotation consideration.

i) Torque

Viewed from behind, the pusher propeller rotates in a counterclockwise direction, thereby generating a torque on the RPV in the clockwise sense. Since at positive lift coeffients, the craft has a natural tendency to roll into the leading wing, these two effects will tend to cancel if the leading wing is the port one.

The torque generated at a given power setting is

$$Q = \frac{P}{\Omega}$$

Thus, neglecting wing center of gravity affect,

$$C_R \; q \; S \; c \;\; = \;\; \frac{P}{\Omega}$$

Recalling that

$$C_R \;=\; C_{R_o} \;+\; \frac{\partial C_R}{\partial \alpha}\;\alpha + \frac{\partial C_R}{\partial \delta_a}\;\delta_a$$

and letting $\delta_a = 0$, then

$$(C_{Ro} + C_{R\alpha}\alpha)\; q \; S \; c \;\; = \;\; \frac{P}{\Omega}$$

for zero net rolling moment.

Now, in general

$$C_L \;=\; a\,(\alpha \;-\; \alpha_{ZL})$$

and $$C_L \;=\; \frac{n\,W/S}{q}$$

$$\alpha \;=\; \frac{n\,W/S}{qa} \;+\; \alpha_{ZL}$$

Thus,

$$\left[C_{Ro} + C_{R\alpha}\left(\frac{n\,W/S}{qa} \;+\; \alpha_{ZL}\right)\right] \; q \; S \; c \;\; = \;\; \frac{P}{\Omega}$$

So that

$$q^* \;\; = \;\; \frac{\dfrac{P/S}{\Omega c} \;-\; C_R \;\dfrac{n}{a}\;\dfrac{W}{S}}{C_{Ro} \;+\; C_{R\alpha}\;\alpha_{ZL}}$$

which is the dynamic pressure at which the net rolling moment vanishes. At $q < q^*$, the engine torque causes the craft to roll* in the direction of the trailing (starboard) wing, while for $q > q^*$, the aerodynamic forces dominate generating rolling moments in the direction of the leading (port wing). Taking for example,

$$P = 90 \text{ H.P.}, \quad \Omega = 4000 \text{ RPM } (410 \text{ rad/sec})$$

$$n = 1$$

and recalling the values of Figure (2.5),

$$q^* = 3.5$$

Since this value falls below flying $q(q_{stall} = 4.5 \#/ft^2)$, it is seen that corrective aileron will have to be applied to prevent rolling into the leading wing, despite the counteracting engine torque contribution.

ii) Slipstream Swirl

The port-wing-forward configuration also tends to reduce the de-yawing tendency as a result of slipstream action on the vertical tail. This is explained in the sketch below. The swirl component of the slipstream above the wing generates an effective angle of attack on the vertical tail which is in the yaw restoring direction.

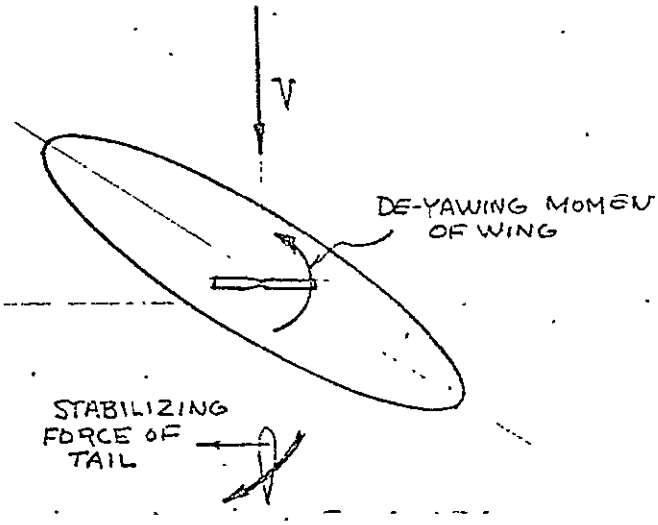

*In the absence of corrective aileron deflection, of course.

2.2.5 Flying Without A Horizontal Tail

The propsect of flying the RPV without a horizontal tail is an intriguing one. The horizontal tail represents added weight, drag, and expense, and is a distinct liability in recovery from the survivability point of view.

The wind tunnel results have shown that the craft will perform well without a horizontal tail at $\Lambda = 0^{\circ}$. However, at $\Lambda = 45^{\circ}$, the aerodynamic center is located at $X_{a_c} = .17c$, giving a statically unstable situation for obtainable c.g. locations. By comparing the Neumann theoretical results with the experimental data (Figure (2.16)), it can be inferred that the fuselage nose is partly responsible for the forward movement of the a.c. On the other hand, the forward location of the nose is also responsible for the c.g. being as far forward as it is. It must be noted that this configurational predicament may will be due to our present limited experience with yawed-wing aerodynamics. It may, in fact, be possible to design vehicle configurations and wing geometries which do not generate this difficulty. Clearly, the conceptually simple, though perhaps implementationally difficult idea of sliding part of the payload forward as the wing yaws would work, but it is felt that this artifice constitutes an inferior solution.

It is almost certain that the stability problem can be solved on a more fundamental level, but additional basic aerodynamic work is needed.

However, the stability problem can always be circumvented electronically by the use of the relatively simple notions of artificial stability. At least with the present craft the more intractable problems are trim and control. As seen from Figure (2.15) when the wing is yawed at 45° the elevons do not provide sufficient pitch power to control and trim the craft. Possibly the elevon planform should be re-designed - perhaps assymmetrically, or a wingtip elevator (either on the leading or trailing wings) could be used to achieve the needed control power for flight without a horizontal tail.

3. AVIONICS

The avionics system is required to provide complete control of the aircraft, to return flight data and a television picture to the ground station, and to track the vehicle. The desired range of these functions is 50 miles. The frequencies allocated for this purpose are listed in Table IV.

RPV FREQUENCY ALLOCATIONS

TABLE IV

Frequency MHz	Power Watts	Purpose
49.78	25	Command Control
240.2	25	Telemetry
1830.0	20	Video

3.1 Airborne System

Figure (3.1) shows the various airborne components and their interconnections. The command package performs all manual control functions and the logic and decoding for autopilot control. The instrument package contains all flight instruments as well as video switching circuitry whose function is to mix video frames from the nose camera and from the instrumentation camera that views the flight instruments. The mixed video frames are decoded and displayed on separate monitors on the ground. The artificial horizon in the instrument package is used for autopilot control, hence the connection to the command package. Other componants shown, either purchased or assembled from purchased parts are listed in Table V.

3.1.1 Command Package

The components of the command package are listed in Table V. Electronic circuits are provided for manual proportional control of control surfaces, throttle and steering, auxiliary non-proportioned control of other aircraft functions, interface with attitude gyros for autopilot control, amplification of instrument input, and the driving of servos and auxiliary function actuators.

A brief description of each circuit card follows.

AIRBORNE SYSTEMS COMPONENTS

TABLE V

ITEM	FUNCTION	MANUFACTURER AND NUMBER
Nose and Instrumentation cameras	Signal for Display of Forward	GBC Model CTC-5000 Modified Package
Zoom lense	Lense for nose camera	Zoomar Mark X-B
Camera/Compass inverter	400 AC For Camera	Texas Electronics 424 A
Autopilot Supply Inverter	15VDC Supply for autopilot logic	Abbott CC15D05
Vacuum Failure Switch	Drives indicator light for vacuum failure	Automotive part
FM Exciter	Telemetry exciter and tracking	GFE
VAF Amplifier	Telemetry and tracking RF amplifier	Greenray Industries, Inc. EA-117-2
LB and FM transmitter	Video Signal transmitter	3dbm Model LFT 1800-15
Servo Motors	Mechanical drive for control surfaces, etc.	TRW-GLOBE 5A515-1
Feedback Potentio-Meters	Position Signal	Bourns 1 k potentiometer
Throttle Servo	Throttle actuation	Kraft Kp 16
Squib	Parachute Deployment	Holex 3100 Pressure Cartridge
Receiver	Receives and decodes command signals	Kraft KPR-7

COMMAND PACKAGE COMPONENTS

TABLE VI

CARD NUMBER	FUNCTION
-1-	Autopilot Driver/Supply
-2-	(Blank)
-3-	Gyro Interface
-4-	(Blank)
-5-	Elevator Sig. Synth.
-6-	Auxiliary Select
-7-	Auxiliary Delay
-8-	Meter
-9-	Priority Control
-10-	Priority Drive
-11-	(Blank)
-12-	Servo Amp, Elevator
-13-	Servo Amp, Elevon
-14-	Servo Amp, Elevon
-15-	Servo Amp, Nose Wheel
-16-	Servo Amp. Rudder
-17-	Servo Amp. Camera Zoom
-18-	Servo Amp. Mixture (Option)
-19-	Servo Amp. Camera Pitch
-20-	Servo Amp. Wing Yaw

Connectors:
- P9-Nose assy. & Inst. Box
- P10-Nose Assy. & Inst. Box
- J11-Fuselage Cable
- J12-Wing Cable
- J7-Receiver Ant.

Power Terminals:
- C-28V. Command System Power
- X-28V. Transmitter Power
- GNO-Frame Ground

Receiver Ant Matching Network
5V Regulator

CARD #1 Autopilot Supply

The autopilot supply card provides stable ± 5 volts D.C. and 5KHZ, 10 V.P.P. square wave outputs for the autopilot gyro circuits.

Referring to Figure (3.2) a dual regulation circuit reduces the incoming ± 15 V.D.C. to approximately ± 5V.D.C. (adjusted to balance the gyro interface circuit). A 3.9K resistor and Diode interconnects the regulators to prevent lock-up of either side.

The 5 KHZ square wave signal is generated by a function generator I.C. (NE 566) and amplified by operational and power booster amplifiers (74 and B10). A capacitor in the feedback circuit rounds off the square wave slightly to prevent transients in other circuits.

CARD #3 Gyro Interface

The gyro interface card converts the gyro pick-off signals (5KHZ) to analogue roll and pitch voltages. The sum and difference of these signals is then formed to be used to drive the elevons.

Referring to Figure (3.3) this circuit uses MC1545 video switch I.C.'s as syncronous detectors. The first two MC1545's receive roll, pitch and altitude hold signals and are switched at the 5 KHZ rate in sync with the input signals. The detector outputs are integrated and then amplified by the second set of MC1545's. Finally, differential and common mode outputs are derived with operational amplifiers (741).

For manual operations, a gating signal is fed to the second set of MC1545's causing them to switch to their grounded inputs thus locking the outputs to zero error level and disabling the autopilot.

CARD # 5 Elevator Signal Synthesizer

An elevator signal is formed in this card to provide elevator control from the right and left elevon signals.

Referring to Figure (3.4) the right and left elevon signals, 1-2 MS pulses, are conditioned by two input Schmitt triggers. The first occuring pulse triggers a one shot flip-flop for the purpose of generating a time reference pulse equivalent to a neutral width elevon pulse (1.5 ms). The elevator pulse (output) is initiated at the completion of the one-shot pulse by changing the state of the out-put flip-flop.

The second elevon pulse, upon its completion, changes the state of the resetting flip-flop and concludes the elevator pulse.

Thus, as shown in the pulse detail, the elevator pulse follows the command mode function of the elevon signals only.

CARD # 6 Auxiliary Select

The auxiliary select card essentially divides the time domain of two command channels into sixteen discrete commands.

Referring to Figure (3.5) the input pulses, channel 5 and 7, are first shaped by Schmitt triggers, then each perform the function of controlling the following counting sequence: The leading edge of the first pulse (Channel 5) enables the one-shot flip-flop and the binary counter.

The one-shot and feedback transistor (Q 1) form a pulse generator with a pulse rate of about 4000 PPS. The counter is allowed to count these pulses as long as the input pulse is present. Since the input pulse has a width from 1 ms to 2 ms, the count range is then four (minimum) to eight (maximum). Actually, only Q_A and Q_B counter outputs are used, so at the end of the count period, the binary output will be from zero to three.

The trailing edge of the input pulse then clocks the output latches (A and B) and resets the one-shot and the counter. The "A" and "B" outputs now retain the previous count.

The second input pulse (Channel 7) controls the same functions with exception to clocking the "C" and "D" latches.

The output will now provide the full zero to fifteen binary codes, updated with each set of input pulses.

CARD # 7 Auxiliary Delay /Decode

The auxiliary delay/decode circuit converts the auxiliary select binary code to a one of sixteen output upon time completion of a preset delay period

Referring to Figure (3.6) the binary code input (0 to 4) is stored in a four-bit latch and decoded in a four to sixteen line demultiplexer. The latch output is compared with the input by a four-bit magnitude comparator which will give a logical "1" output if equal.

If, however, the latest binary update is different than the previous, then the comparator output goes low and allows the RC time period to start.

At the end of this delay period (.5 sec), the one-shot is triggered which gates the latch to the new data.

The output will be up-dated only if the binary code difference is maintained during the delay. Thus, momentary input changes from glitches, noise, etc. is ignored and only the valid auxiliary selection is passed through.

CARD # 8 Meter Amplifier

Exhaust gas temperature, head temperature and battery voltage signals are conditioned by this meter card to provide the proper voltages and ranges for meter read-out on the instrumentation panel.

Referring to Figure (3.7) a dual-operational amplifier I.C. is utilized to amplify the low level thermocouple voltages. Amplifier offsets and output diodes provide expanded scale read-out on B 0-1 MA meter load.

Battery voltage is also conditioned for expanded scale indication with a 20 volt zener diode and a 12,000 OHM resistor.

CARD # 9 Priority Control

Control of the more crucial elements of the avionics system are performed by the priority control card, i.e. autopilot on/off, altitude hold on/off and parachute deployment.

Referring to Figure (3.8) four discrete commands from the auxiliary select system are the inputs to two bi-stable flip-flops. These flip-flops are used simply as latches to hold the given "on" or "off" command. Cross connections prevent the altitude hold from being enabled (on) without the autopilot being on also.

A separate receiver (Channel 6) is measured for pulse width by comparing to a fixed pulse width froma one-shot flip-flop. As long as the input pulse width is greater than about 1.2 MS, then no output occurs. If, however the width is changed to 1 MS or disappears all together, then a 4 second time delay period is initiated. An output (chute deploy) command pulse will occur at the end of this period provided that the input pulse is not re-established with the normal 2 MS width.

CARD #10 Priority Driver

The priority driver card provides the power necessary to operate the engine kill and chute deploy relays, alt. hold solenoid and indicators from the signals derived in the priority control circuit.

Referring to Figure (3.9) the output drivers normally supply +28V. to the engine kill and chute deploy relays. Upon receiving a logical "o" input, the output will drop to zero volts.

The altitude hold and hook deploy outputs change from zero to a plus level with logic "o" input.

CARDS # 12 through 16

Proportional Servo Amplifier

Proportional command is amplified and controlled (through external position feedback) to drive a servo motor with output position relative to input command and pulse width.

CARDS # 17 through 20

Positionable Servo Amplifier

The positionable servo amplifier provides power amplification necessary to drive an actuator from auxiliary selection signals.

Referring to Figure (3.11), a logical "o" at either input from the auxiliary select system will drive the output to full on with polarity determined by which input is commanded.

Optional limit control is provided to disable the output polarity relative to the limited actuator direction.

3.1.2 Electrical

The power switch panel allows the command systems, transmitters and vacuum pump to be operated separately for purposes of power-up and check-out. Referring to Figure (3.12), power may be provided by either the RPV batteries or by ground power source. Alternately, the aircraft batteries may be charged through the ground power connector by switching the batteries onto the power bus. Starter current is controlled by a switch on the ground power cart.

The relay panel isolates and controls the engine kill, chute deploy and hook deploy functions. Referring to Figure (3.13) the engine kill and chute deploy relays normally receive + 28 volts D-C from the priority driver circuit. They are latched (prior to flight) by pressing the reset button. A pilot light then indicates latch-up, allowing safe arming of the chute squib.

Removal of the incoming +28 volts supplying the chute relay, will cause relay drop-out and thus connect the chute battery to the squib, if armed.

This function will also "kill" the engine by shorting the magnito circuit to ground.

The engine "kill" relay will also drop-out of latch with removal of supply voltage, however, it "kills" the engine only, leaving the chute relay still functional.

An optional hook deploy relay may be added. This relay normally will receive no voltage until a command is received at which time +28 volts will close the relay and operate a hook deployment mechanism.

3.1.3 Instrument Package and Nose Camera

The instrument package houses the flight instruments, the instrument camera and video encoder circuitry for mixing video signals from the nose and instrument camera. The instrument panel layout as it appears on the monitor is shown in Figure (3.14).

The wiring of the instrument package and nose camera are shown in Figure (3.15) and (3.16) respectively. A signal sync generator for the two cameras mounted on the nose camera causes the two cameras to scan simultaneously.

The video encoder, Figure (3.17), is housed in the instrument package and provides the logic and switching for time sharing the two video signals.

The video signals are selected sequentially by a video switching I.C., driven by a flip-flop synchronized to the vertical sync. pulse. The switching takes place during the vertical retract of each scan.

Thus, only field instead of a complete frame is selected from each camera. The video signals are adjusted for close match of amplitude and DC offset. Manual selection of either picture provided by grounding either the reset or set input of the flip-flop.

3.1.4 Control Logic Summary

The control block diagram, Figure (3.18), shows the control signal flow paths used for RPV control. Elevator control is used as an example. Other surfaces are controlled in a similar manner but do not receive inputs from the attitude sensor.

In the manual control mode, the auto pilot circuit is opened and command inputs produce control surface deflections proportional to the control stick position. This corresponds to conventional manual controls and may be thought of as a rate command in that the pitch rate will be proportional to surface position.

In the autopilot mode the pitch gyro signal is summed with the surface position signal. With this system an error signal from the pitch gyro will cause a surface deflection proportional to the error. Thus, since the rate is proportional to the error, pitch response to a disturbance will be without overshoot, neglecting aircraft inertia. Since the manual input is still present, it may be used to change the null pitch angle and thus the flight path.

In the altitude hold mode of operation an altitude error signal, indicating the difference in altitude from the position where the altitude hold was initiated, is summed with the other control signals. The altitude error signal may be thought of as providing an offset in the pitch null signal in the

proper direction to correct the altitude change. The equilibrium altitude will differ from the initial altitude by as much as several hundred feet if the RPV is not initially trimmed for level flight when altitude hold is initiated.

Control gains were determined by pilot preference while operating a simulator developed for this purpose at NASA/Ames Research Center. Gains for initial flights are shown in Table VII Actuator speed was limited to 13 RPM or approximately 78 deg/sec.

3.2 Ground Equipment

3.2.1 Command Control

The command system is based on a Kraft KPT-7 transmitter which is used as an encoder and exciter. In addition to the basic Kraft unit (slightly modified), input signal conditioning is provided by flight control and auxiliary select circuits. Output power is boosted by an RF amplifier to approximately 20 watts.

Flight Control

The flight control circuit interfaces the flight control sticks to the command transmitter encoder and generates the proper differential function of the aileron/elevator channels to provide the elevon control mode.

Referring to Figure (3.19) the D-C voltages from the flight control sticks are filtered (noise) and coupled to conditioning circuits through emiter followers. The aileron Channel (1) and the elevator Channel (2) signals are combined with summing resistors and differential amplifiers, the output of which is the elevon function.

The rudder and throttle channels are coupled unchanged to the output circuitry.

TABLE VII

CONTROL SURFACE GAIN

INPUT	RESPONSE Degrees	
Elevator Full Up	Elevator	10
	R. Elevon	10
	L. Elevon	10
Alerons Full RT.	R. Elevon	-10
	L. Elevon	
Rudder Full	Rudder	20
	Nose Gear	6
Pitch Gyro 10 deg. Up	Elevator	5
	R. Elevon	5
	L. Elevon	5
Roll Gyro 10 deg. RT.	R. Elevon	10
	L. Elevon	-10
100 Ft. Altitude Error	Elevator	2
	R. Elevon	2
	L. Elevon	2

All four outputs are emitter coupled to the transmitter/encoder channels one, two, three, and four respectively. Each output emitter follower acts as a clamp to the pulse amplitude which controls the timing of the succeeding pulse width.

This pulse width is thus proportional to the stick position.

A chute deploy circuit is also incorporated which simply shunts the timing resistor in Channel (6) of the encoder and shortens that pulse period.

Auxiliary Selection

The auxiliary select panel, Figure (3.20), incorporates six, two-position switches to control the selection of sixteen discrete commands.

Each switch selectively shunts the pulse timing resistors in Channels (5) and (7) in the encoder circuit of the Kraft exciter. This shunting causes the pulse width to decrease to one of three selected widths (four including no shunt) therefore, utilizing the two channels provides the sixteen combinations used for discrete commands.

3.2.2 Video Display

Receiving

Referring to Figure (3.21), incoming video signals are received through a parabolic dish antenna (29 db gain) and processed by a "building block" single conversion receiver.

Video Decoder

The function of the video decoder is to separate the incoming sequencial video signal for display on two monitors.

Referring to Figure (3.22) the incoming video is fed to both monitors symultaneously and if no sequencial blanking is used, then both pictures (nose and instruments) would be seen superimposed on both monitors. The decoder, however, prevents this by sequencially blanking each monitor, in sync with the vertical sync pulse.

The vertical sync pulse toggles a flip-flop circuit installed in the nose camera monitor. The output of this flip-flop drives clamping transistors to blank the video in each monitor sequencially. A diode and pot is provided for holding the raster on during blanking of the nose camera monitor. The pot is adjusted for minimum picture flicker.

3.2.3 Tracking System

The RPV is tracked using the 240 MHZ telemetry signal. Tracking serves three purposes: (1) Navigation (2) Aiming of the high gain TV antenna and, (3) Providing the basis for an automatic housing system.

The tracking antenna assembly is shown in Figure (3.23). It consists of two 7 element yagi's used for tracking and the TV antenna mounted on a common rotating mast.

The tracking system works by comparing the signal strength of the two yagi's which are aimed in slightly different directions so that their patterns do not coincide.

Referring to Figure (3.24), syncronized choppers samples each antenna. The power amplifier, Figure (3.25), drives the antenna rotor in response to a difference in signal strength between the two antennas.

Automatic RPV return control is accomplished by using the aircraft position error signal from the tracking system as shown in Figure (3.26). An error signal from the tracking system causes a 3 degree bank turn to be commanded in the proper direction to correct the RPV's track error. A typical path under automatic control is shown in Figure (3.27).

4. PROPULSION

The RPV engine is a McCulloch 4318 B target drone engine modified for use a a pusher and a power output of 90 horsepower. With an installed weight of 84 pounds including the propeller, this engine has by far the best power to weight ratio of any available engine below 100 horsepower. In this case, fuel consumption is the penalty for performance. The specific fuel consumption is estimated to be 0.9 to 1.3 depending on the power setting. A direct determination of sfc has yet to be done. Engine Specifications are listed in Table VIII.

Engine accessories include a Delco 2 kw aircraft alternator and a Bosch starter motor from an outboard motor. The alternator is mounted under the forward end of the engine and is driven by a timing belt from the modified magneto drive. The starter motor is mounted under the aft end of the engine and drive a ring gear on the propeller hub. The total added weight is 30 lbs.

The standard carburator was replaced with a pressure carburator (Tillotsen) which allows inverted operation and eliminates a separate fuel pump. The only modifications to the engine itself were the addition of a snap ring to the prop end of the crankcase.and a split ring on the prop end of the crank to take pusher thrust loads and the use of long life rod bearing. A muffler system was fabricated to reduce the exhaust noise. There was insufficient volume available for properly sized expansion chambers.

TABLE, VIII

ENGINE SPECIFICATIONS

Model: Model 0-100-1 Engine

Type: Two-cycle Air Cooled Engine

Number of Cylinders: Four

Bore: 3-3/16 inch.

Stroke: 3-1/8 inch.

Piston Displacement: 100 Cu. Inch

Compression Ratio: 8 to 1

Crankshaft Rotation: Clockwise (viewed from front of A/C)

Propeller Hub Bolt Circle Size: 4 Inch. Dia.

Propeller Hub Keyway: 1/4 in.

Number of Engine Mounting Eyes: Three

Size of Engine Mounting Eyes: 1 Inch

Weight of Engine Complete: 84 lbs. (Includes propeller)

Overall Diameter of Engine: 27 in.

Overall Length of Engine: 26 1/4 in.

Position of Center of Gravity: Seven Ins. AFT From forward Surface of Engine Mounting Eyes, and Vertically Through the Center of the Carburetor Venturi Tube

90 H.P. Developed at 4100 R.P.M. Rated H.P.

Magneto Speed: One to One

Magneto Breaker Point Gap: .018 Inch.

Spark Plug Type: RB916-S (BG Corp.)

Spark Occurs in Degrees Before Top Center - 25.°

Fuel/Oil Mixture: Ten to One

Type of Fuel: 115/145 Octane

The mufflers tested, therefore, all involved a compromise between power loss and noise suppression . The Table below summarizes the results of muffler tests with power expressed in RPM obtained with the same propeller. The "Flow Thru" muffler was installed on the RPV.

TABLE IX MUFFLER EFFECTIVENESS

CONFIGURATION	NOISE AT 20 FT. dba	RPM
Open exhaust	123	3750
Full Baffle Muffler	110	3300
Flow Thru Muffler	118	3500

Cooling ducts were fabricated to direct cold air through the cylinder cooling fins.

Total engine weight with the propeller, alternator, starter , mufflers and cooling ducts was 120 lbs.

All engine testing was done statically. Initial tests were with a gyrocopter propeller with a 48 inch diameter and a 24 inch pitch. Full throttle with no muffler was 3800 RPM and produced 360 lbs. thrust, without the duct. Later tests with a 30 inch pitch propeller running in the duct with .25 inch tip clearance produced 300 lb. thrust at 3950 RPM. The drop in thrust was due in part to the high pitch. It is felt that considerable improvement can be made by adding an effective tip seal.

5. PERFORMANCE

The craft performance depends to a great extent on the selection of the fixed-pitch propeller. The selection of the propeller, in turn depends upon what specific flight-tests are to be conducted with the RPV. For examp if low-speed, high maneuverability performance is to be demonstrated, a lov pitch prop can be installed. If the emphasis is to be on high speed flight, a higher pitch prop can be used. Since the propellers are inexpensive and easily changed, many possibilities are open. We shall assume that propelle efficiencies of $\eta = 0.8$ can be achieved in any speed required through the appropriate propeller choice. Thus, the performance calculation will be made as if the craft had a variable pitch prop.

Static Thrust

For a ducted propeller, the slipstream does not contract behind the duct as it does with a free propeller. Thus, the ideal static thrust (negative swirl) can be calculated on the basis of the following two simple relationships.

$$\text{Thrust} = T = \rho V_s^2 A_s$$

$$\text{Power} = P = \frac{1}{2} \rho V_s^3 A_s \, (1/\eta^*)$$

Where V_s = slipstream velocity

A_s = slipstream (duct) area

η^* = static thrust efficiency of blades

$$\text{Thus,} \quad T = (\rho A_s)^{1/3} \, (2 \eta^* P)^{2/3}$$

For $P = 90$ H.P. , $\eta = 0.8$, $A_s = 12.6$ ft^2

$T = \underline{570\#}$ @MSL

Power Required

Figure (5.1) shows the power requirement vs. speed for two configurations.

i) $\Lambda = 0$

ii) $\Lambda = 45^{\circ}$

Top Speed

With the appropriate high advance ratio propeller, the followi top speeds should be attainable @ MSL

$\Lambda = 0 \quad V_{mx} = 155$ mph

$\Lambda = 45 \quad V_{mx} = 168$ mph

Cruise Speed

Again, with the appropriate propeller pitch, using 70% power the following cruise speeds can be achieved

$\Lambda = 0 \quad V_{cr} = 136$ mph

$\Lambda = 45^{\circ} \quad V_{cr} = 144$ mph

Stall Speed

From Figure (2.12), neglecting scale effects, untrimmed $C_{L_{mx}} = 1.0$ for the $\Lambda = 0$ and $\Lambda = 45^{o}$ configurations, therefore taking a nominal gross weight of 880 lbs. $V_{stall} = 59$ mph

Endurance

The specific fuel consumption for the McCulloch engine is estimated at

(SFC) @ 20-40 H.P. = 1.2

(SFC) @ 40-90 H.P. = 0.9

Thus, with 50 usable pounds of fuel on-board

E = 57 min. @ 140 mph, $\Lambda = 45$

E_{max} = 2 hrs. @ 80 mph, $\Lambda = 0$

Rate of Climb

Based on the power required curves, Figure (5.1), the rate of climb curves plotted in Figure (5.2) were obtained.

The best climb performance (approximate) for = 0 and 45 degrees is shown to be:

$\Lambda = 0$ R/C_{max} = 1640 Ft/Min. @ 80 mph

$\Lambda = 45$ R/C_{max} = 1510 Ft/Min. @100 mph

6. STRUCTURE

6.1 Materials

The primary and secondary structure consists of hand lay up fiberglas, and epoxy resin. Various types of cloth were used as described in detail following. Only one type of resin was used due to its high strength; dimensional stability and resistance to attack from most acids, chemicals and water.

6.2 Wing Structure

The wing primary structure consists of one main spar and a center ring. These items are the main load carrying members.

Materials used for the main spar and ring were style 7544 uniglas (manufactured by Thalco, Los Angeles, California). The cloth is an 18 oz. cloth of basket weave pattern. This cloth was selected because of its strength and pliability.

The resin used was Fiber Resin Corp.(Los Angeles, California) No. 5317L epoxy laminating resin and 5235 M hardener.

The physical properties of this laminate are:

Ult.	Compression Strength	– 45,000 p.s.i.
Ult.	Tensile Strength	– 58,000 p.s.i.
Ult.	Flexural Strength	– 62,000 p.s.i.
Ult.	Shear Strength	– 19,000 p.s.i.

The laminate construction is shown on Drawing 1126 Volume II. Four layers of cloth were used for the upper and lower cap areas and two (2) layers of cloth for the web areas in the region of the root. Starting at Station #6 and continuing toward the tips, fewer layers of cloth are used until, at the tip, only one layer is used.

The bending and torsional loads are distributed through the structure from Station #1 to Station #7 as a single cell beam, Figure (6.2). From Station #8 to the $\mathbb{C}_L$ of the aircraft the structure is a two (2) cell beam. Figur (6.3).

The moment of inertia of any Beam section between Station's 1 and 7 is,

$$I_x = 2\ btlh^2 + \frac{2}{3}\ t_2h^3$$

The material used to resist bending from Station #1 to Station #7 in the spar as depicted in Figure (6.4) as the cross hatched area.

The area of each element is,

$$A=btl + \frac{ht_2}{6}$$

In the fixed leading edge, two cell portion of the wing, the bending material is concentrated at points 5, 6, 7 and 8. Figure (6.3). The area concentrated at each point is, 50 t_3.

where, t_3 = skin thickness

The following stresses are based on a 10G loading condition.

The maximum bending stress of 7219 p.s.i. compression occurs at Station #11 in the forward top stringer of the beam.

The maximum toatal shear stress of 780 p.s.i. occurs in the front web of the beam at Station #11.

In the center ring the maximum bending stress of 11177 p.s.i. occurs in the ring at the $\mathbb{Q}$ of the airplane.

The maximum shear stress of 6089 p.s.i. occurs in the fixed leading edge skin at the $\mathbb{Q}$ of the airplane.

The removeable leading edge was made from 7 1/2 oz. boat cloth and 5317L epoxy resin. The leading edge was designed to transfer its load through skin structure only. Figure (6.4)

The frangible wing tips were made from a 4 oz., style 120 fabric of .004 thickness, molded to contour and filled with a two (2) pound density Polyurethane foam.

Wing ribs are laid up from 7 1/2 oz. boat cloth. Two layers of cloth were used to give a rib thickness of .040.

6.3 Duct

The duct structure is made up of two 2024-T3 aluminum rings which comprise a front and rear beam. Ribs and outer skin are laid up to a thickness of .040 from 7 1/2 oz. boat cloth.

The duct is made in two halves, an upper and lower half. These halves are joined by bolts through the front and rear beams into fittings in the central rotating disc. The duct loads are therefore transmitted through the fittings and rollers into the wing structure.

6.4 Tail Surfaces

Horizontal Tail

The horizontal tail skin is laid up from 7 1/2 oz. boat cloth to a thickness of .025. This outside shell is then filled with a two (2) pound density Polyurethane foam. Each horizontal tail section half is fastened by screws to a magnesium rib, fitting.

The bending loads are reacted by the skins. The skin bending stress in compression and tension is 890 p. s. i. Skin buckling in bending and torsion is not considered to be any criteria due to the fact the foam in its adhesion to the fiberglas skin stiffens the skin considerably. The vertical shear is carried by the foam core. Maximum vertical shear stress is 12.5 p. s. i.

Vertical Tail

The vertical tails primary structure consists of a fore and aft beam. The beam thickness is .125. The vertical tail skin is laid up from two layers of 7 1/2 oz. cloth to a thickness of .050.

The vertical tail tip is a .004 thick fiberglass skin filled with a two (2) pound density polyurethane foam. This tip section is a frangible portion of the vertical tail.

Vertical tail torsional loads are reacted by two (2) struts leading from the duct to the upper part of the vertical tail.

6.5 Landing Gear

The main landing gear is made from a 5/8" thick 7075-T56 aluminum alloy strip. Landing gear loads are reacted through the side duct fittings and transferred to the wing structure via the central ring.

The maximum landing load is a 4 G loading condition.

7. PRELIMINARY TESTING

FORT IRWIN, CALIFORNIA
NOVEMBER 12-16, 1973

The tests planned for this period consisted of a series of ground tests to evaluate the performance of all RPV systems, and a series of flight tests to determine flying qualities and to further demonstrate the operation of the RPV systems. In summary, all ground tests, including some taxiing, were completed in the first three days. A certain amount of time was spent during this period in adjustments to the controls and modifications to the video system and instrumentation as problems were encountered.

The last two days were spent taxiing in an effort to improve ground handling and to find a reliable method for straight line taxiing for takeoff run and landing rollout. R/C techniques were thought to be insufficient for this task since the required length of takeoff run would place the vehicle out of effective visual range for takeoff. The method adopted was to give a second operator the nose camera display and steering-only control for taxiing purposes.

The tests ended on Friday, November 16, when a loss of video signal resulted in a ground loop and moderate damage.

A summary of each day's activities follows:

---------- MONDAY, NOV. 12 ----------

Unloaded and assembled RPV.

Changed compass connections.

Calibrated yaw indicator.

Video transmitter blew fuse - replaced with larger fuse after consulting manufacturer.

Calibrated camera tilt indicator.

Verified head and exhaust temp indicators.

Connected S-meter.

Verified three chute modes.

Trimmed surfaces.

---------- TUESDAY, NOV. 13 ----------

Assembled and verified tracking system.

Operated all systems, vehicle tethered, engine running.

Verified auto-homing command.

Measured unusable fuel (~2 lbs).

Tested chute firing with engine running
(blows 3A fuse)
5 times on command
3 times on loss of signal

Starter nut came off - added cotter pin

Tuesday, Nov. 13 (continued)

Range check to far end of lake (1.6 mi.)

Command solid - engine running
tracking good
video weak on receiving dipole

Noted head temp, exhaust temp, and tachometer -

no good with engine running and transmitters on.

Propeller damaged by rocks - patched with epoxy.

Ran battery test (see results).

Checked video for possible attenuation by leading edge.

---------- WEDNESDAY, NOV. 14 ----------

Fixed head temp, exhaust temp and tachometer rf interference.

Set up for taxi tests.

Taxi 1. Engine killed on apparent chute deploy command - cause unknown.

Taxi 2. Taxi in large circles - max. speed 30 mph, approx. 5 min.
max head temp = 310°F.

Taxi 3. Same - approx. 5 min. - noted tendency for turns to tighten up.

Wind increased - returned to hangar.

WEIGHING RESULTS

NO FUEL

STBD GEAR	365 Lb.
NOSE GEAR	116 Lb.
PORT GEAR	366 Lb.
TOTAL	847 Lbs.

C.G. = 7.46 fwd. main gear
= 27.8% chord

BATTERY TEST RESULTS

The following items operating:

Command System (Manual Mode)

Vacuum Pump

1.8 GHz Transmitter

240 MHz Transmitter

Total load is approximately 15A.

ELAPSED TIME, MIN.	BATTERY VOLTAGE
0	24.0
5	23.3
10	23.0
15	22.8
20	22.6

Wednesday, Nov. 14 (continued)

WITH 230 LB. FUEL

STBD GEAR	365
NOSE GEAR	140
PORT GEAR	371
TOTAL	876

Drop test from 7" blocks ok.

Drop test from 12" blocks - STBD gear fell off block prematurely - wheel contacted ground and broke - no other damage.

---------- THURSDAY, NOV. 15 ----------

Installed new STBD gear.

Modified command system for steering - only control from console.

Removed mufflers.

Engine covers off as for previous taxi tests.

Tethered static tests

Thrust = 290 - 300 lb.
approx 3800 rpm
full rich mixture.

Set up for taxi tests.

Tried straight runs using distant land marks.

Tried following line on lake.

In all cases, very active control was necessary - ground track very sinuous often ending in spin-out.

Thursday, Nov. 15

Two problems:

1) poor ground handling

2) poor picture quality

Tried runs with chase car, noted airspeed indicator

50 mph + 5 mph ⟶ 32 kts indicated
car wind

Returned to hangar.

Modified video to free-running mode.

Removed and repaired STBD elevon servo for less free action.

---------- FRIDAY, NOV. 16 ----------

Removed autopilot card because of noted tendency to enable autopilot without command.

Reduced nose gear tire pressure to improve straight running tendency

Main - 27 psi

Nose - 13 psi

Tried hands-off taxi at low speed - noted large trim change with power - runs fairly straight power on.

Tried taxiing with auto chase, nose camera only display for second operator.

Noted improved handling and picture quality.

Straight runs possible using terrain for reference - active control necessary handling poor with power off.

Make four full power runs - each apparently better with operator gaining ski

Last run 17 sec. - 70 mph.

Video signal lost at same time as throttle was shut down - vehicle ground looped in tight turn to left.

LIST OF FIGURES

FIGURE 1.1	Oblique Wing Remotely Piloted Research Vehicle
FIGURE 2.1	Remotely Piloted Vehicle Yawed Wing
FIGURE 2.2	Wing Airfoil Section
FIGURE 2.3	Stability Axes
FIGURE 2.4	Lift Coefficient (Theory)
FIGURE 2.5	Lift Slope Variation with Λ (Indep. Of α)
FIGURE 2.6	Aerodynamic Center Travel
FIGURE 2.7	Wind Tunnel Model
FIGURE 2.8	Tuft Photos, $\Lambda = 0^{\circ}$
FIGURE 2.9	Tuft Photos, $\Lambda = 45^{\circ}$
FIGURE 2.10	Lift Coefficient Squared
FIGURE 2.11	Logitudinal Characteristics No Elevator
FIGURE 2.12	Lift As A Function Of Angle Of Attack (No Elevator)
FIGURE 2.13	Elevator Control Of Pitching Moment
FIGURE 2.14	Lift As A Function Of Angle Of Attack (No Elevator)
FIGURE 2.15a	Longitudinal Characteristics Λ =45° No Elevator
FIGURE 2.15b	Longitudinal Characteristics Λ =45° With Elevator
FIGURE 2.16	Wing Yaw, deg.
FIGURE 2.17	Yaw Restoring Moment
FIGURE 2.18	Aileron Effectiveness Λ =0 No Elevator
FIGURE 2.19	Yawing Moments Λ =45 deg.
FIGURE 2.20	Tip Stabilizer

LIST OF FIGURES (Continued)

FIGURE 2.21	Tip Stabilizer Incidence Angle Required To Trip $\Lambda = 45^{\circ}$ Craft @ $\psi = 0$
FIGURE 2.22	Elevon Control of Roll $\Lambda = 45^{\circ}$
FIGURE 2.23	Aileron Trim Angle Vs. α
FIGURE 2.23a	Parts/Instructions
FIGURE 2.24	Unpowered Model Launch/Net Recovery $\Lambda = 50^{\circ}$
FIGURE 2.25	Redesigned Tip Stabilizer Equilibrium Incidence Angle (Theory)
FIGURE 3.1	Avionics System Block Diagram
FIGURE 3.2	Autopilot Supply Card (#1)
FIGURE 3.3	Gyro Interface Card (#2)
FIGURE 3.4	Elevator Signal Synthesizer Card
FIGURE 3.5	Auxiliary Select Card (#6)
FIGURE 3.6	Auxiliary Delay/Decode Card (#7)
FIGURE 3.7	Meter Card (#8)
FIGURE 3.8	Priority Control Card
FIGURE 3.9	Priority Drive Card (#10)
FIGURE 3.10	Proportional Servo Amplifier Card
FIGURE 3.11	Positionable Servo Amplifier Card
FIGURE 3.12	Electrical Schematic
FIGURE 3.13	Relay Panel
FIGURE 3.14	Instrument Panel
FIGURE 3.15	Instrument Package

FIGURE 3.16 Nose Camera

FIGURE 3.17 Video Encoder (Inst. Pkg.)

FIGURE 3.18 RPV Control Diagram (Pitch)

FIGURE 3.19 Flight Control Circuit (Control Circuit)

FIGURE 3.20 Auxiliary Select Panel

FIGURE 3.21 T.V. Receiver

FIGURE 3.22 Video Decoder (Nose Monitor)

FIGURE 3.23 Tracking Antenna

FIGURE 3.24 Aircraft Auto Tracking Block Diagram

FIGURE 3.25 Tracking Amplifier, 240 MHZ

FIGURE 3.26 Aircraft Auto Return Steering Block Diagram

FIGURE 3.27 Typical Aircraft Path, With Auto Return Steering

FIGURE 5.1 Power Required η =0.80

FIGURE 5.2 Climbing Performance

FIGURE 6.1 Ring Spar Layout

FIGURE 6.2 Single Cell Sections

FIGURE 6.3 Double Cell Sections

FIGURE 6.4 Spar Cap Geometry

FIGURE 6.5 Leading Edge Loads

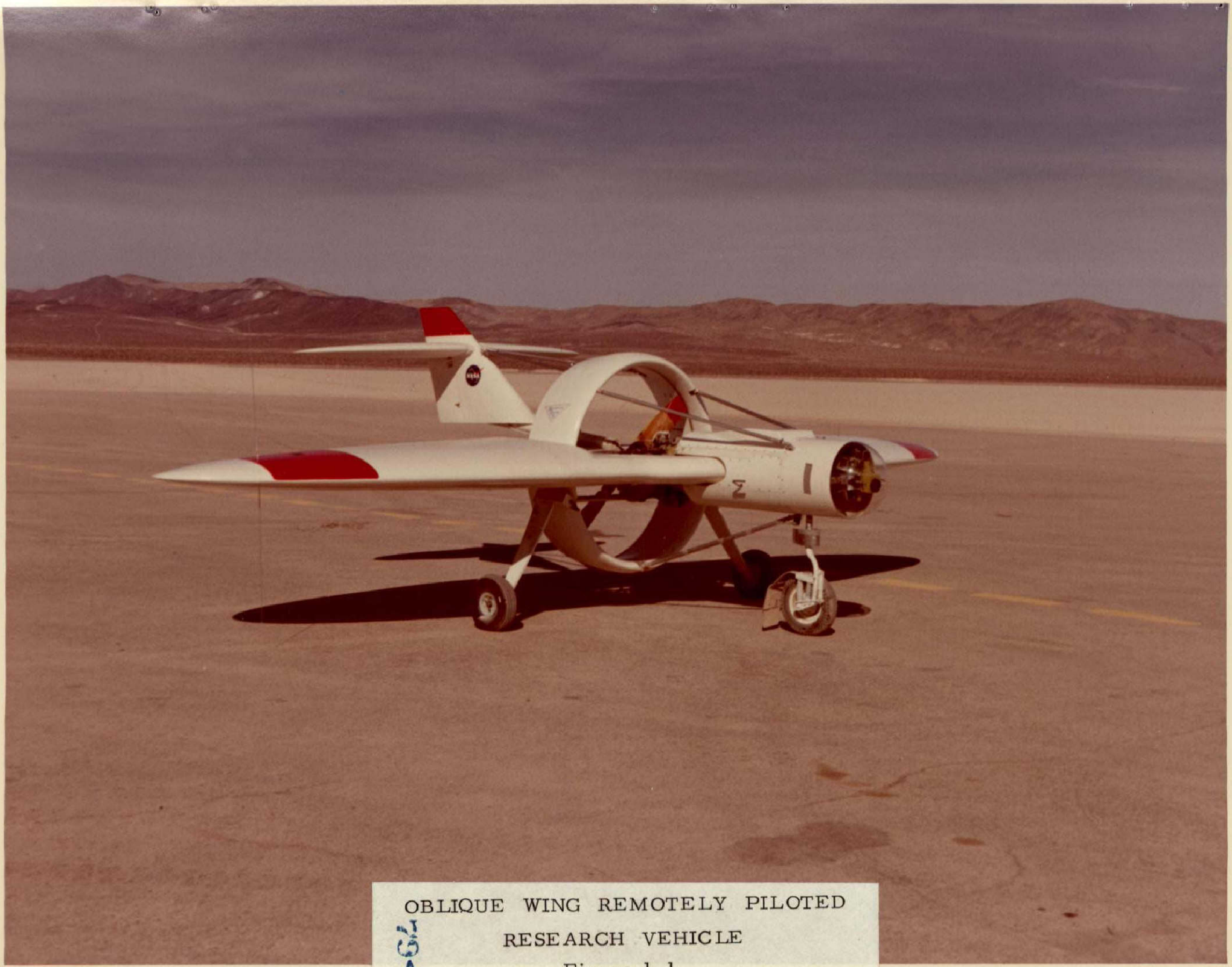

OBLIQUE WING REMOTELY PILOTED
RESEARCH VEHICLE
Figure 1.1

FOLDOUT FRAME 1

FOLDOUT FRAME 2

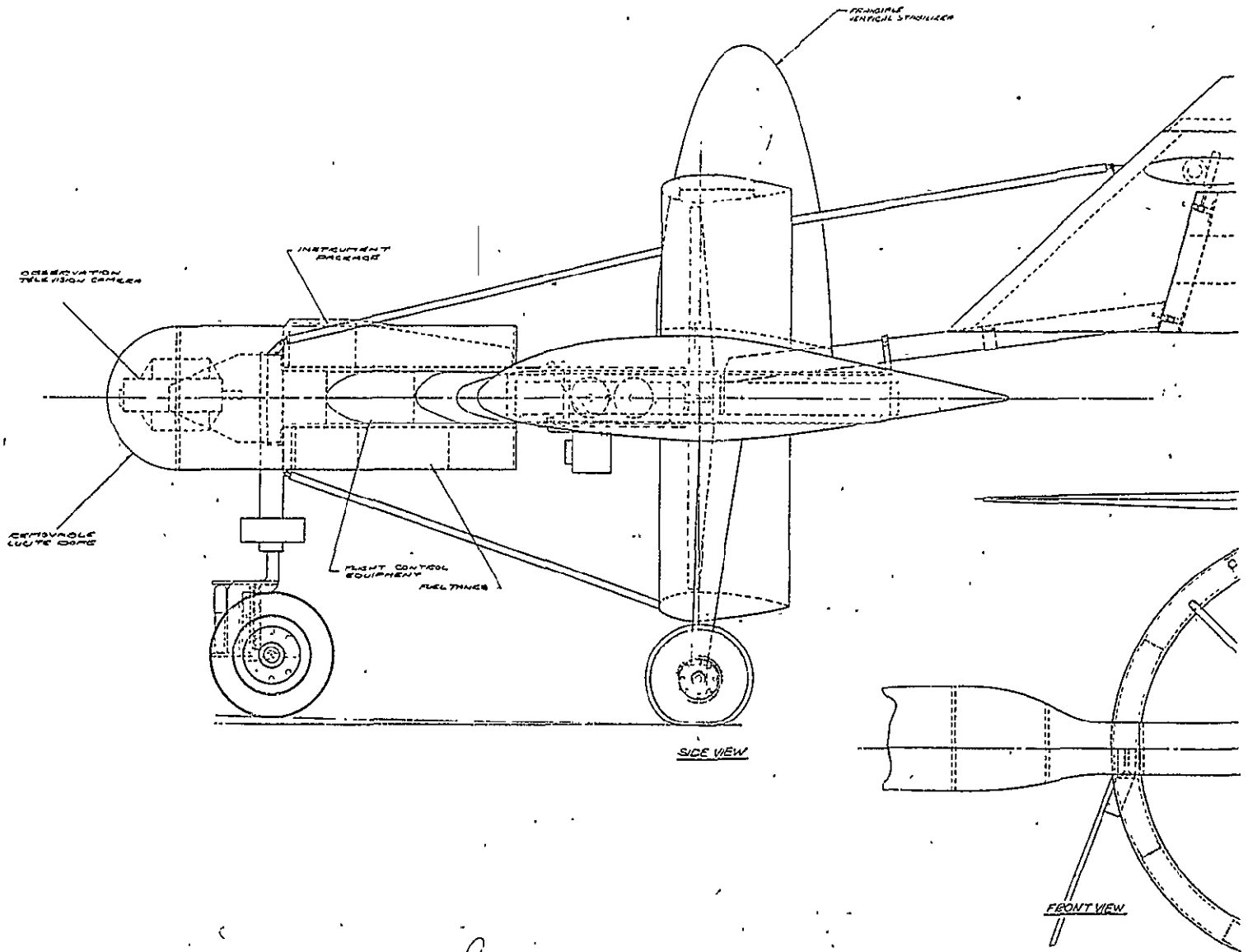

FOLDOUT FRAME 2

FOLDOUT FRAME 3

FOLDOUT FRA

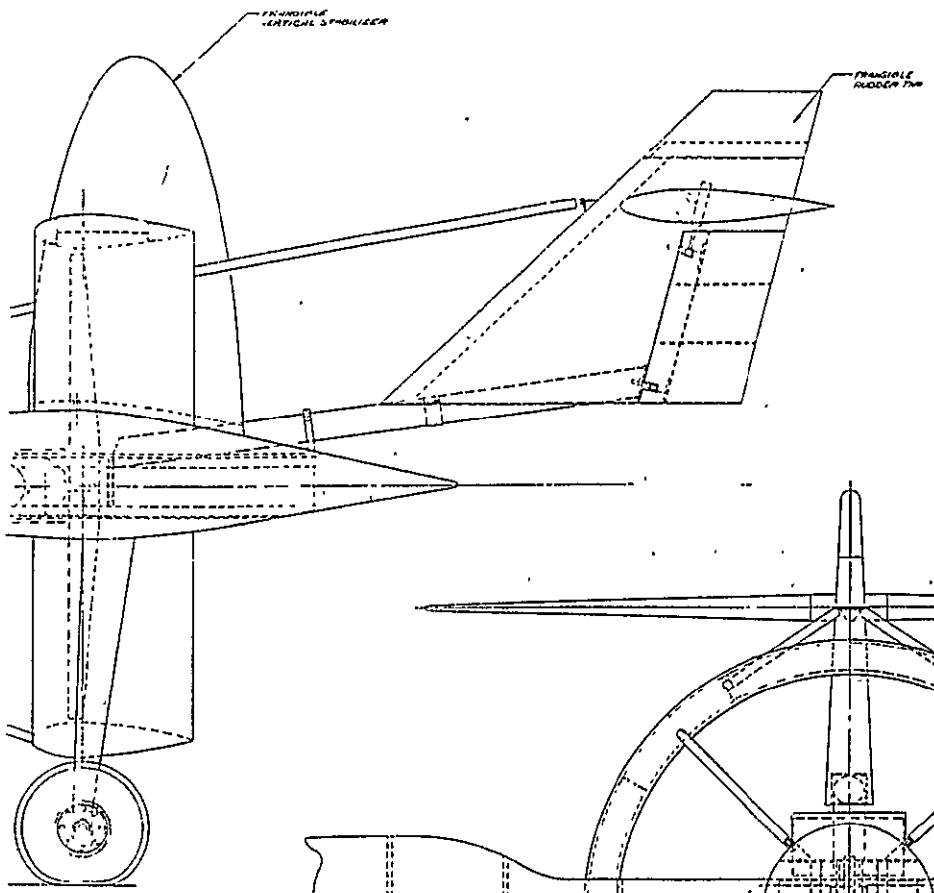

SIDE VIEW

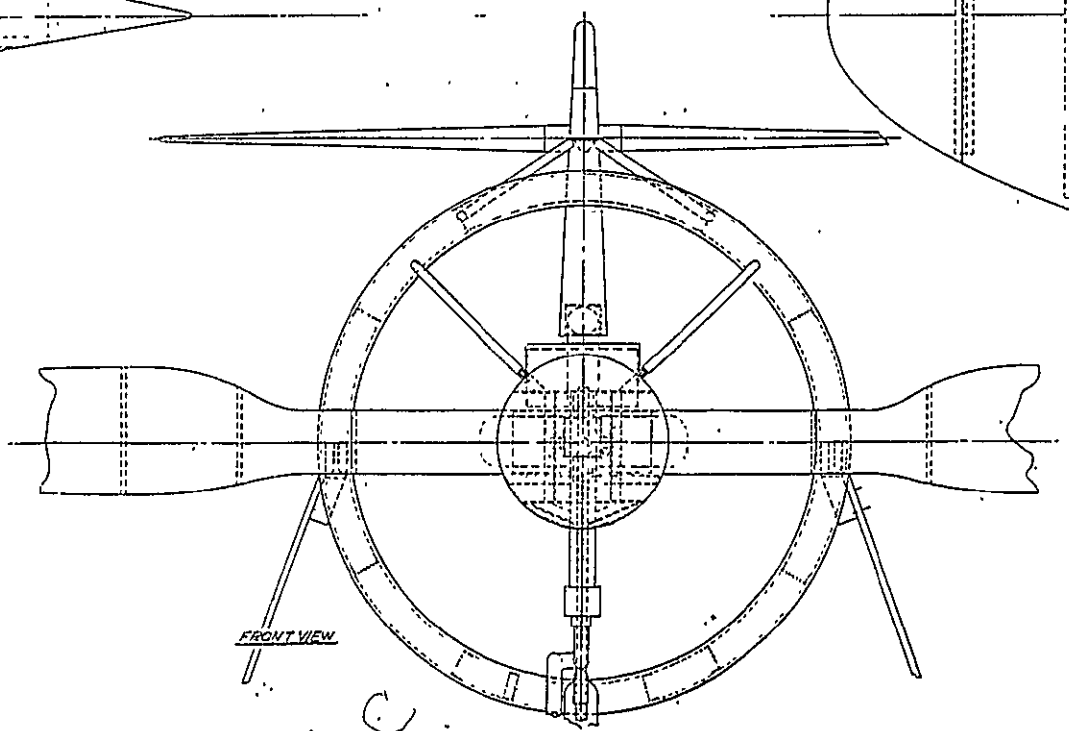

FRONT VIEW

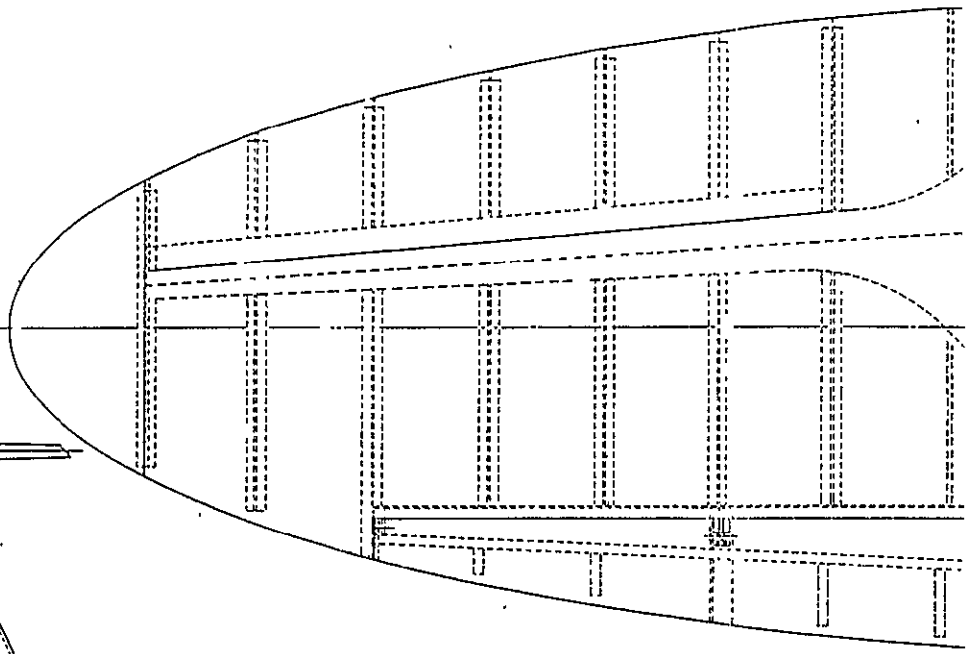

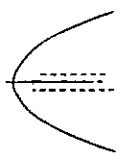

C

D

FOLDOUT FRAME 5

FOLDOUT FRAME 6

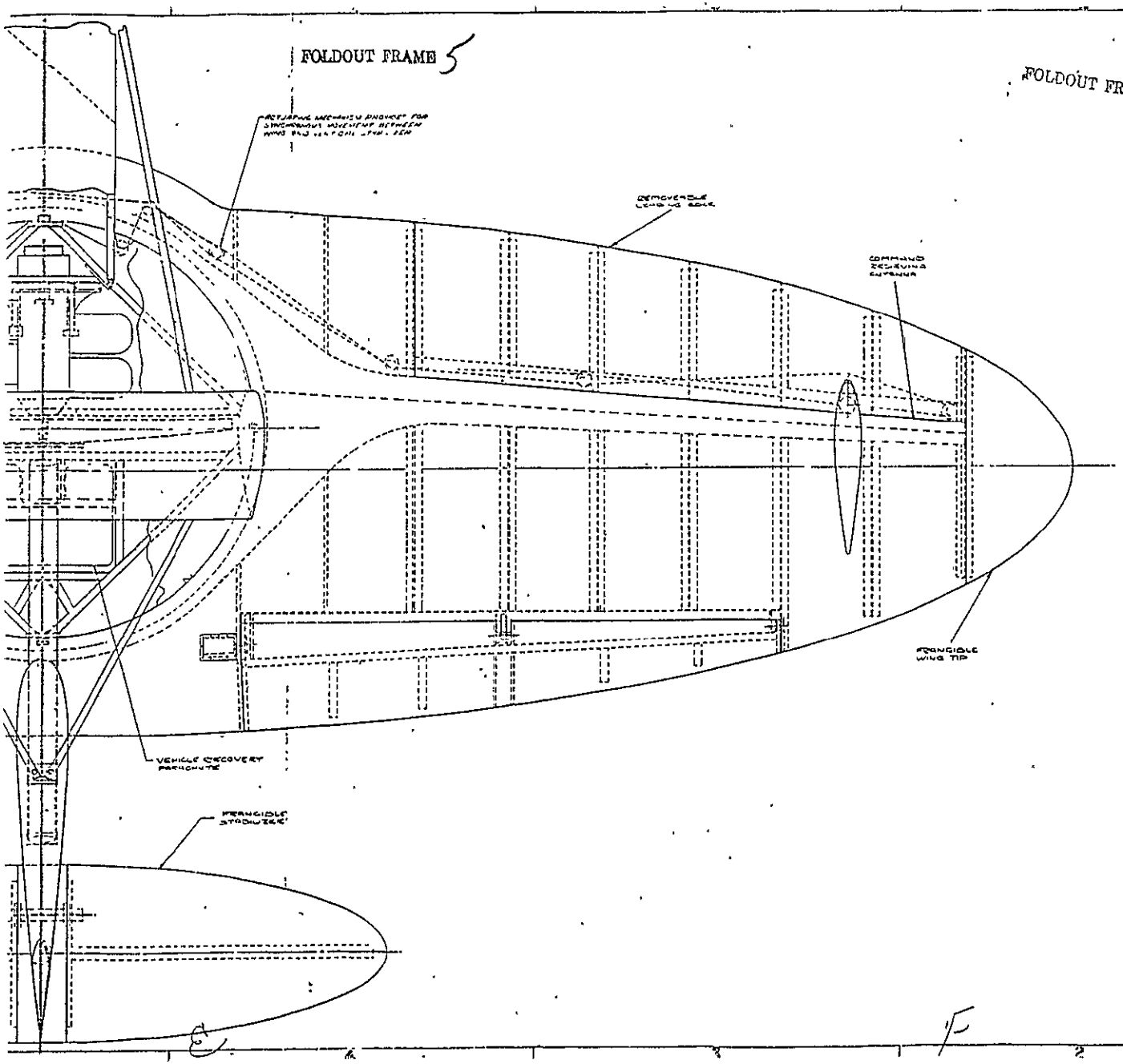

SPECIFICATIONS

EMPTY WEIGHT	847 LB
PAYLOAD	150 LB
FUEL CAPICITY	60 LB
MAX GROSS WT	1060 LB
AVAILABLE POWER	90 BHP @ 4200 RPM
PROPELLER DIA	49.5 in.
WING SPAN	268 in
ROOT CHORD	68.5 in
WING AREA	99.6 FT²
ASPECT RATIO	5.0

Figure 2.1

DEVELOPMENTAL SCIENCES, INC.
REMOTELY PILOTED VEHICLE - YAWED WING
1038

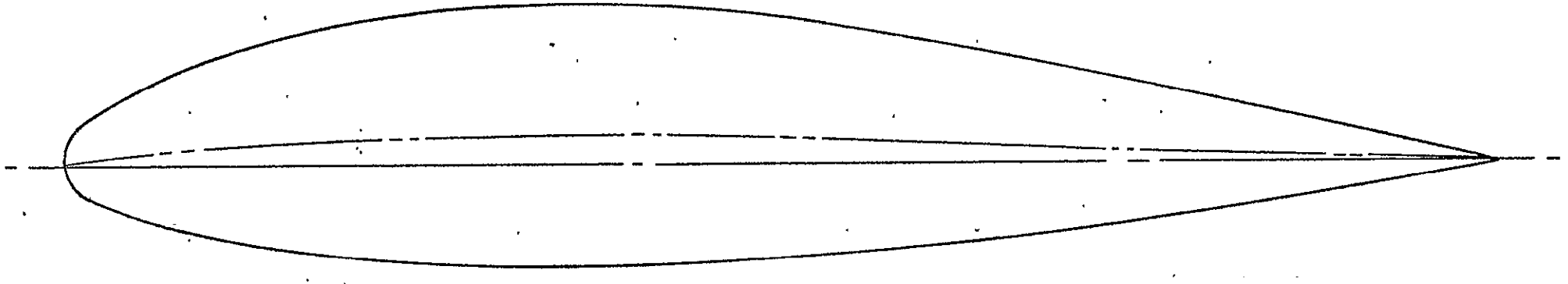

WING AIRFOIL SECTION

FIG. 2.2

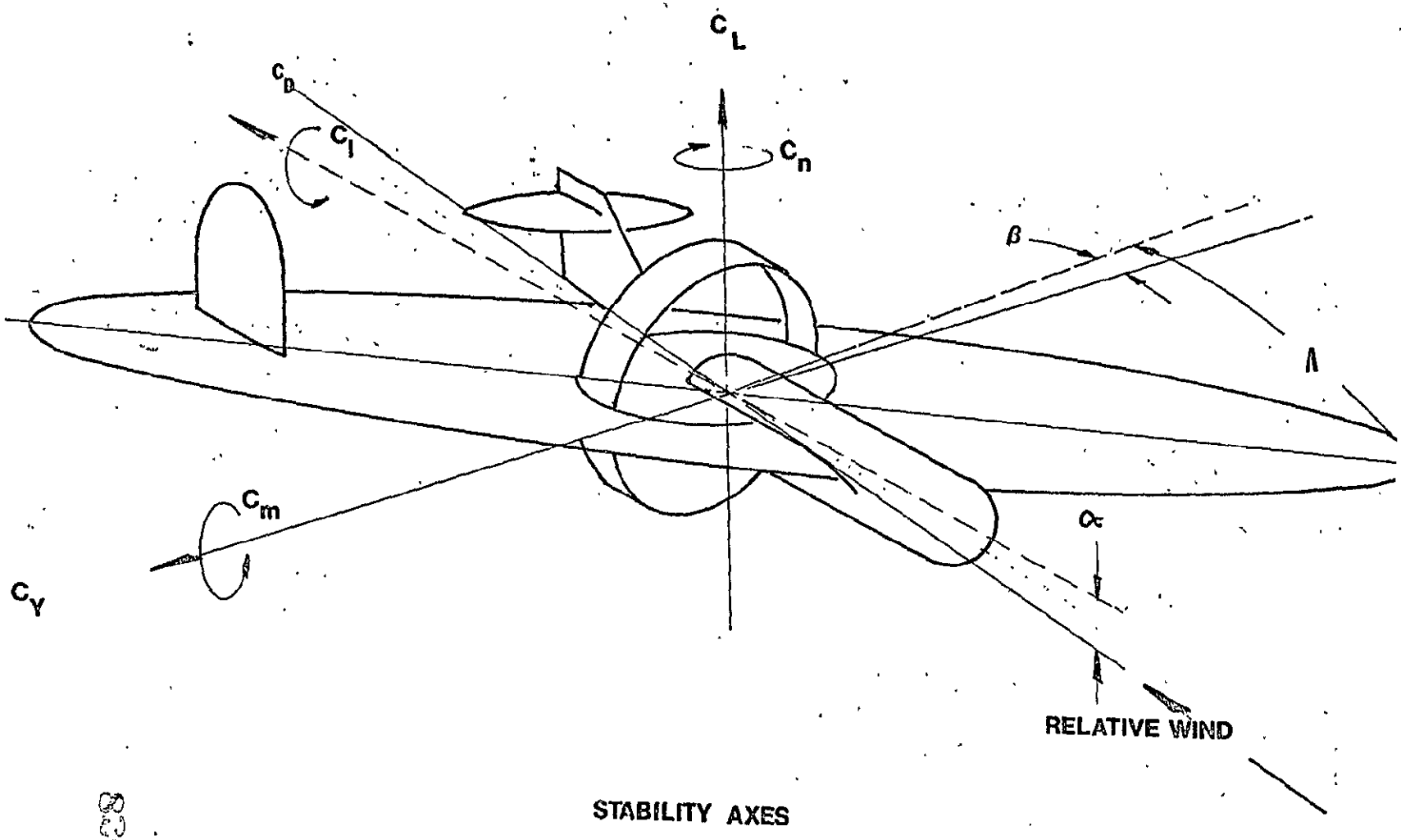

STABILITY AXES

FIGURE 2.3

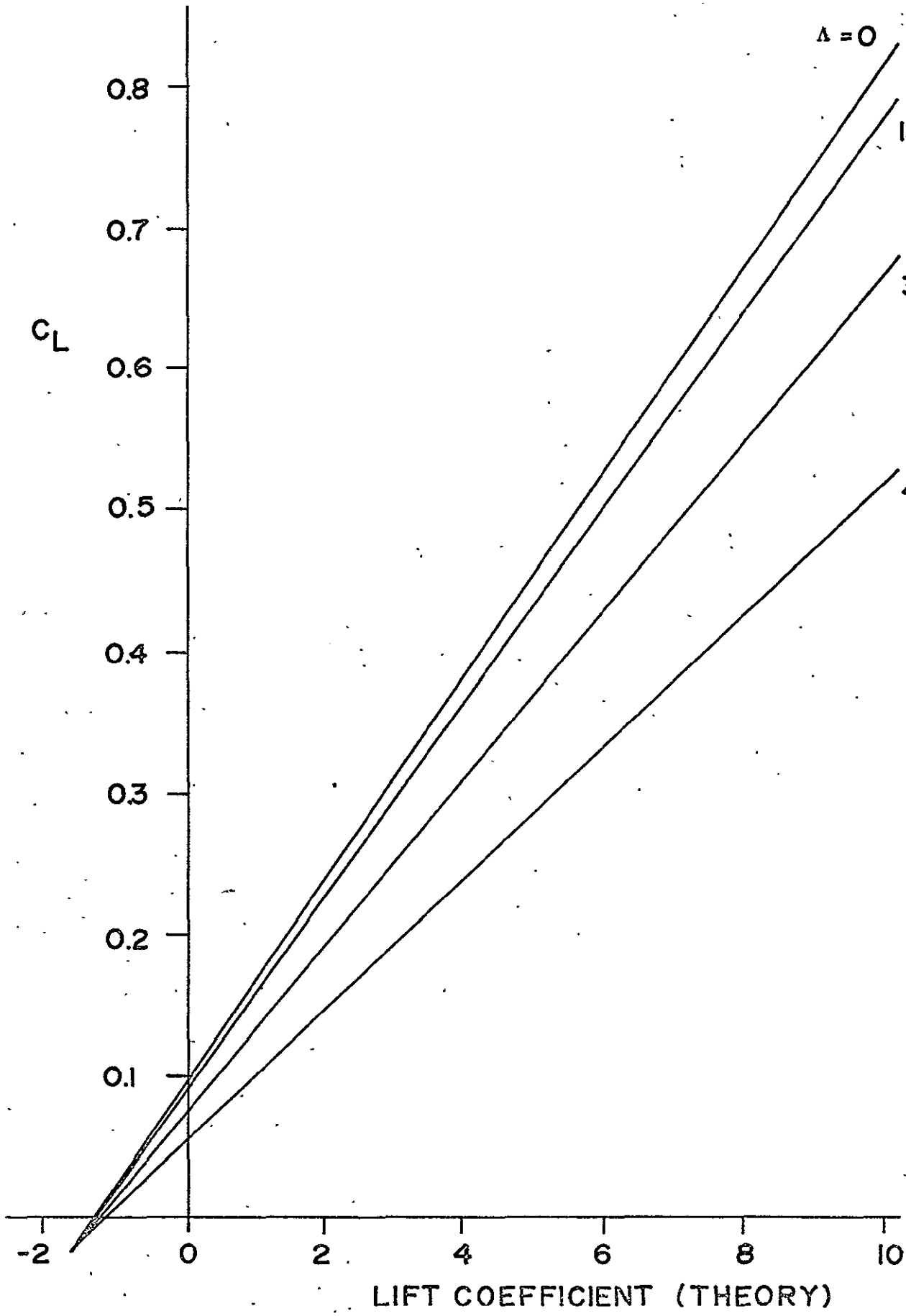
Λ = 0
15°
30°
45°
0.8
0.7
0.6
0.5
0.4
0.3
0.2
0.1
C_L
-2
0
2
4
6
8
10
LIFT COEFFICIENT (THEORY)

FIGURE 2.4

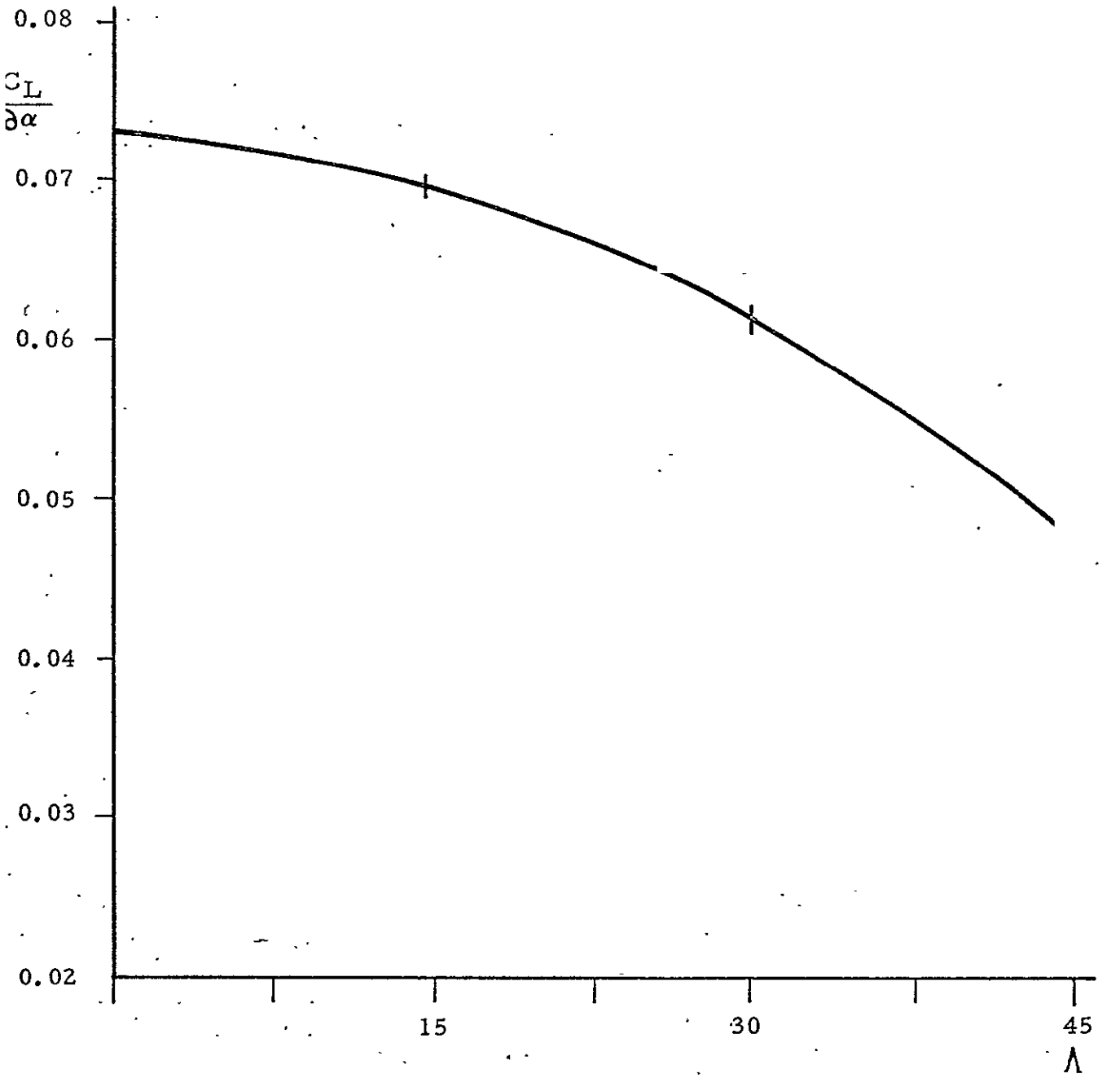

LIFT SLOPE VARIATION
WITH Λ (INDEP. OF α)

84

FIGURE 2.5

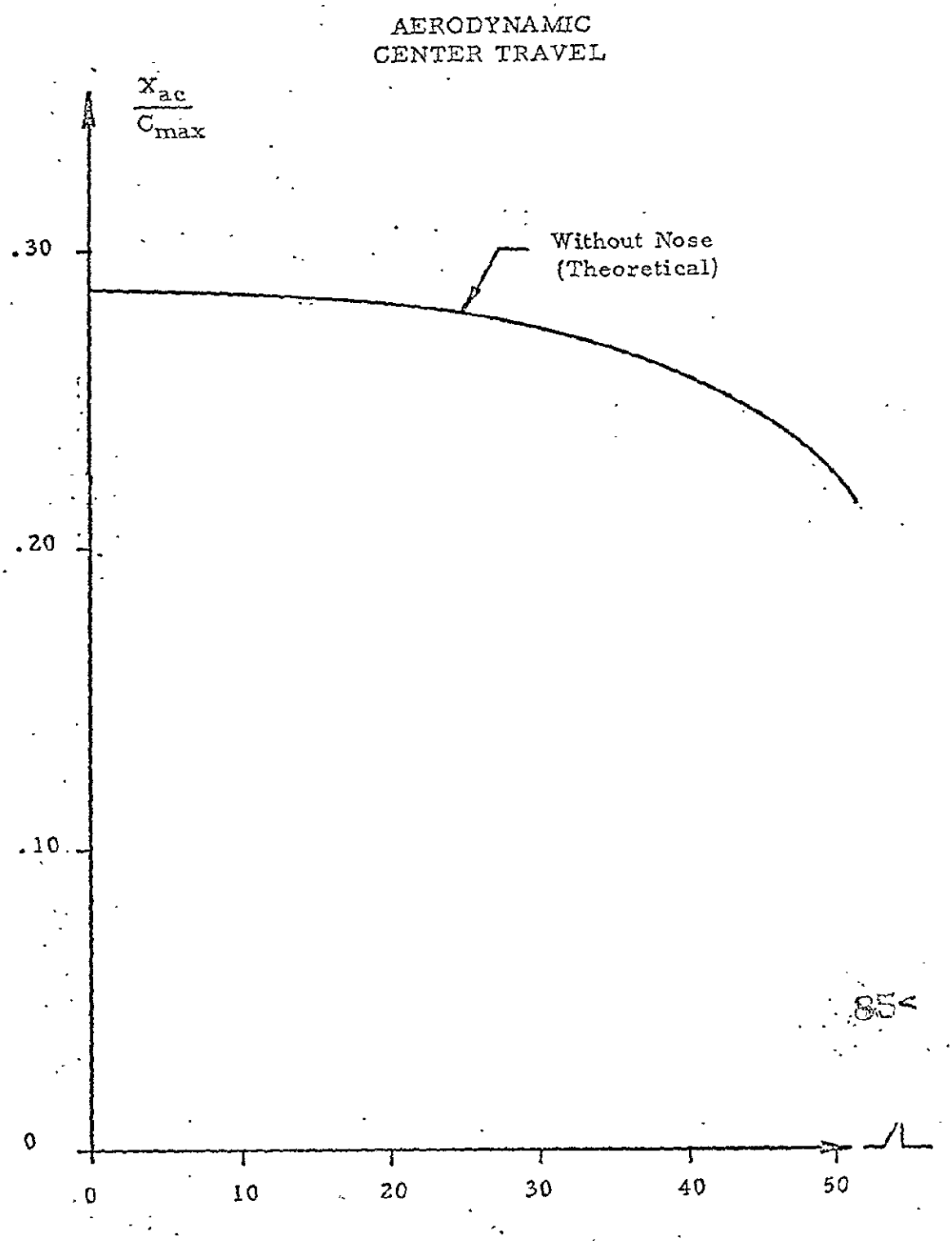
AERODYNAMIC
CENTER TRAVEL
$\frac{x_{ac}}{c_{max}}$
.30
.20
.10
0
Without Nose
(Theoretical)
0
10
20
30
40
50
85<

FIGURE 2.6

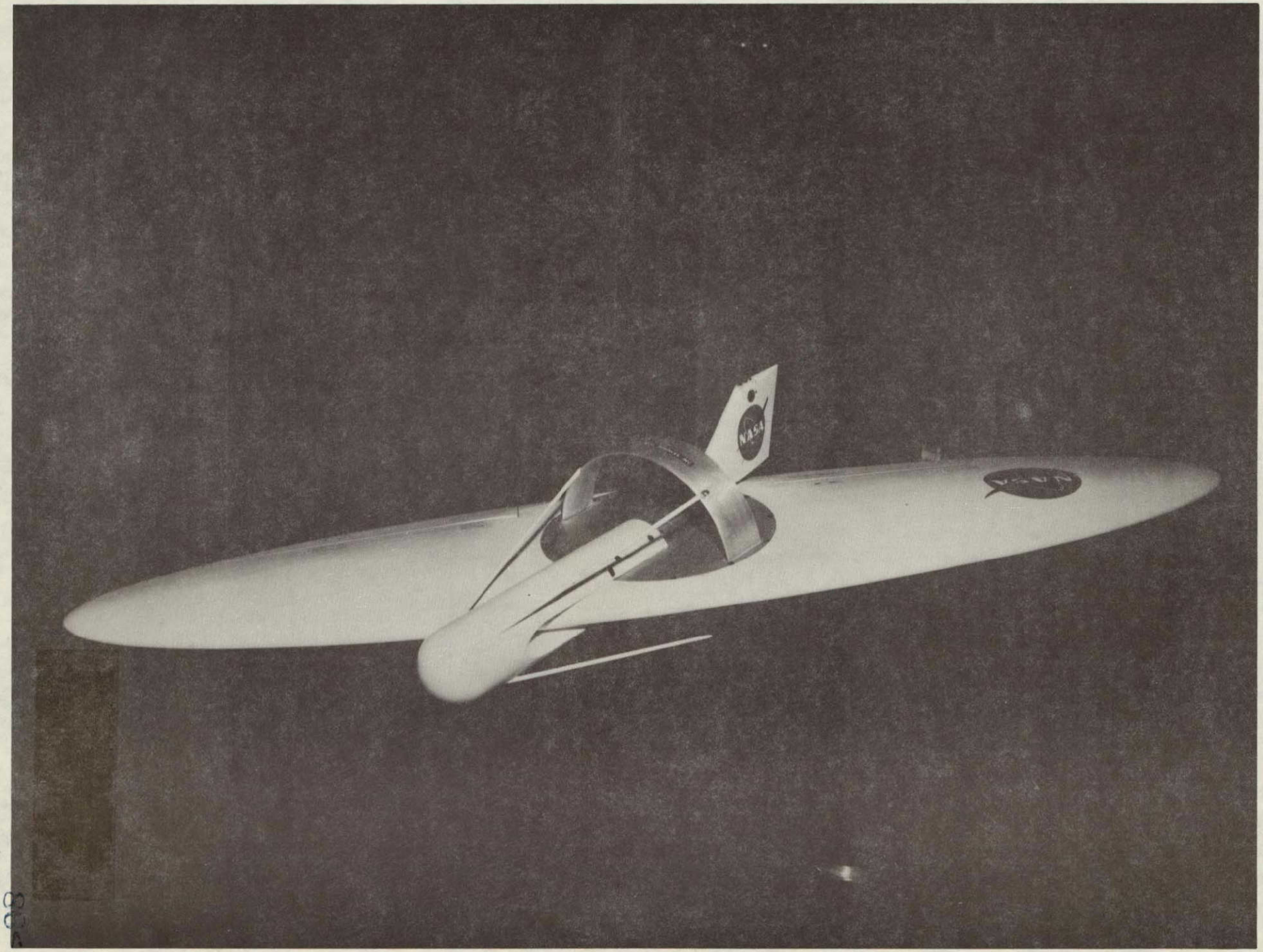

FIGURE 2.7

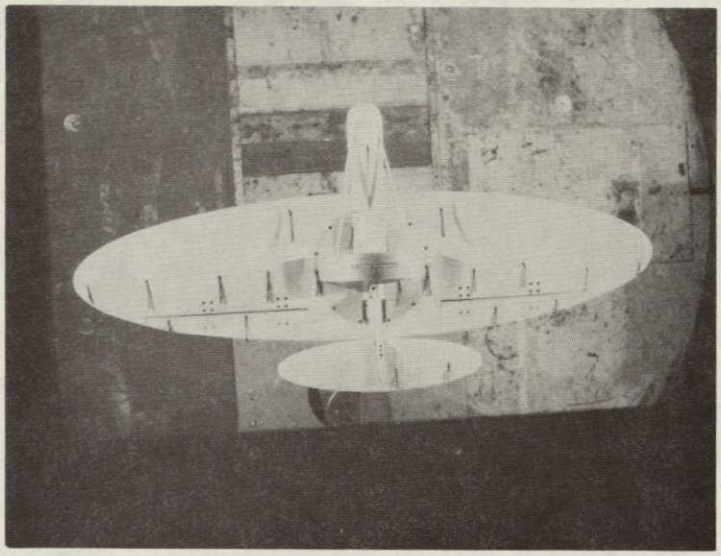

$\alpha = 0^{\circ}$

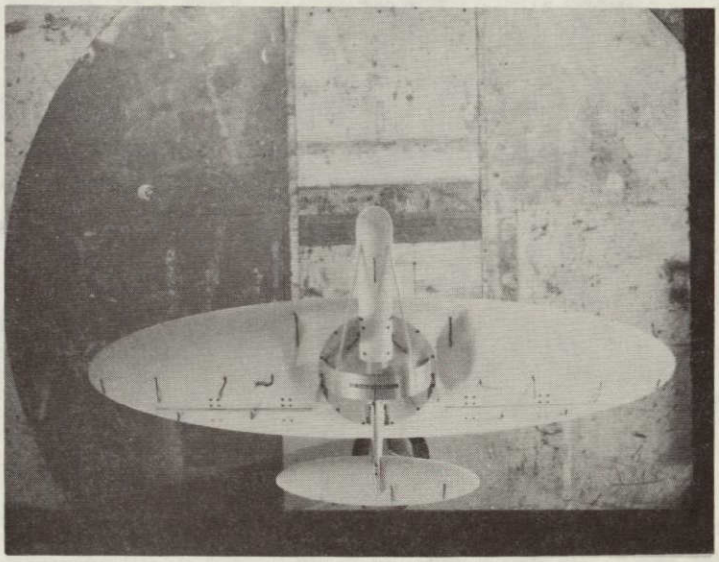

$\alpha = 15^{\circ}$

87<

TUFT PHOTOS, $\Lambda = 0^{\circ}$

FIGURE (2.8)

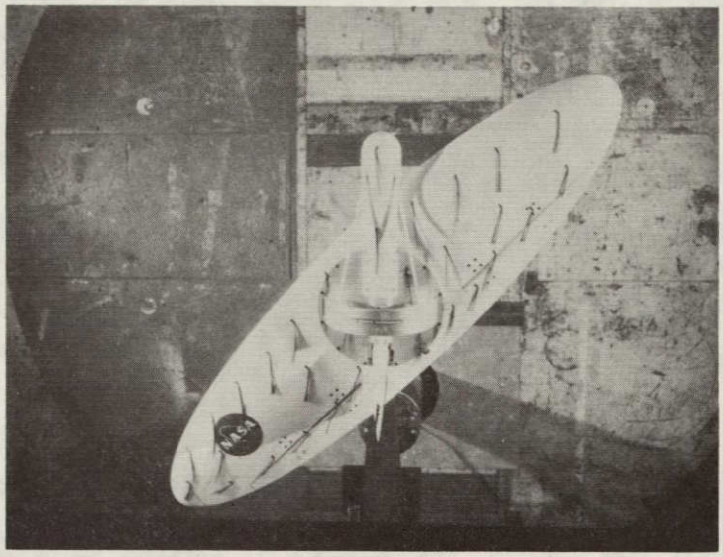

$\alpha = 10^{\circ}$

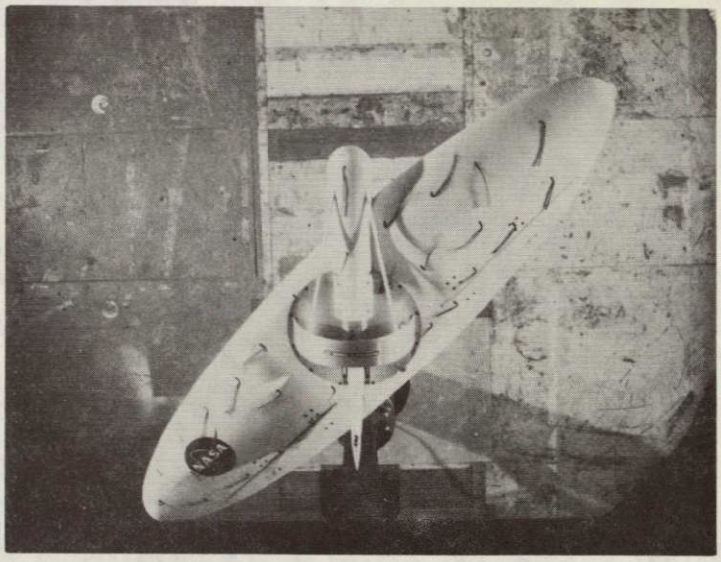

$\alpha = 20^{\circ}$

TUFT PHOTOS, $\Lambda = 45^{\circ}$

FIGURE (2.9)

ITEM PART

1. ROD AL .250 OD LENGTH 56.0 7075-T6 5 REQUIRED
2. BRACKET, AL .030 x 1.0 x 1.25 6061-T6
3. BLOCK, AL 1.0 x 2.0 x 3.0 6061-T6
4. SUPPORT TUBE, AL .050 WALL, 1.00 OD, 20. 6061-T6
5. STRAP, BRASS .030 .250 x 5.0
6. INSULATOR SLEEVE .750 OD, .250 ID LENGTH 1.00 NYLON
7. CONNECTOR 50 239

NOTES

1. WELD ITEM 3 TO 4
2. ATTACH 7 TO 2 WITH 4-40 x 1/2 SCREWS
3. PRESS FIT ITEMS 3 6 1.
4. SOLDER BRASS STRAP TO 7 AND CLAMP OTHER END TO VERTICAL ROD
5. ADJUST LENGTH OF VERTICAL ROD FOR MINIMUM V.S.W.R. AT 49.78 MHZ

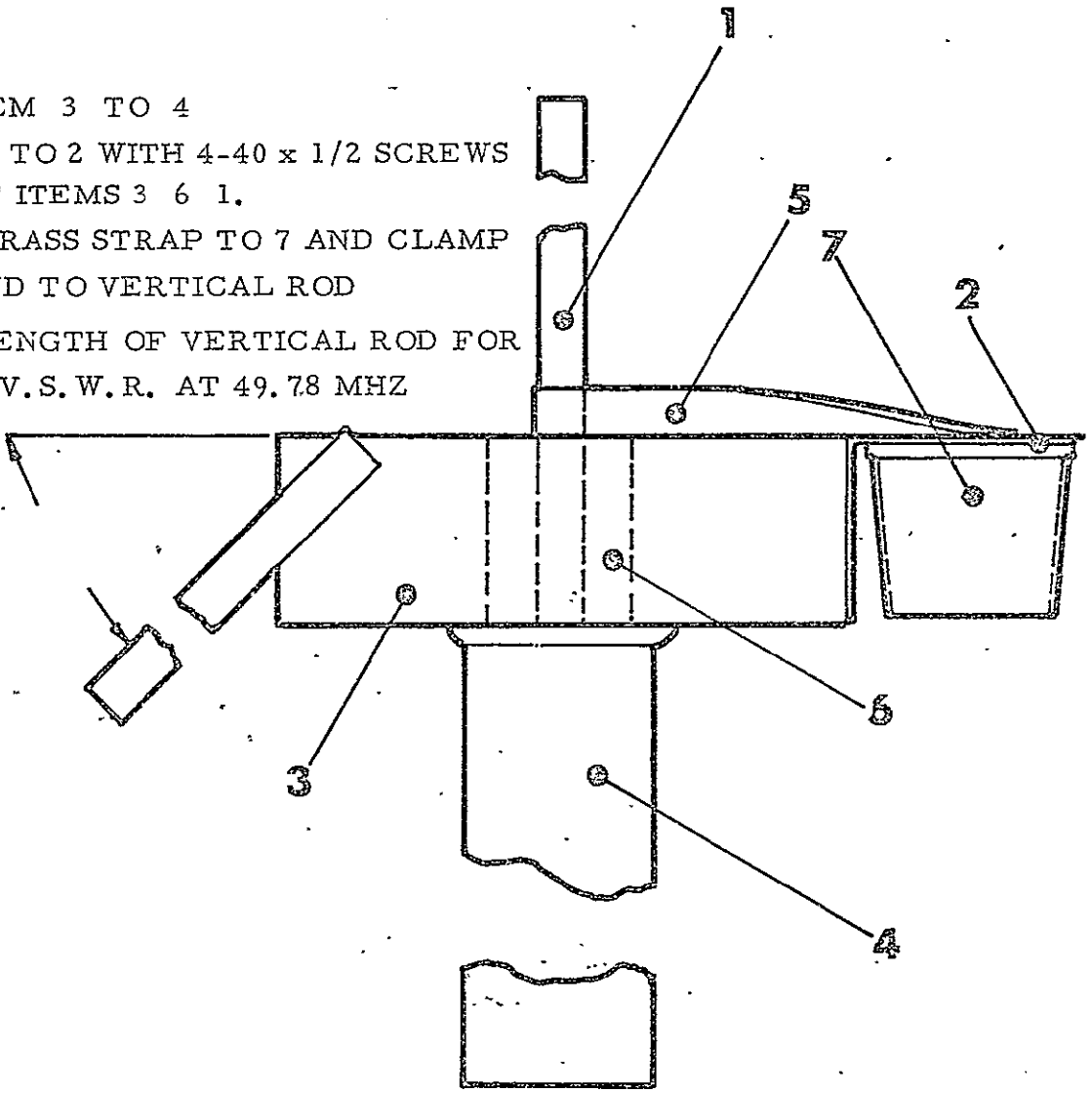

89<

FIGURE 3.23 a

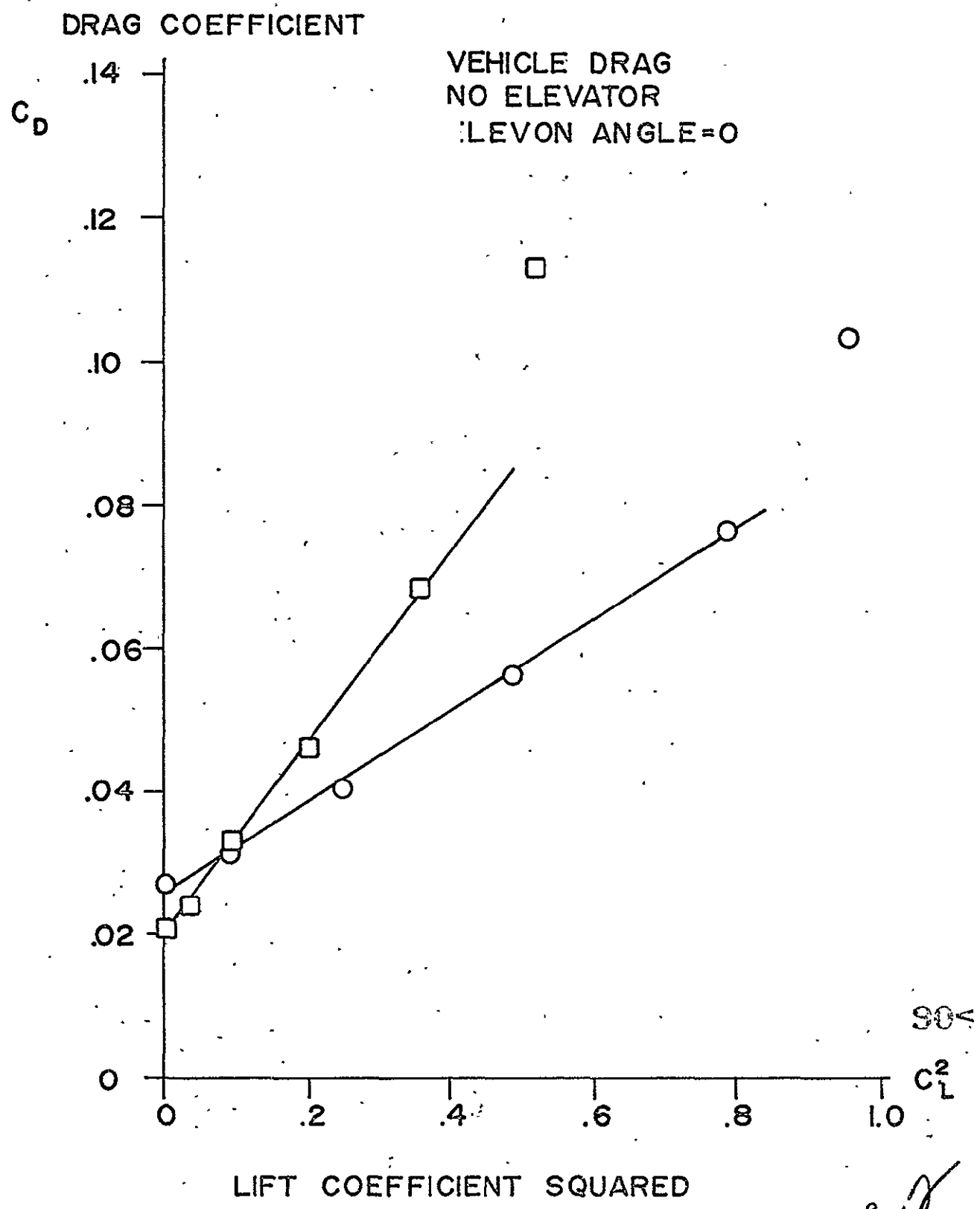
DRAG COEFFICIENT
C_D
VEHICLE DRAG
NO ELEVATOR
ELEVON ANGLE=0
.14
.12
.10
.08
.06
.04
.02
0
0
.2
.4
.6
.8
1.0
C_L^2
LIFT COEFFICIENT SQUARED

FIGURE 2.10

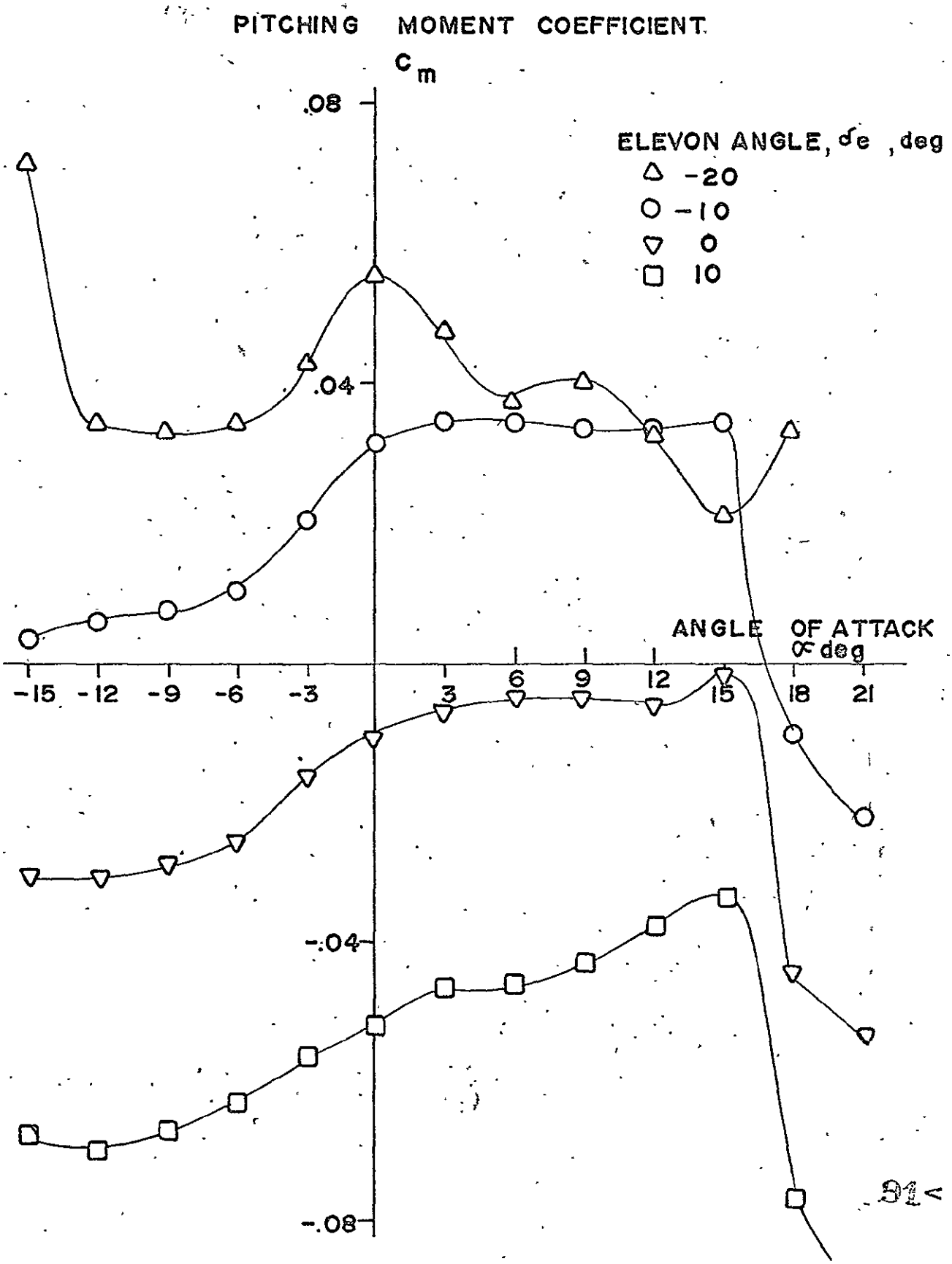

LONGITUDINAL CHARACTERISTICS NO ELEVATOR $\Lambda=0$

FIGURE 2.11

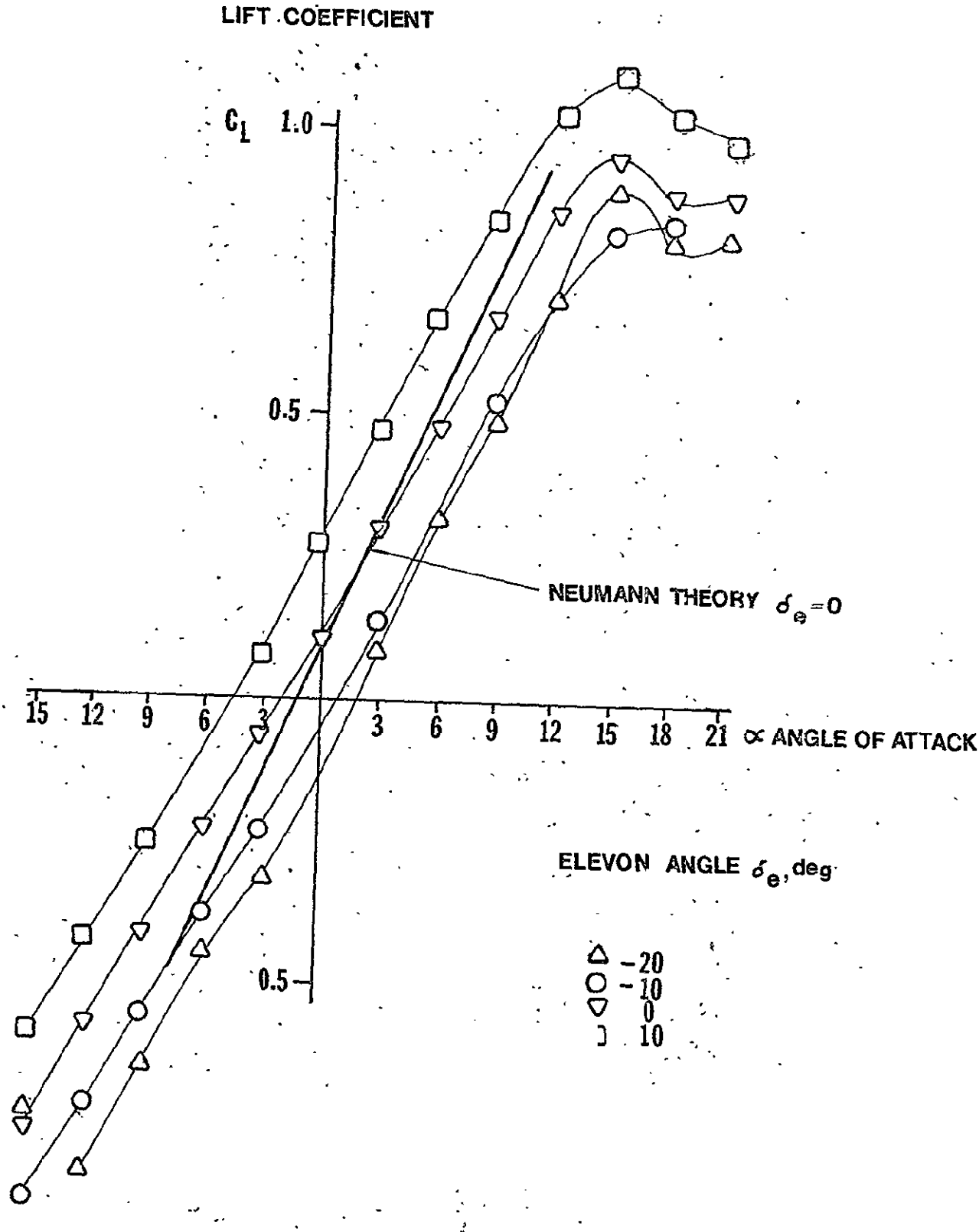

LIFT AS A FUNCTION OF ANGLE OF ATTACK
(NO ELEVATOR)

92<

FIGURE 2.12

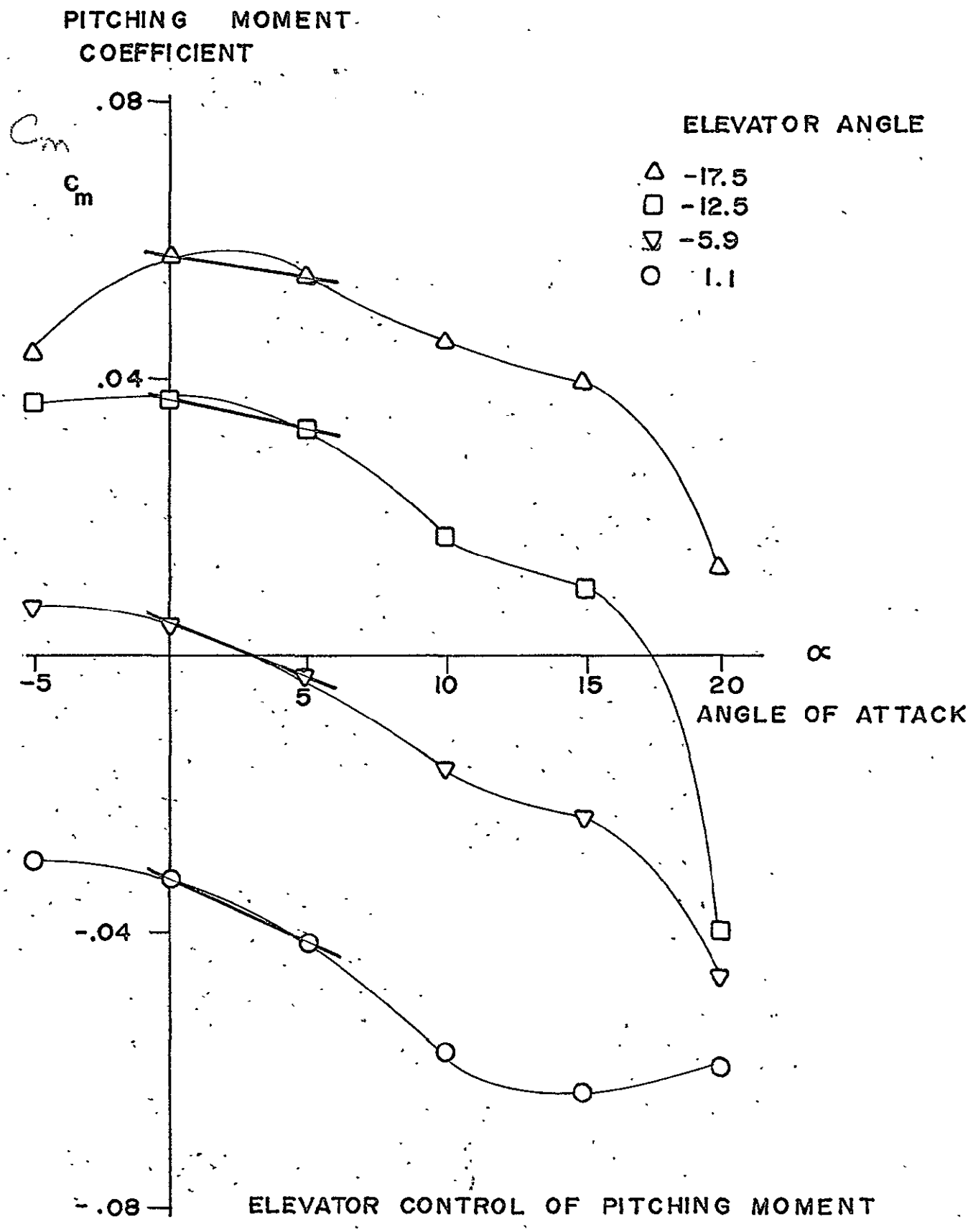

ELEVATOR CONTROL OF PITCHING MOMENT

FIGURE 2.13

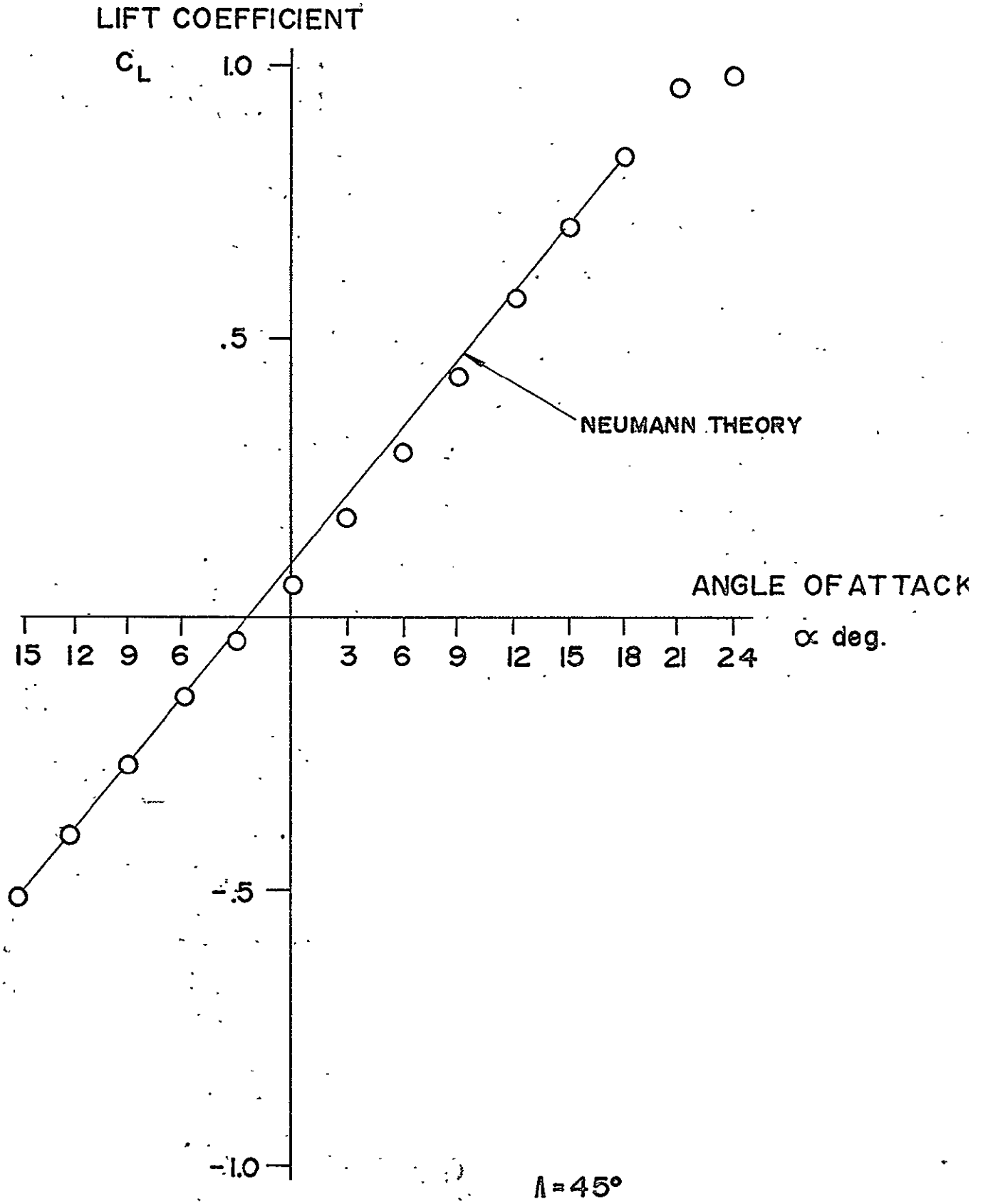

LIFT AS A FUNCTION OF ANGLE OF ATTACK
(NO ELEVATOR)

FIGURE 2.14

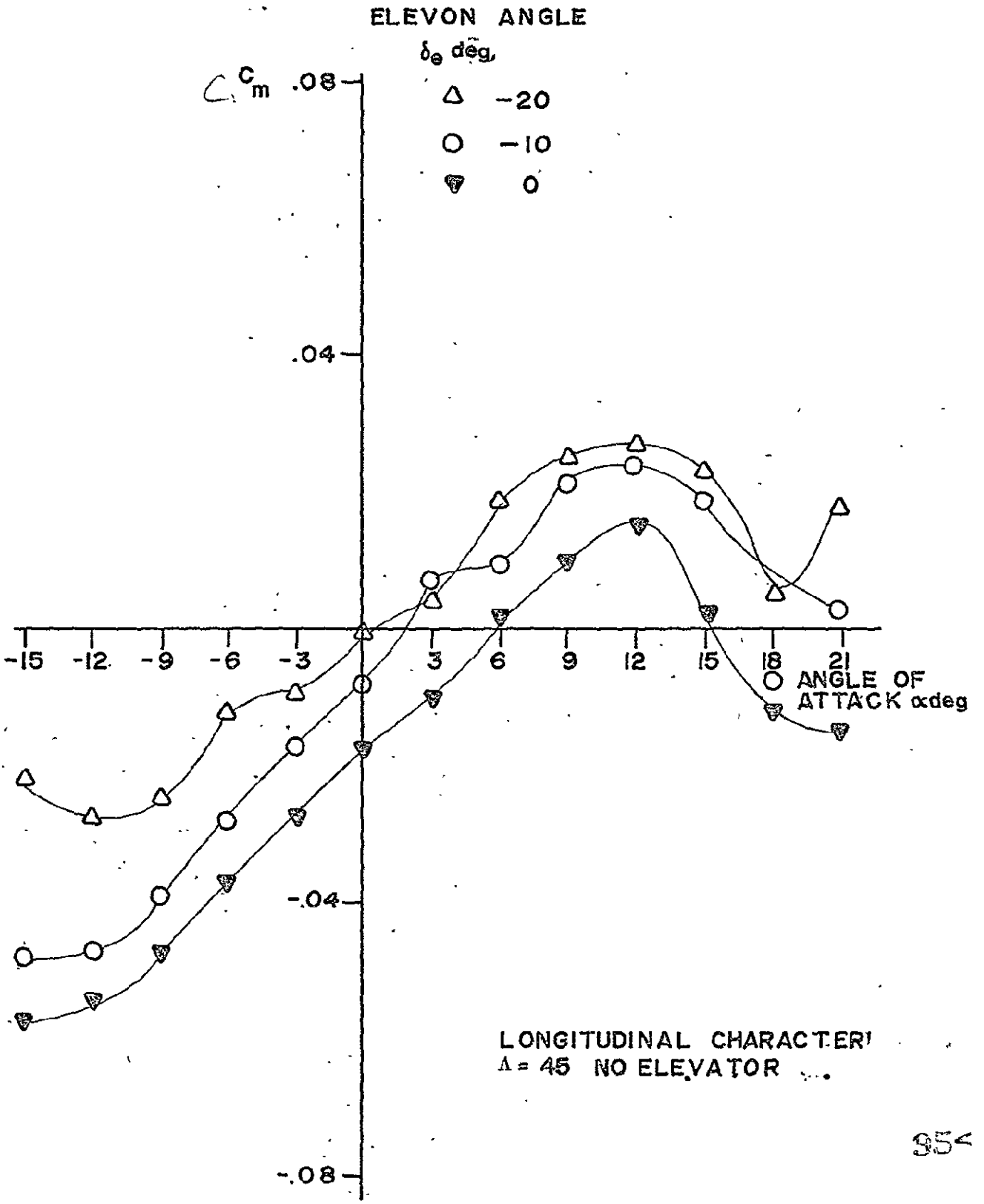

LONGITUDINAL CHARACTERI
Λ = 45 NO ELEVATOR

95

FIGURE 2.15

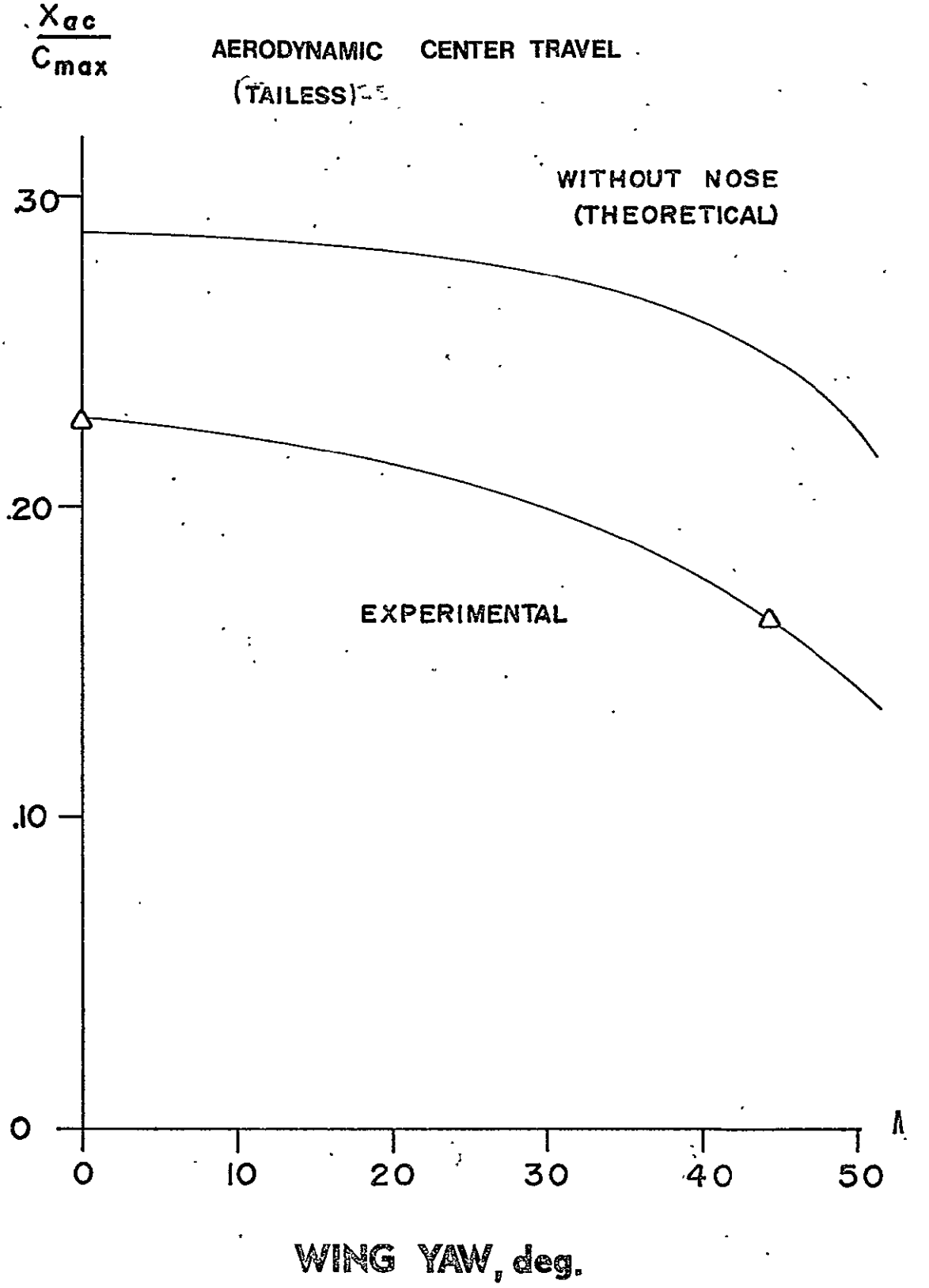
$\frac{X_{ac}}{C_{max}}$
AERODYNAMIC CENTER TRAVEL
(TAILESS)
WITHOUT NOSE
(THEORETICAL)
EXPERIMENTAL
.30
.20
.10
0
0
10
20
30
40
50
M
WING YAW, deg.

FIGURE 2.16

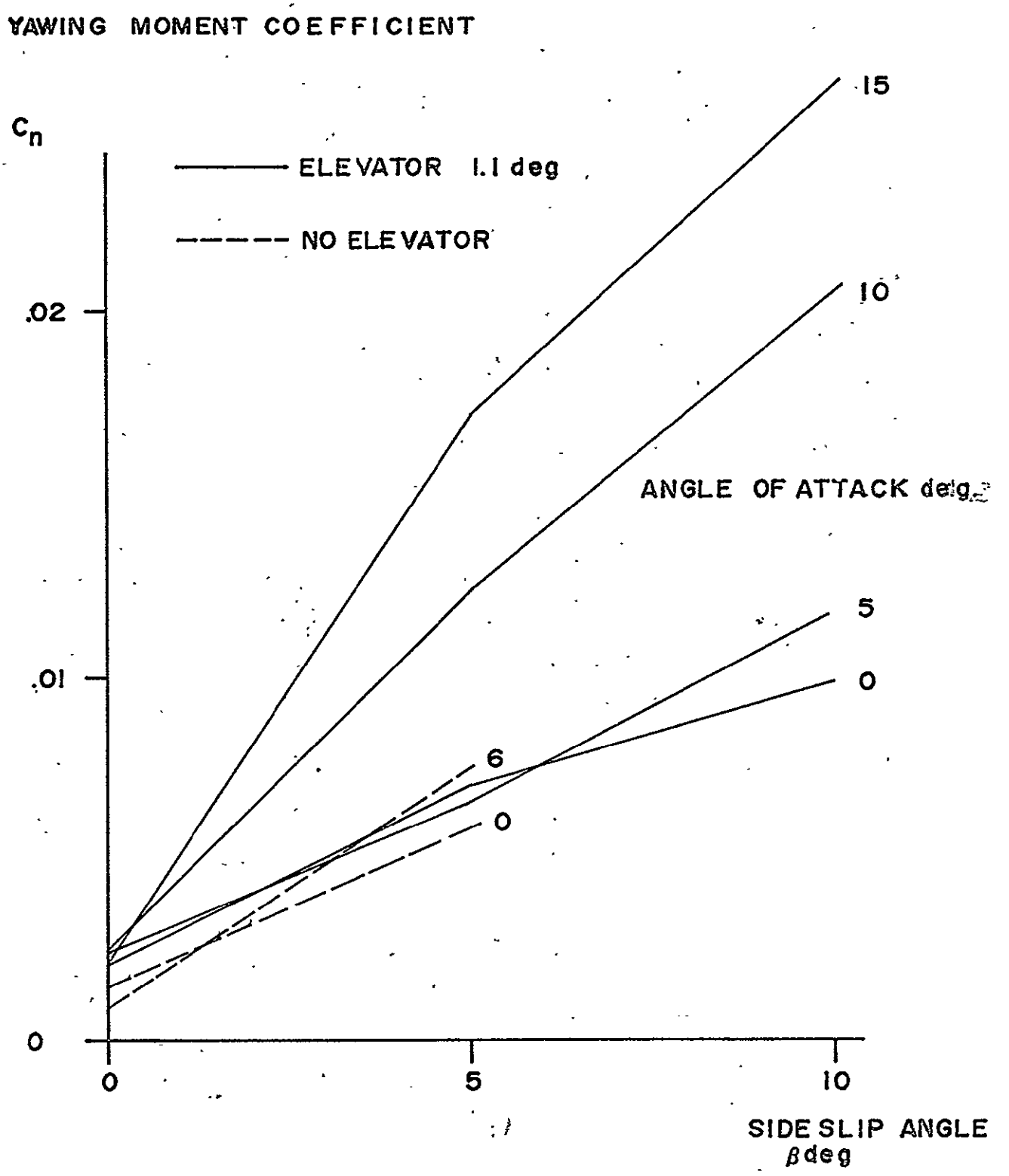

YAW RESTORING MOMENT

FIGURE 2.17

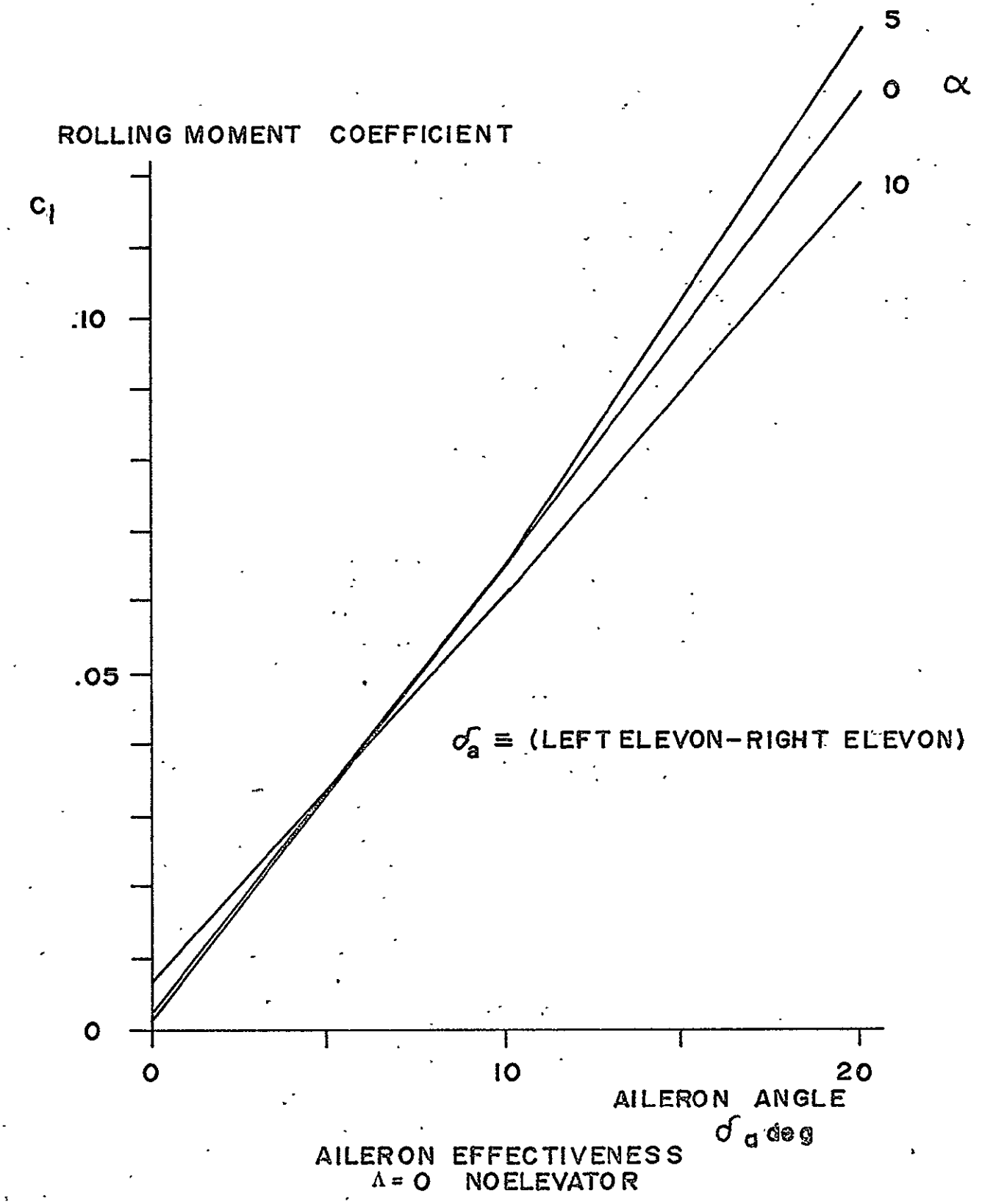
ROLLING MOMENT COEFFICIENT
C_l
.10
.05
0
0
10
20
AILERON ANGLE
δ_a deg
$\delta_a \equiv$ (LEFT ELEVON − RIGHT ELEVON)
5
0
10
α
AILERON EFFECTIVENESS
Λ = 0 NOELEVATOR

FIGURE 2.18

YAWING MOMENT COEFFICIENT

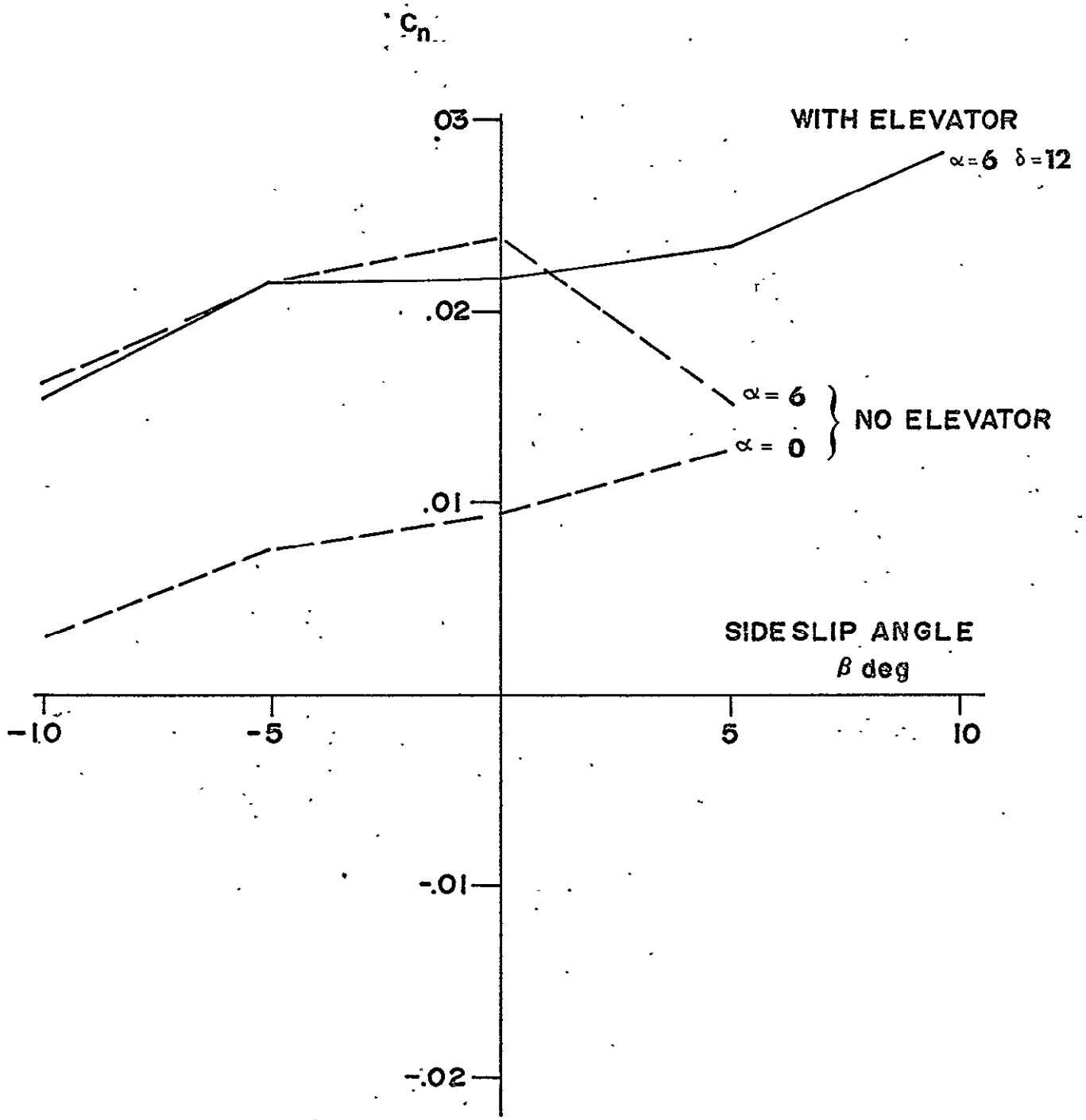

YAWING MOMENTS
Λ = 45 deg

FIGURE 2.19

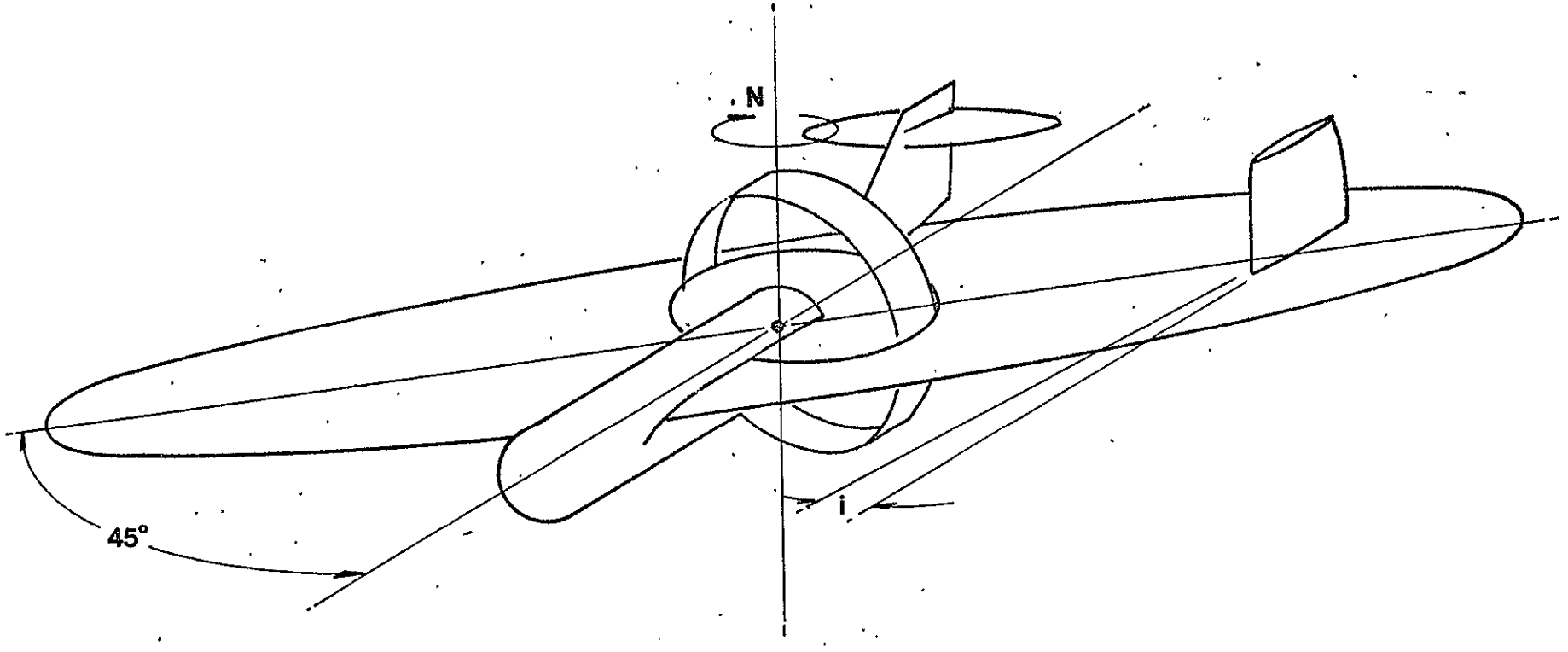

TIP STABILIZER

FIGURE 2-20

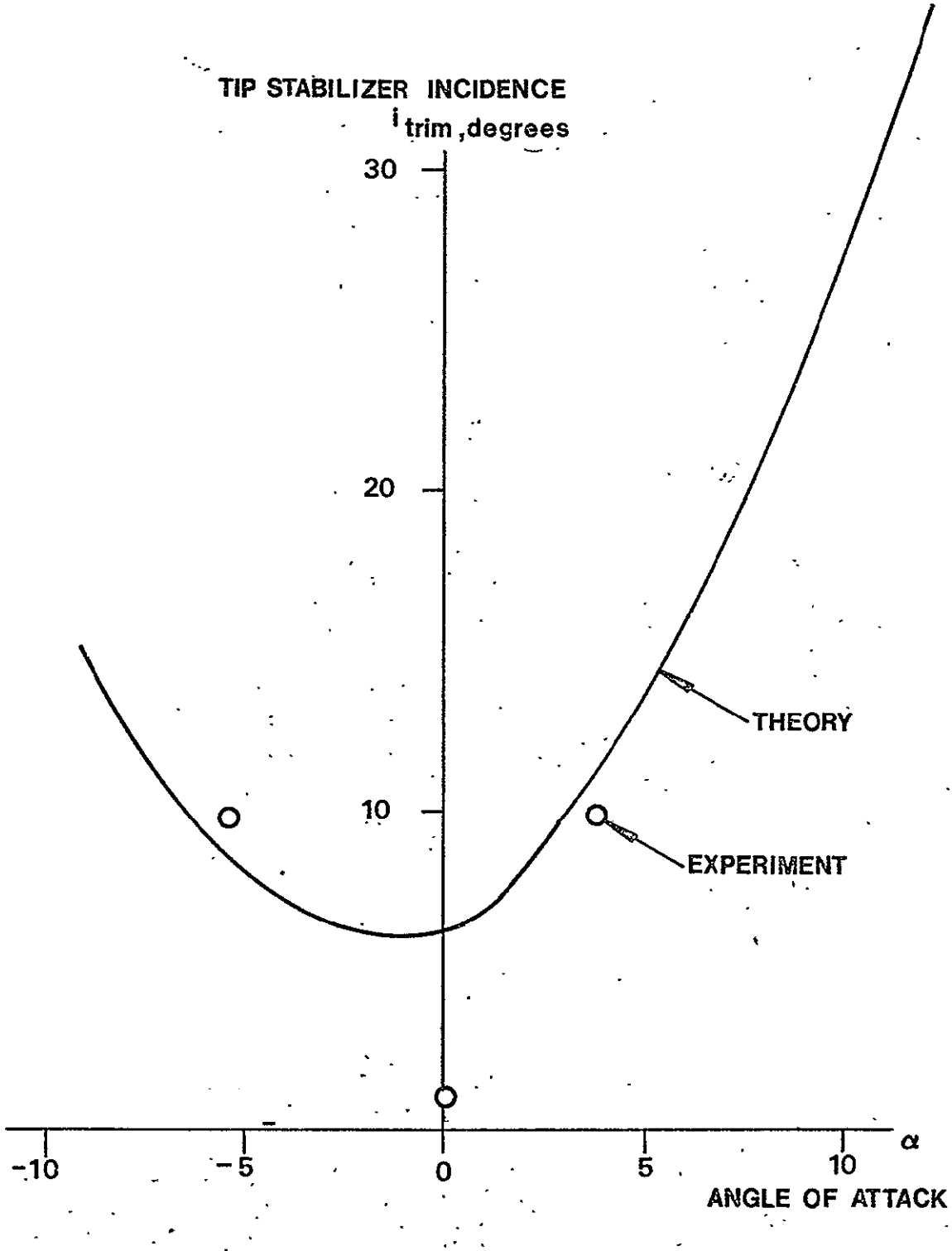

TIP STABILIZER INCIDENCE ANGLE REQUIRED TO TRIM
Λ=45° CRAFT @ ψ=0

FIGURE(2.21)

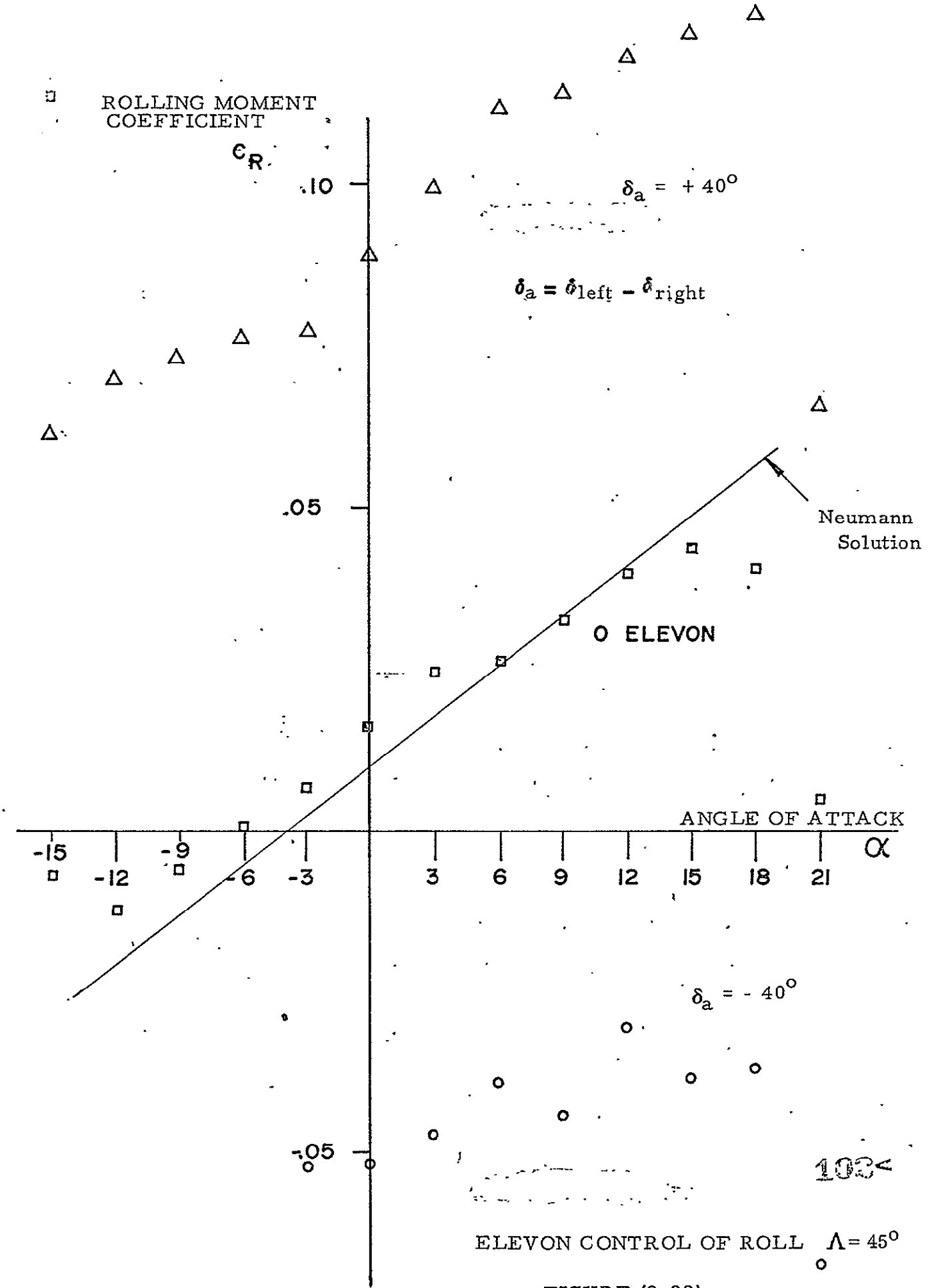

ELEVON CONTROL OF ROLL $\Lambda = 45^\circ$

FIGURE (2.22)

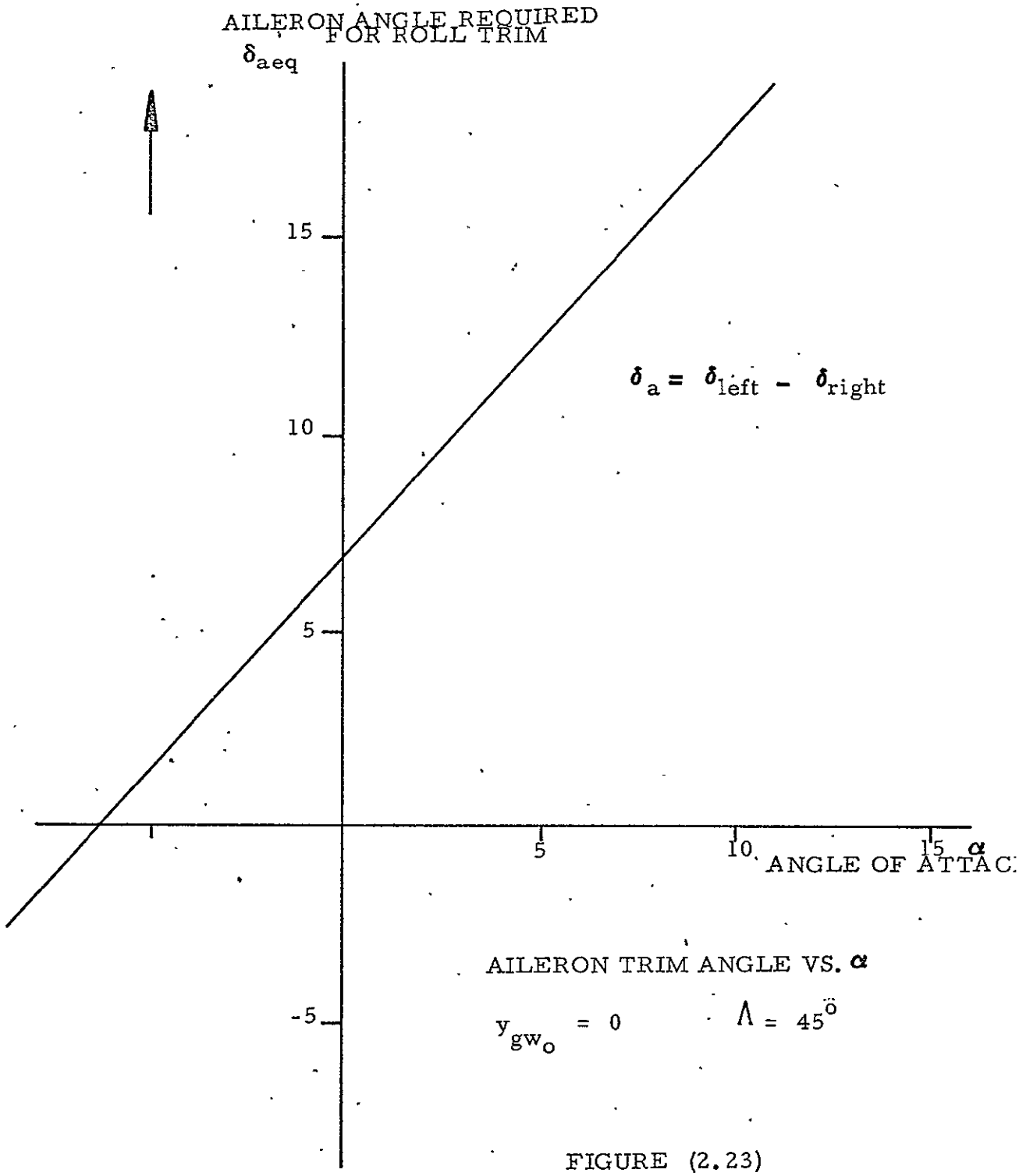

AILERON TRIM ANGLE VS. α

$y_{gw_o} = 0$ $\Lambda = 45^{\circ}$

FIGURE (2.23)

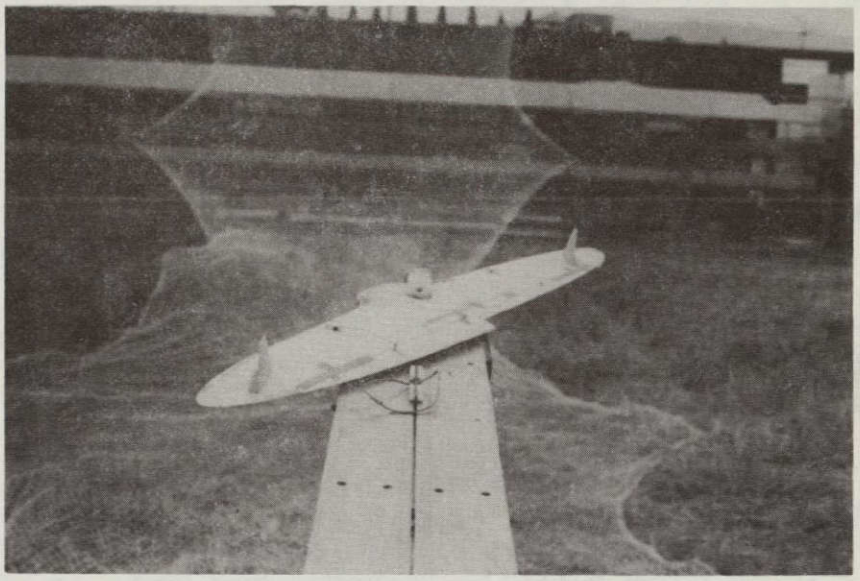

Unpowered Model Launch, $\Lambda = 50^{\circ}$

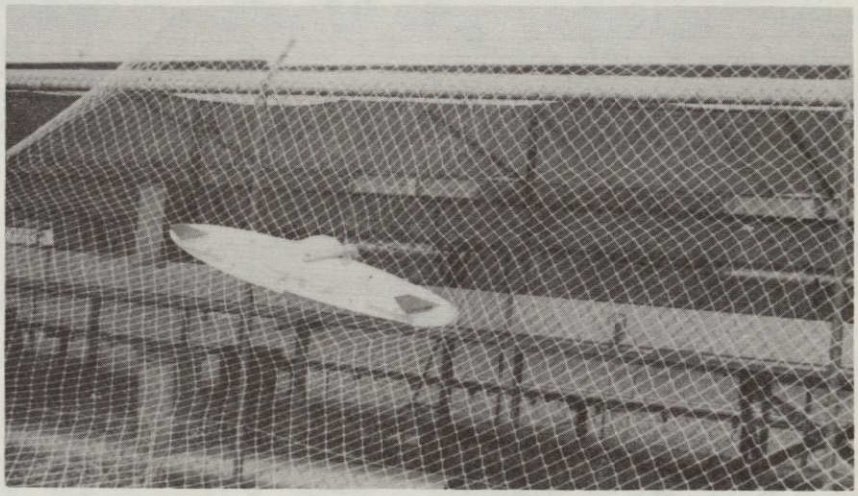

Unpowered Model Net Recovery, $\Lambda = 50^{\circ}$

FIGURE (2.24)

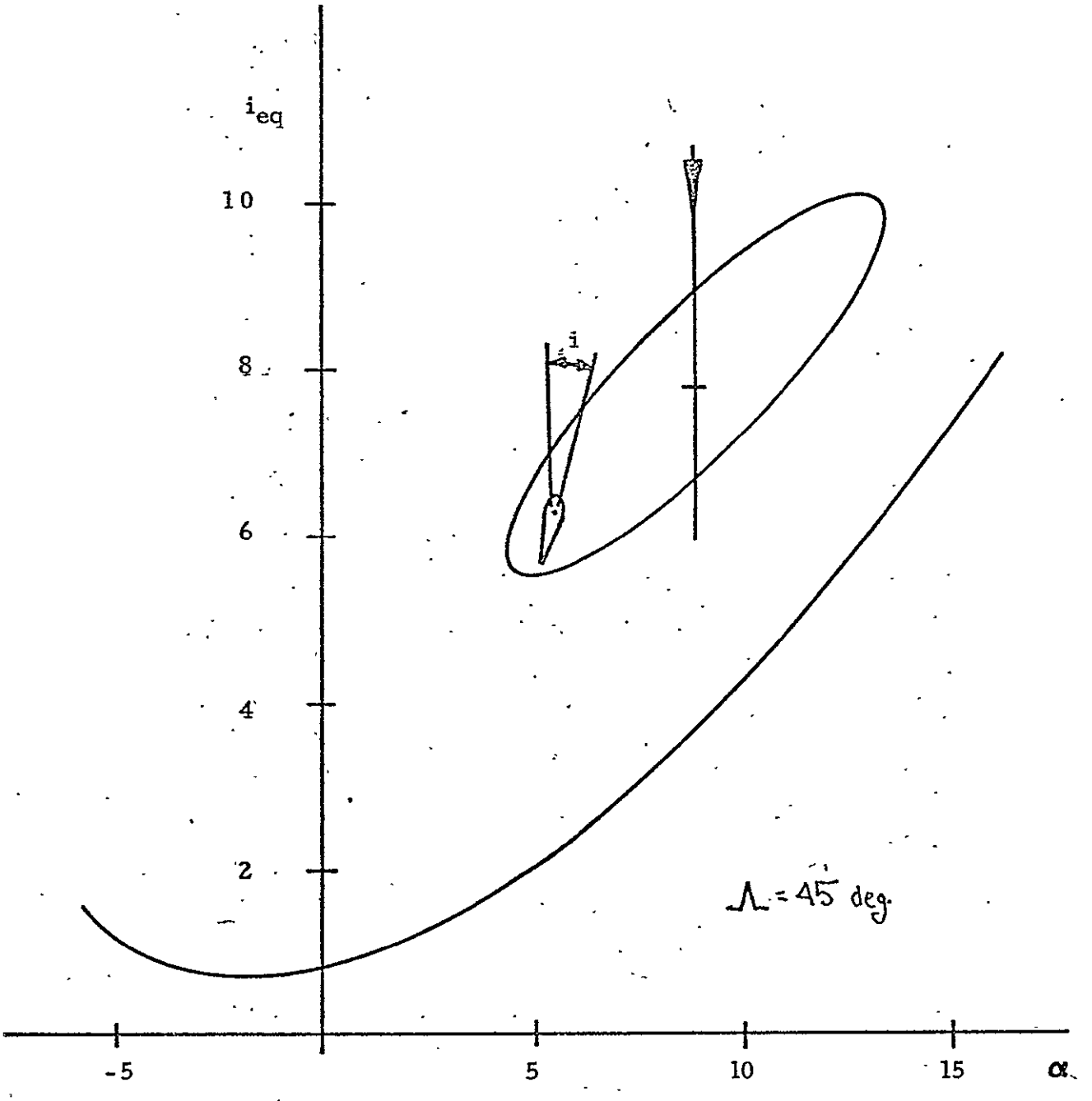

REDESIGNED TIP STABILIZER

EQUILIBRIUM INCIDENCE ANGLE (THEORY)

FIGURE (2.25)

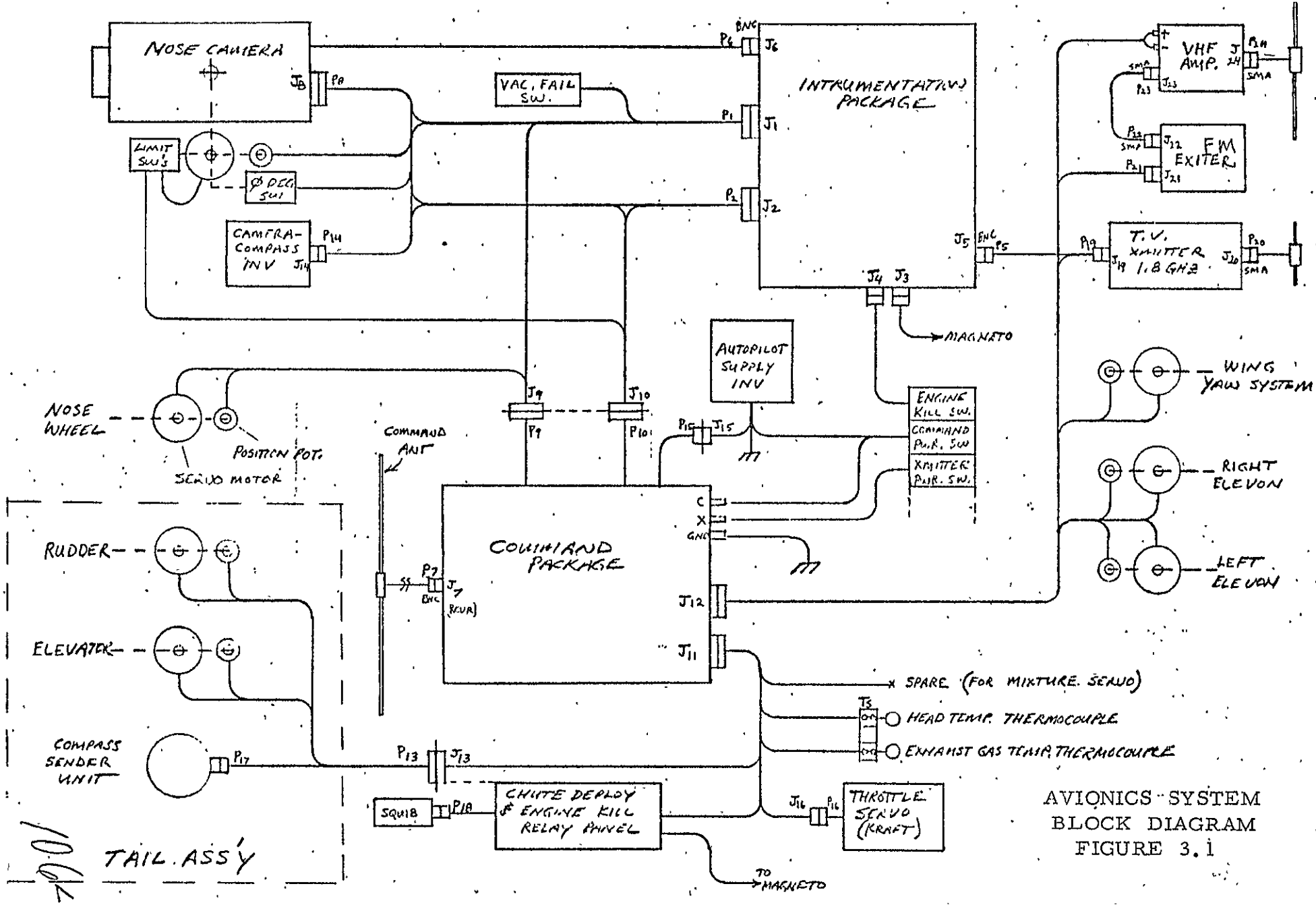

AVIONICS SYSTEM
BLOCK DIAGRAM
FIGURE 3.1

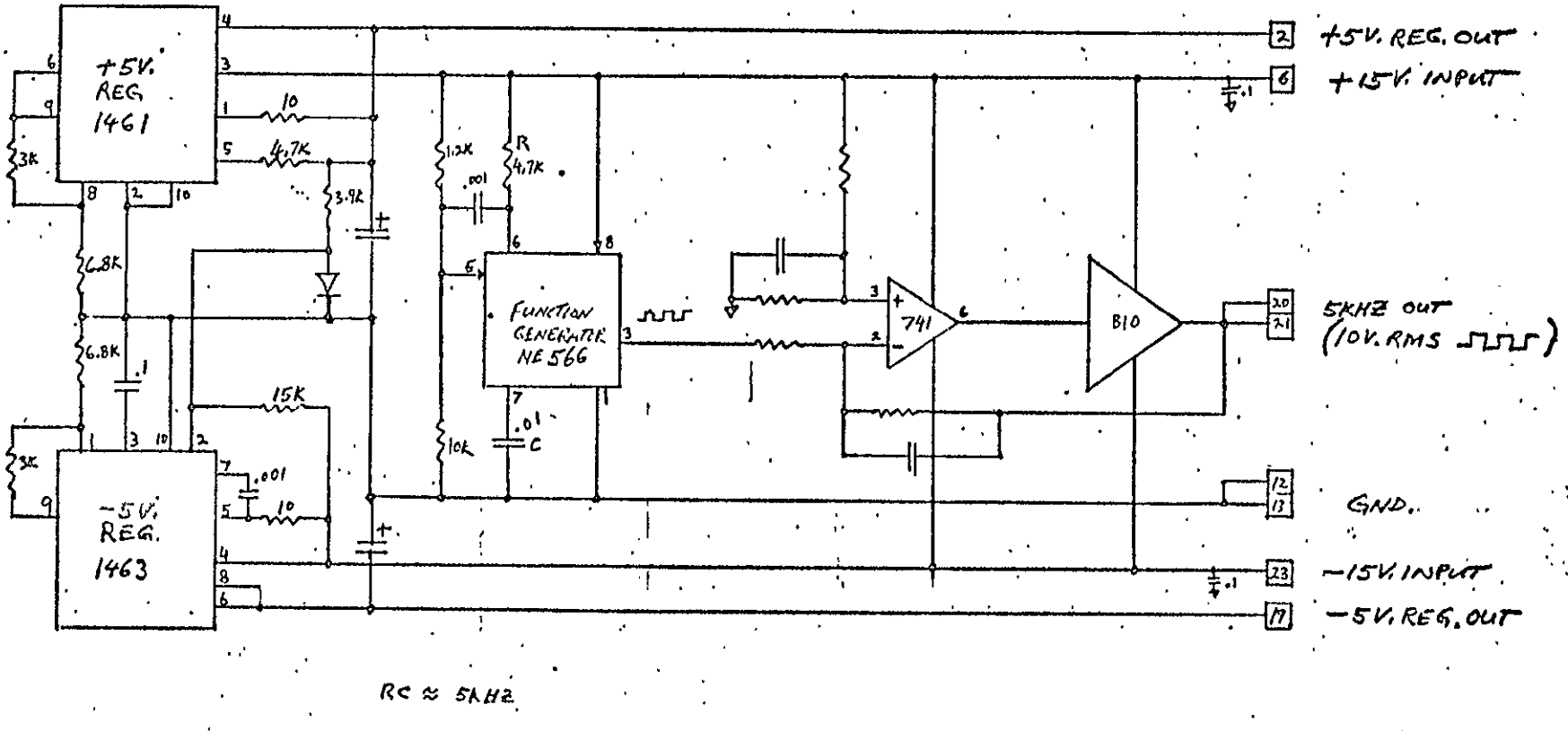

AUTOPILOT SUPPLY CARD (#1)

FIGURE 3.2

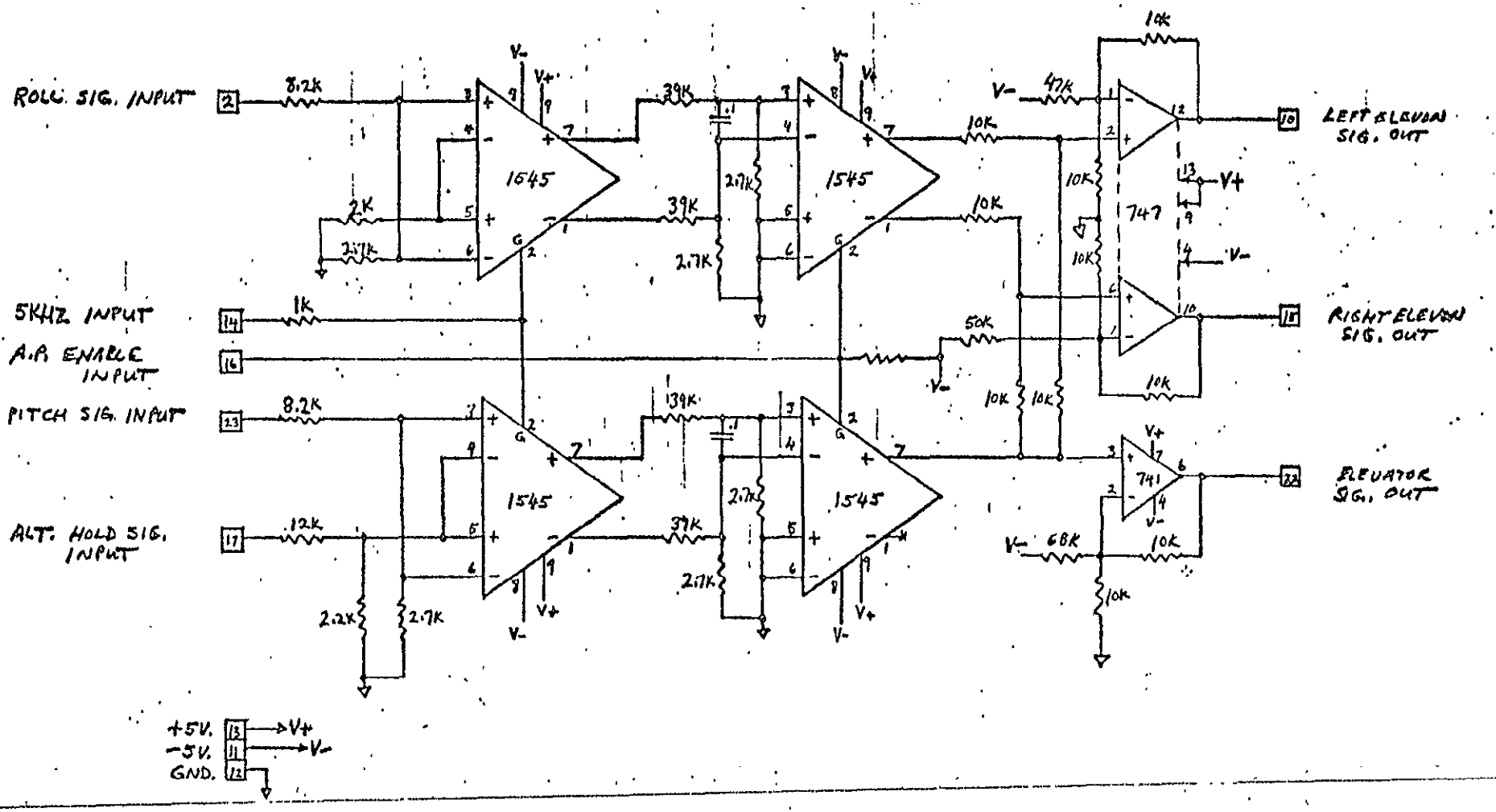

GYRO INTERFACE CARD (#2)

FIGURE 3.3

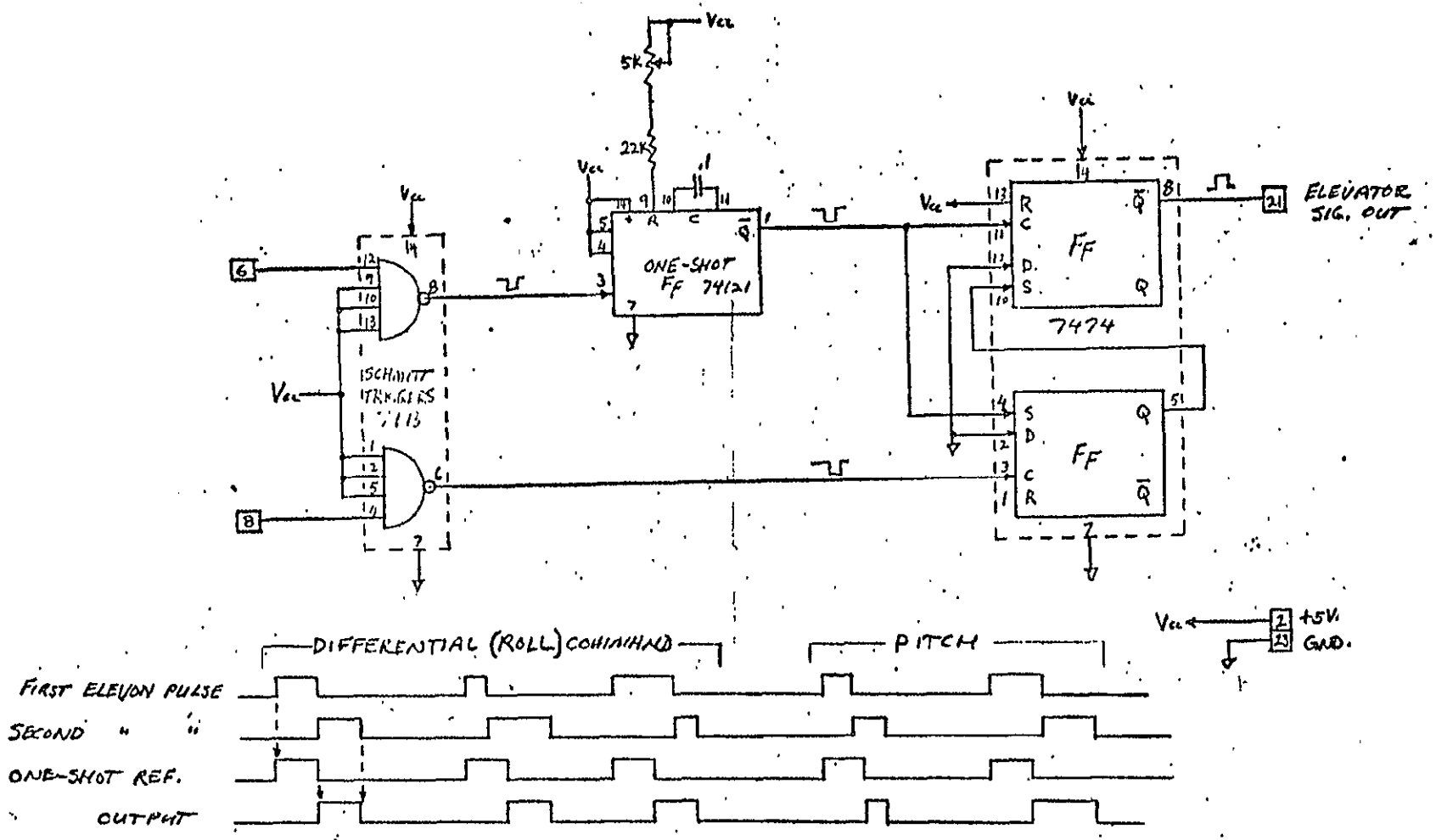

ELEVATOR SIGNAL SYNTHESIZER CARD

FIGURE 3.4

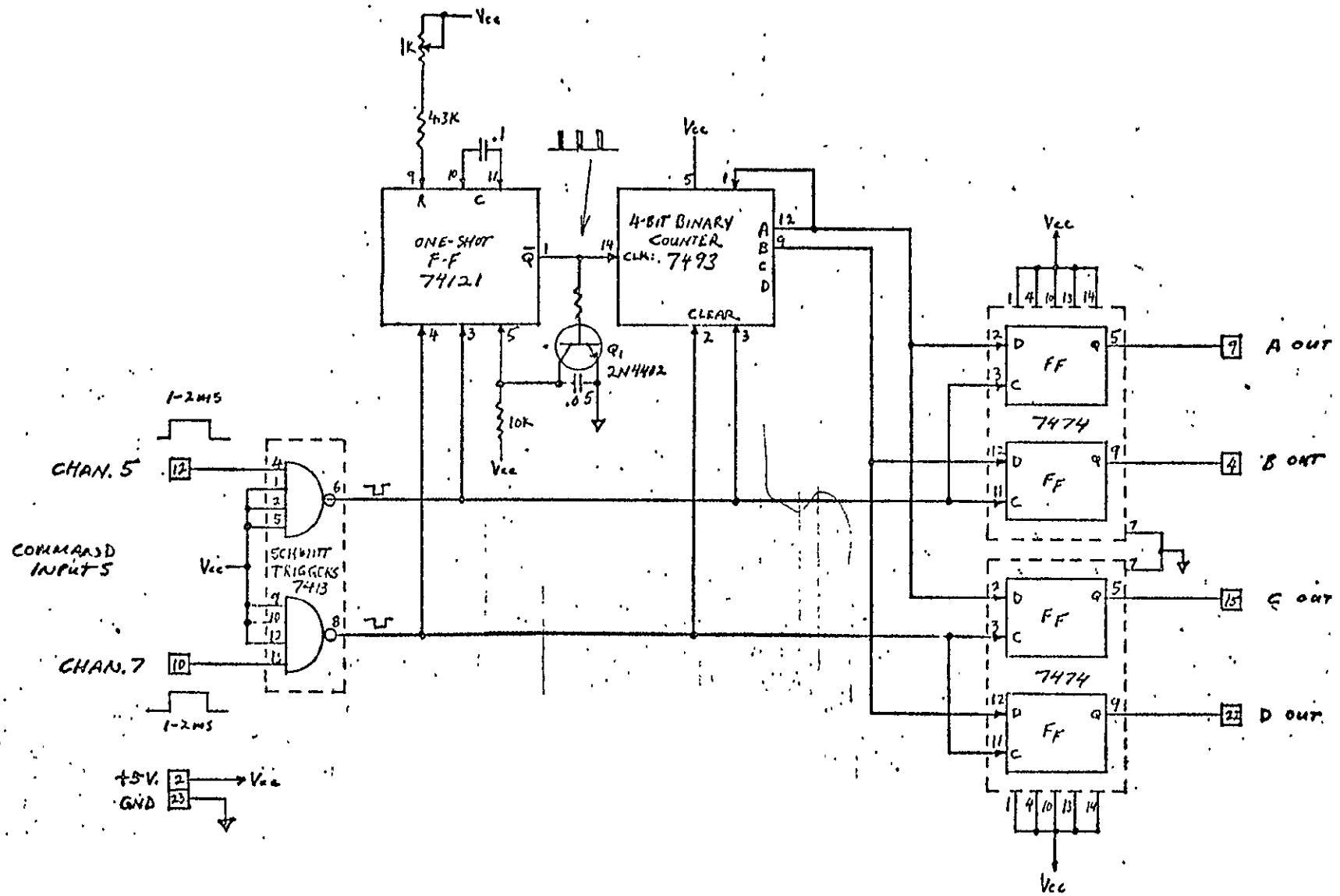

AUXILIARY SELECT CARD (#6)

FIGURE 3.5

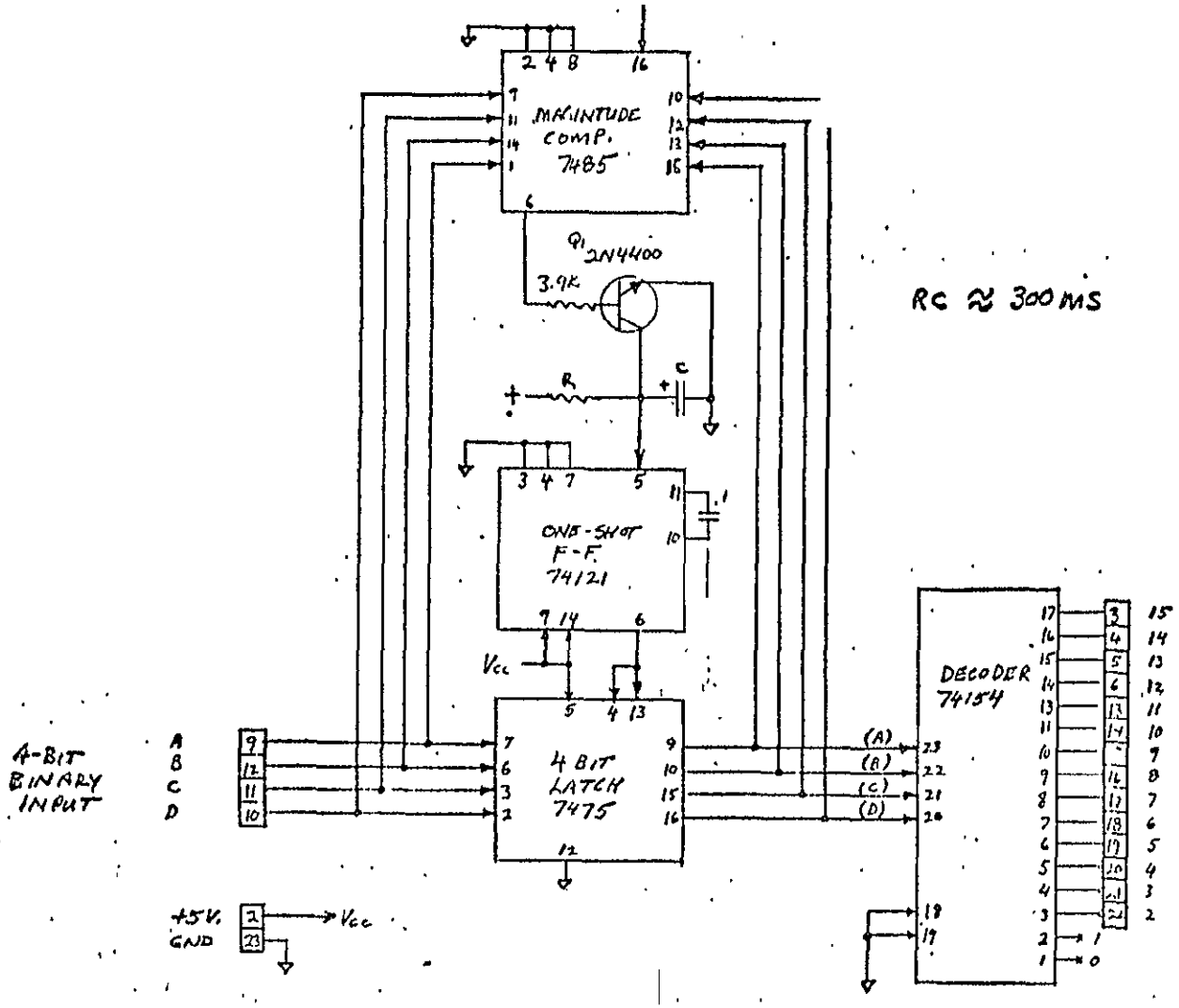

AUXILIARY DELAY/DECODE CARD (#7)

FIGURE 3.6

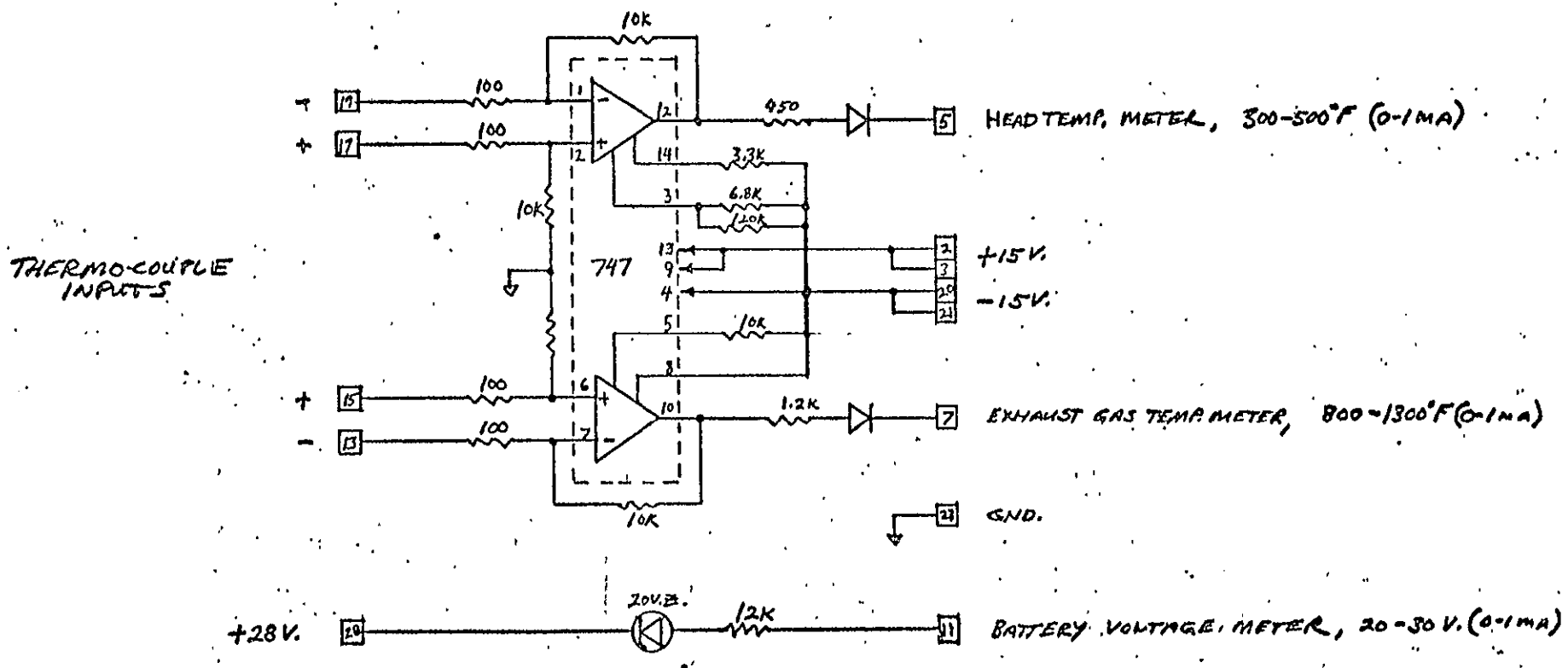

METER CARD (# 8)

FIGURE 3.7

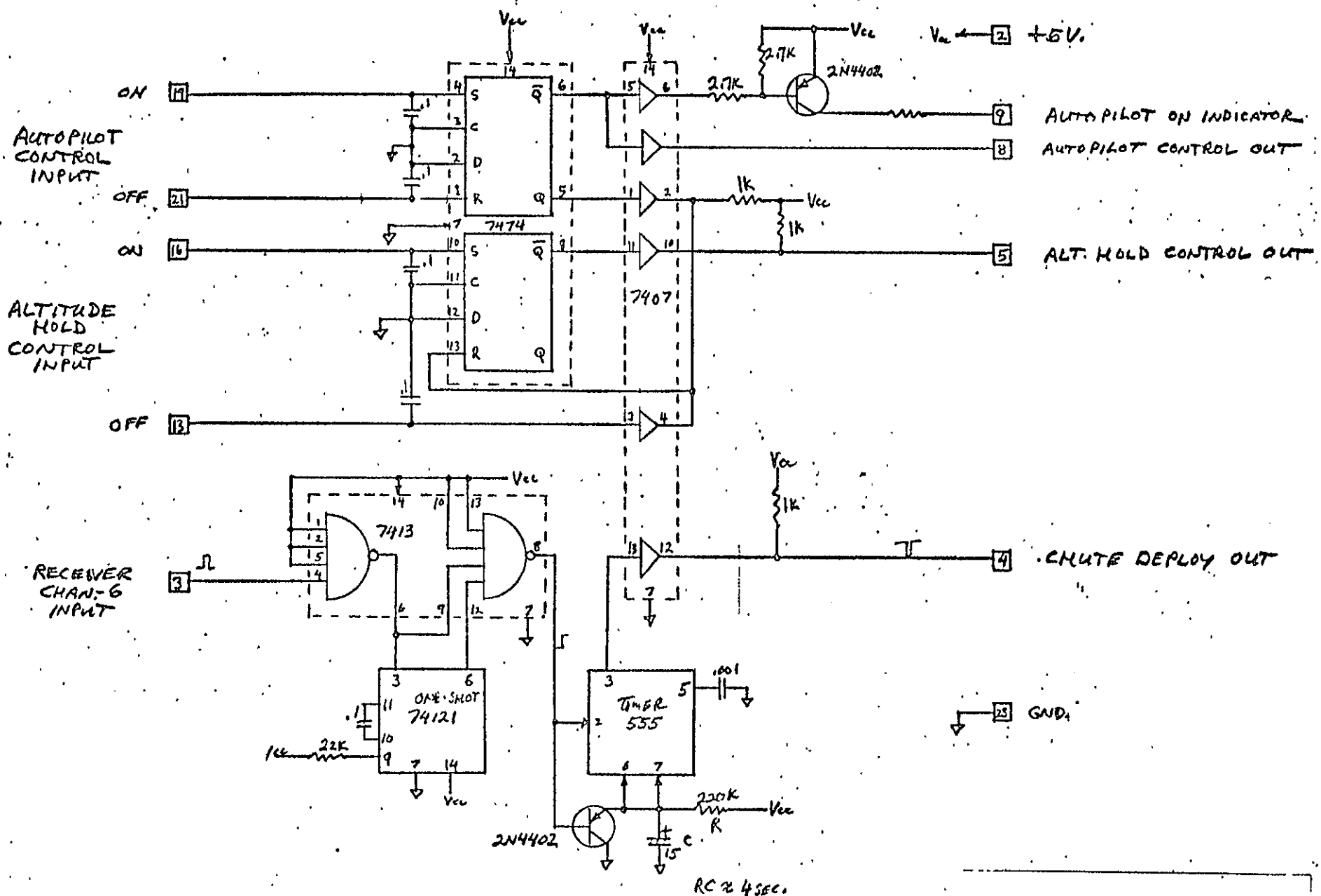

PRIORITY CONTROL CARD

FIGURE 3.8

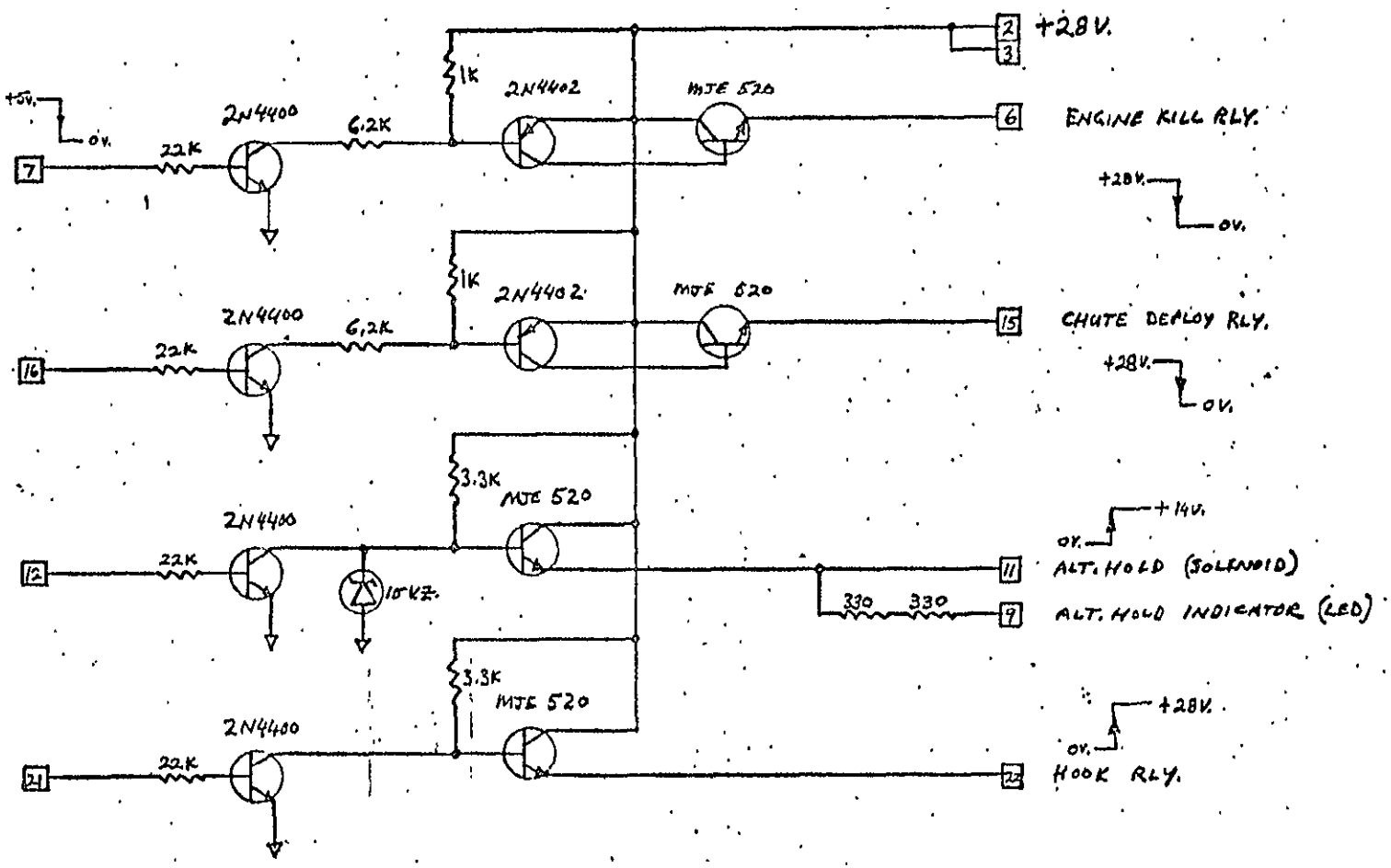

PRIORITY DRIVE CARD (#10)

FIGURE 3.9

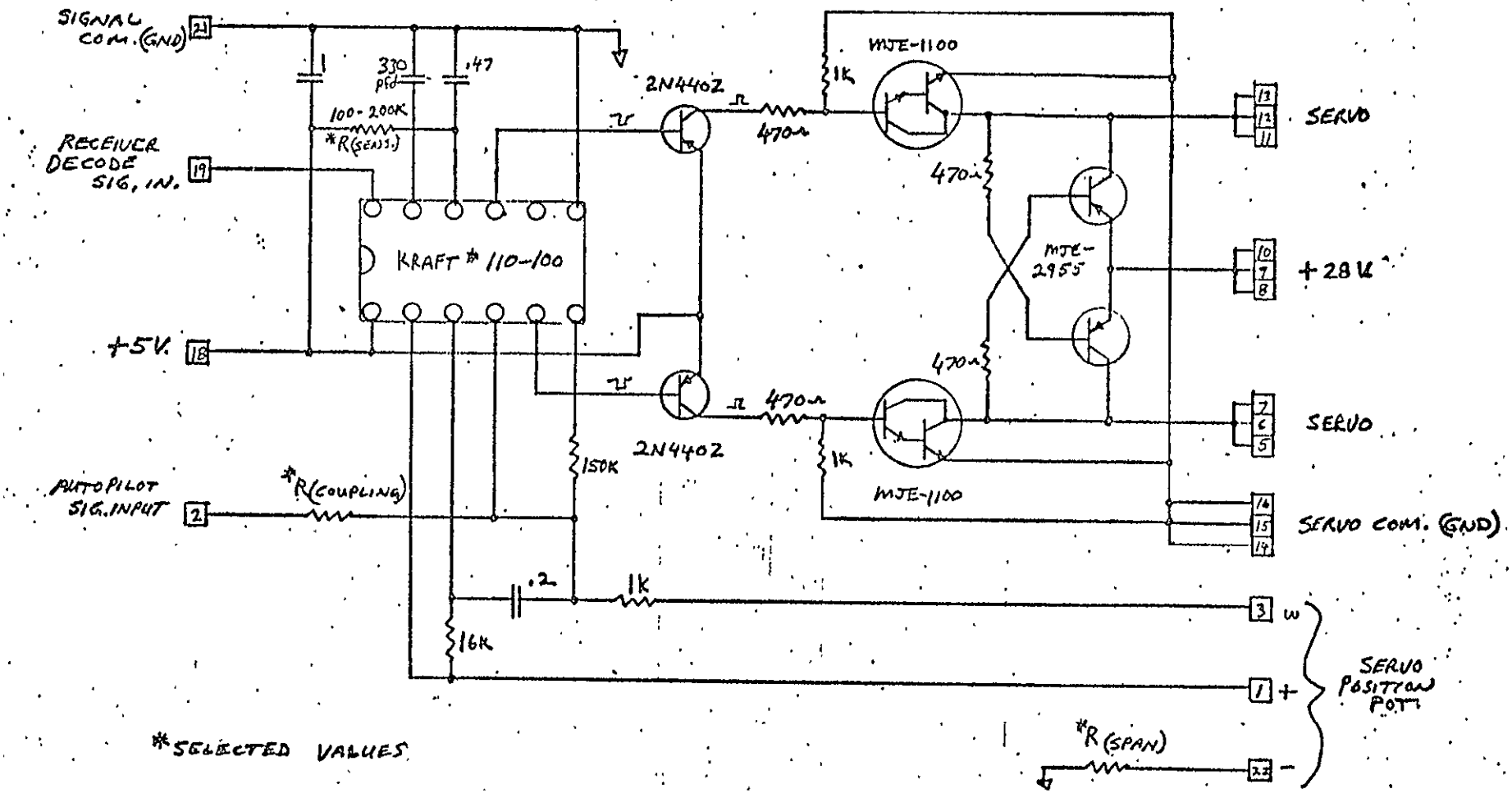

PROPORTIONAL SERVO AMPLIFIER CARD

FIGURE 3.10

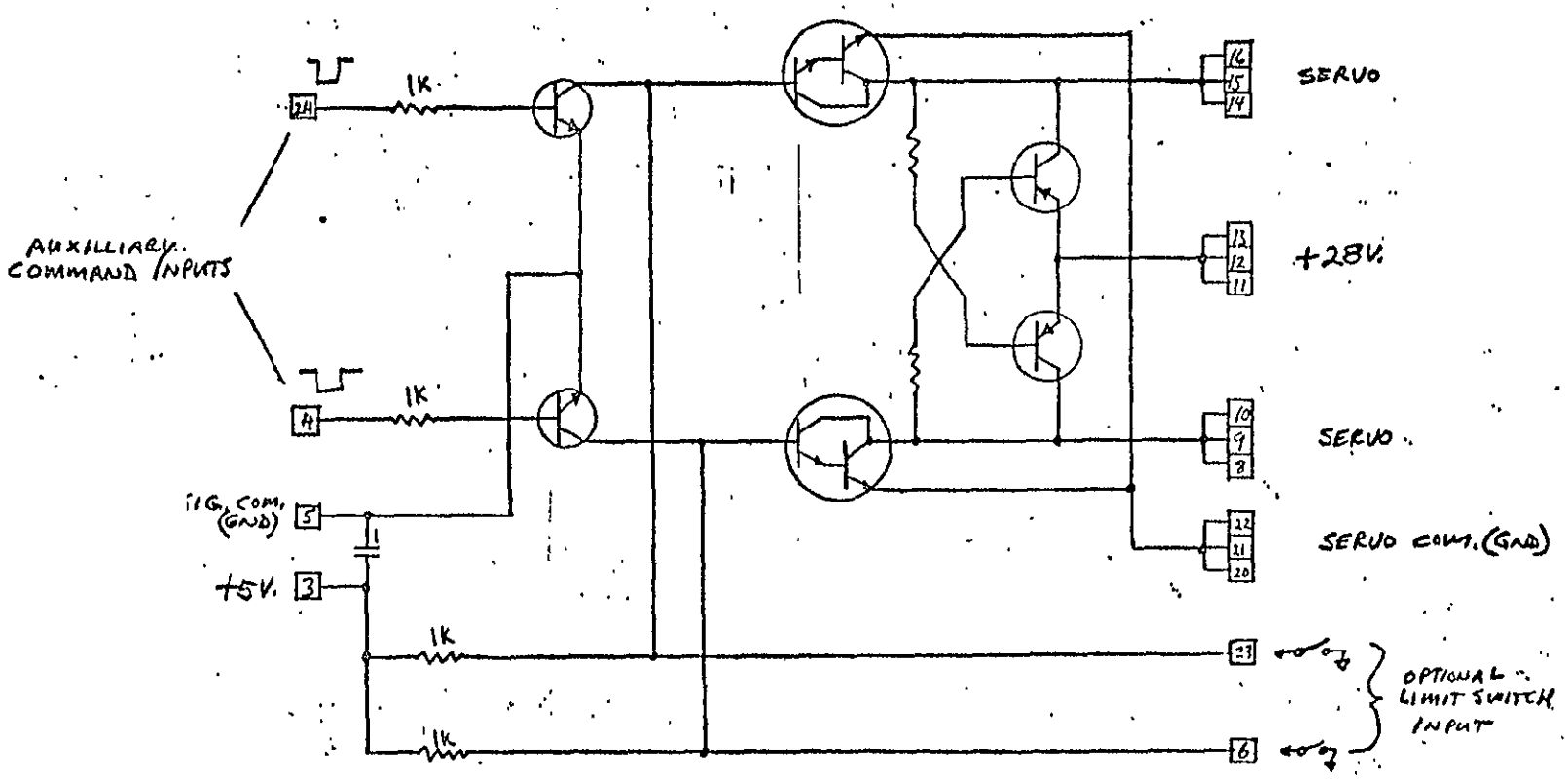

POSITIONABLE SERVO AMPLIFIER CARD

FIGURE 3.11

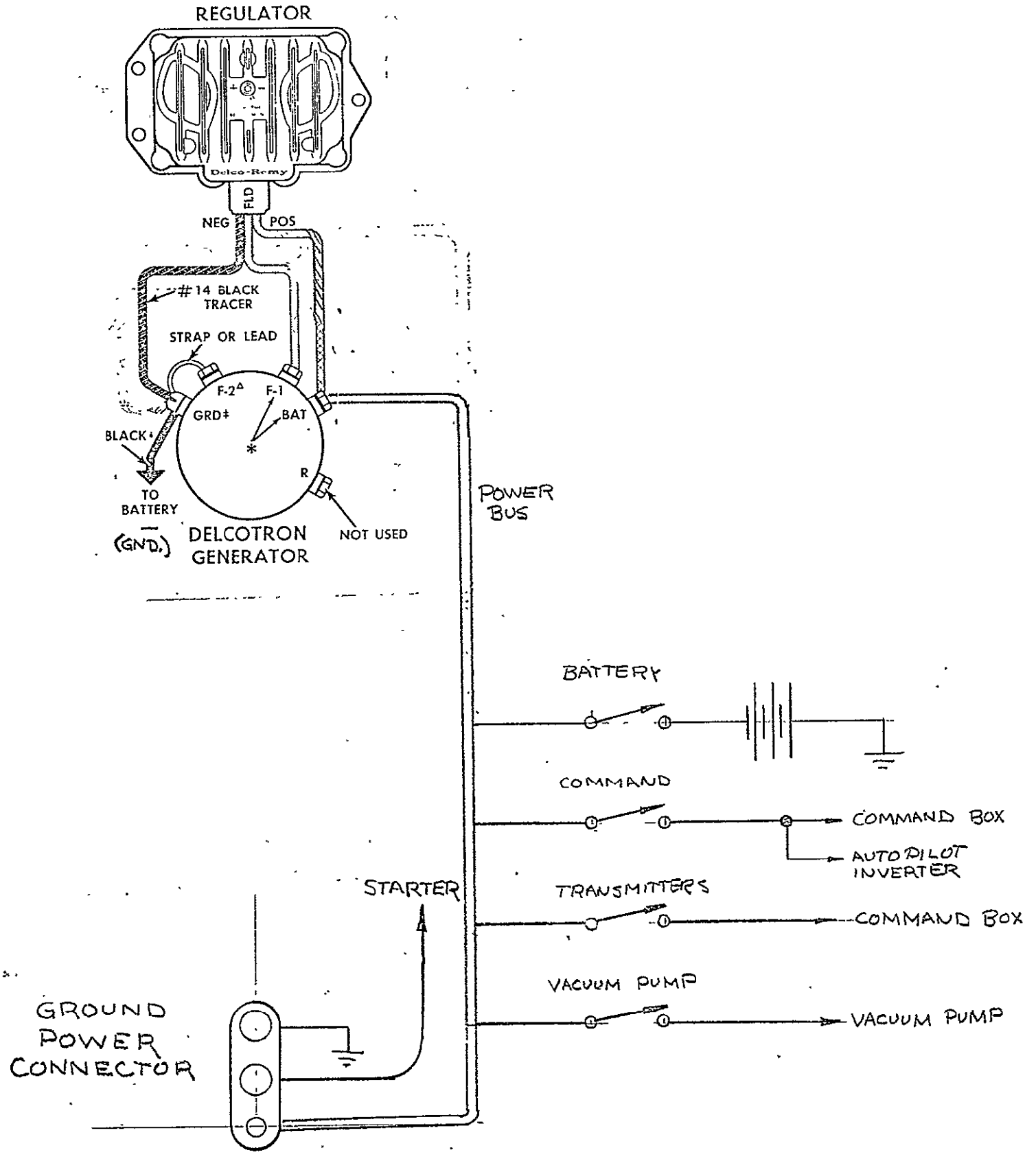

ELECTRICAL SCHEMATIC

FIGURE 3.12

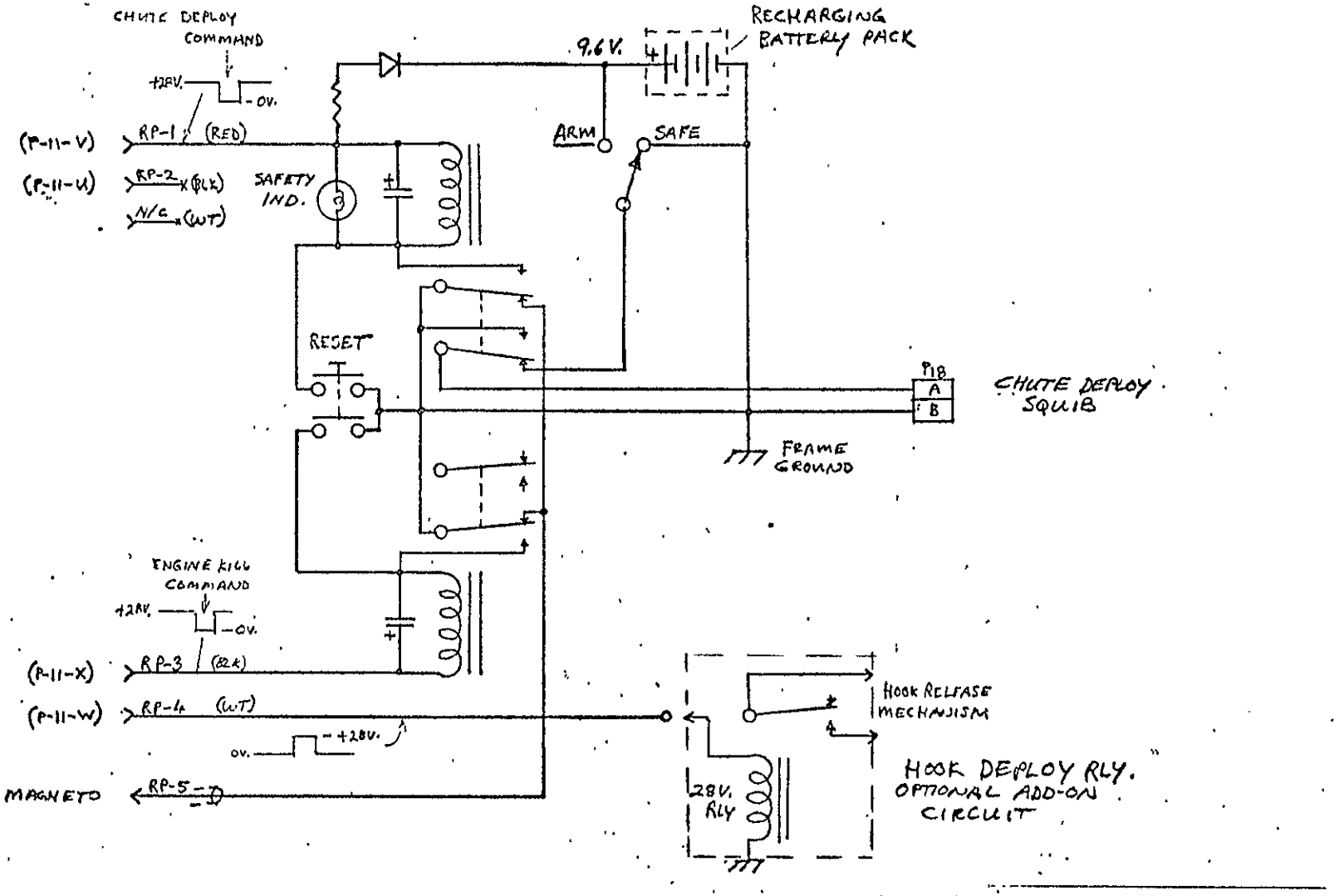

RELAY PANEL
FIGURE 3.13

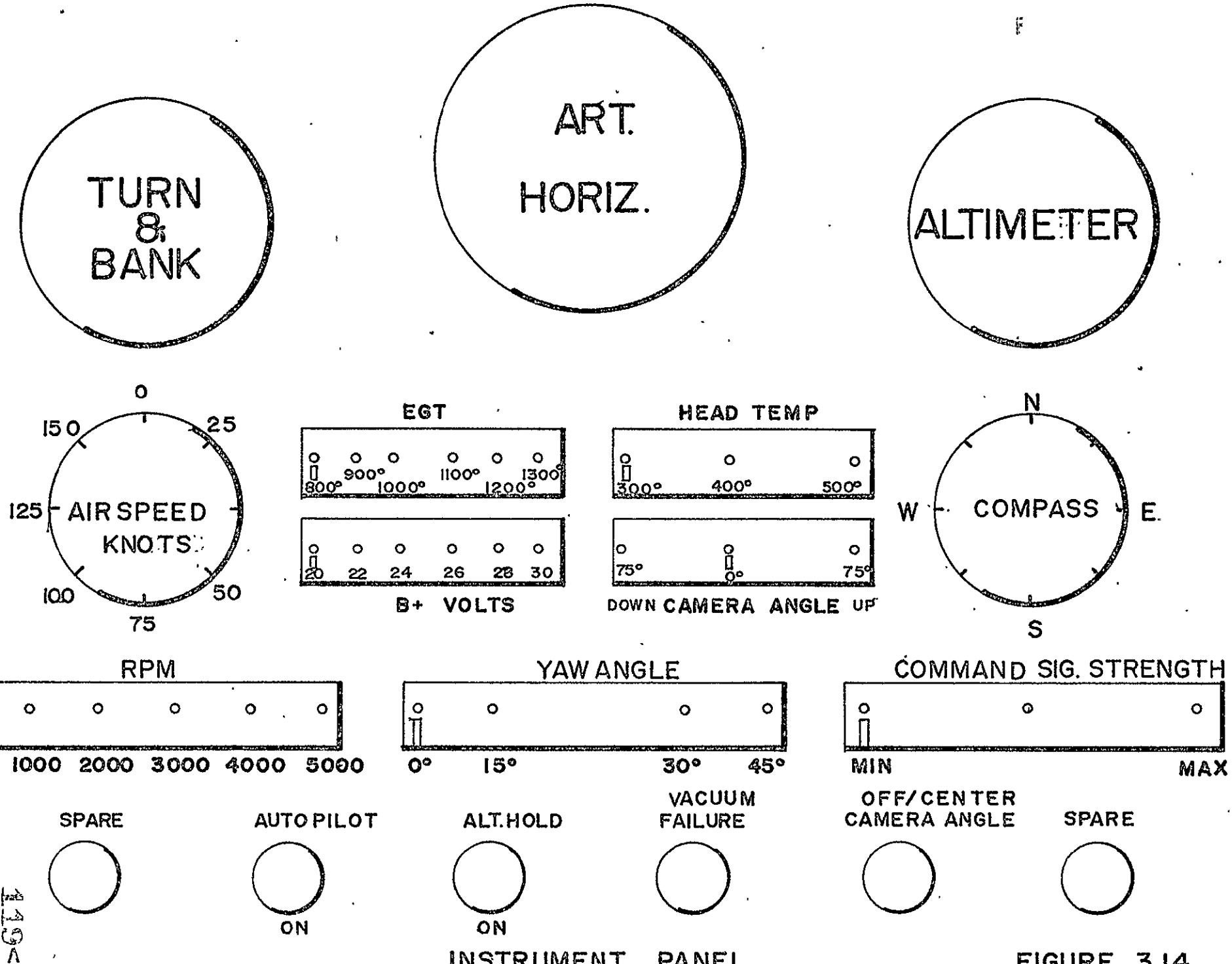

INSTRUMENT PANEL

FIGURE 3.14

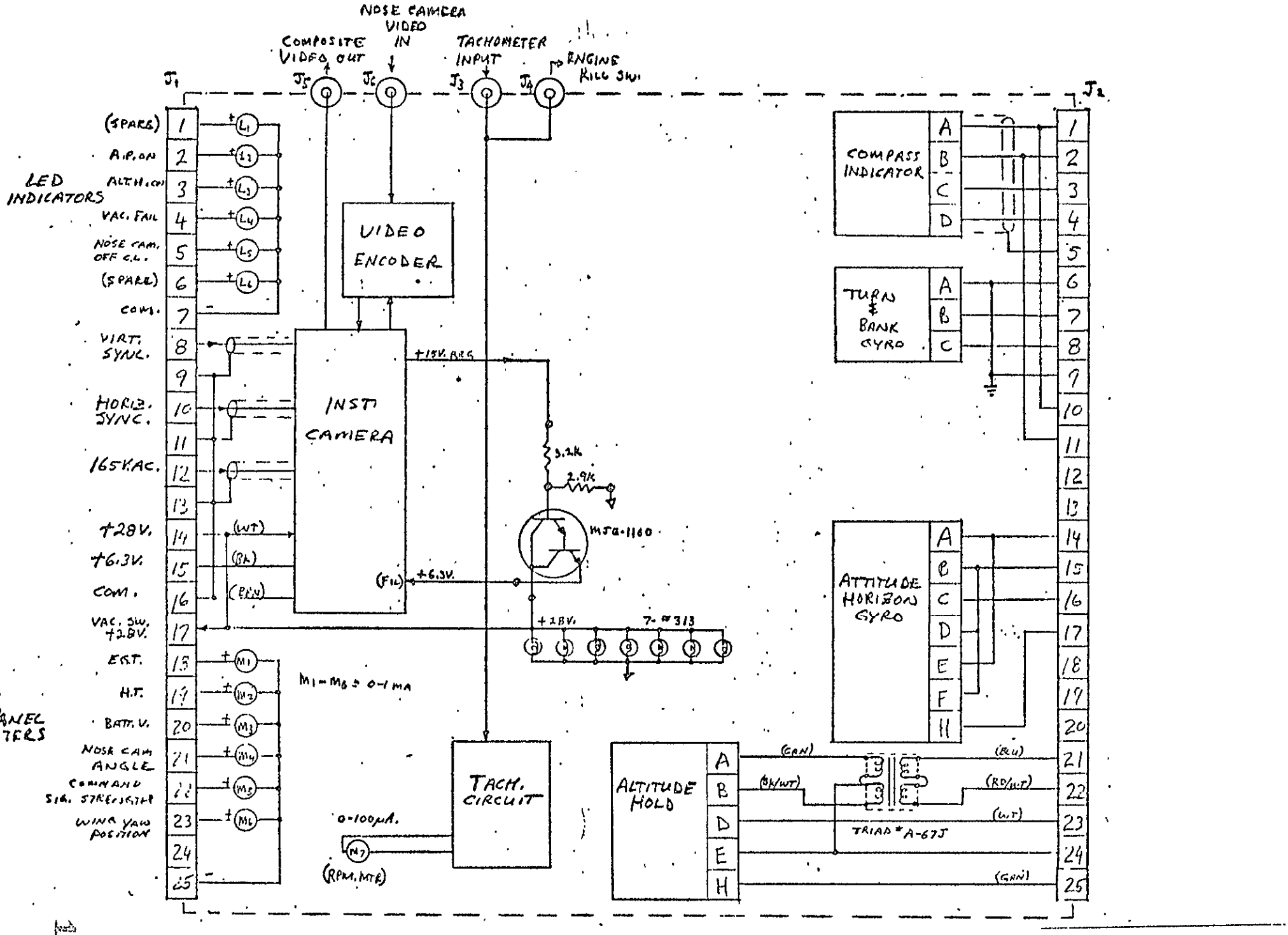

INSTRUMENT PACKAGE
FIGURE 3.15

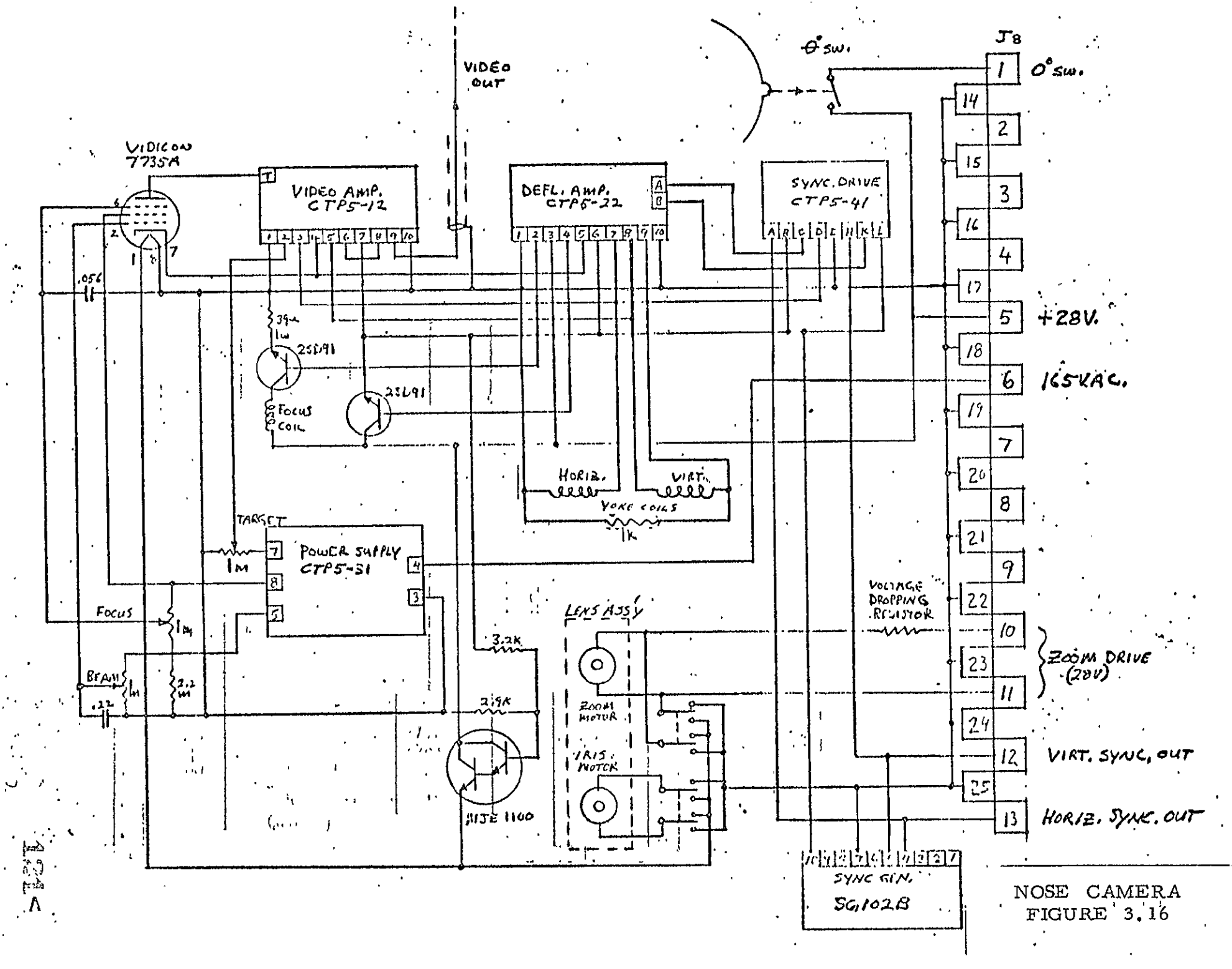

NOSE CAMERA
FIGURE 3.16

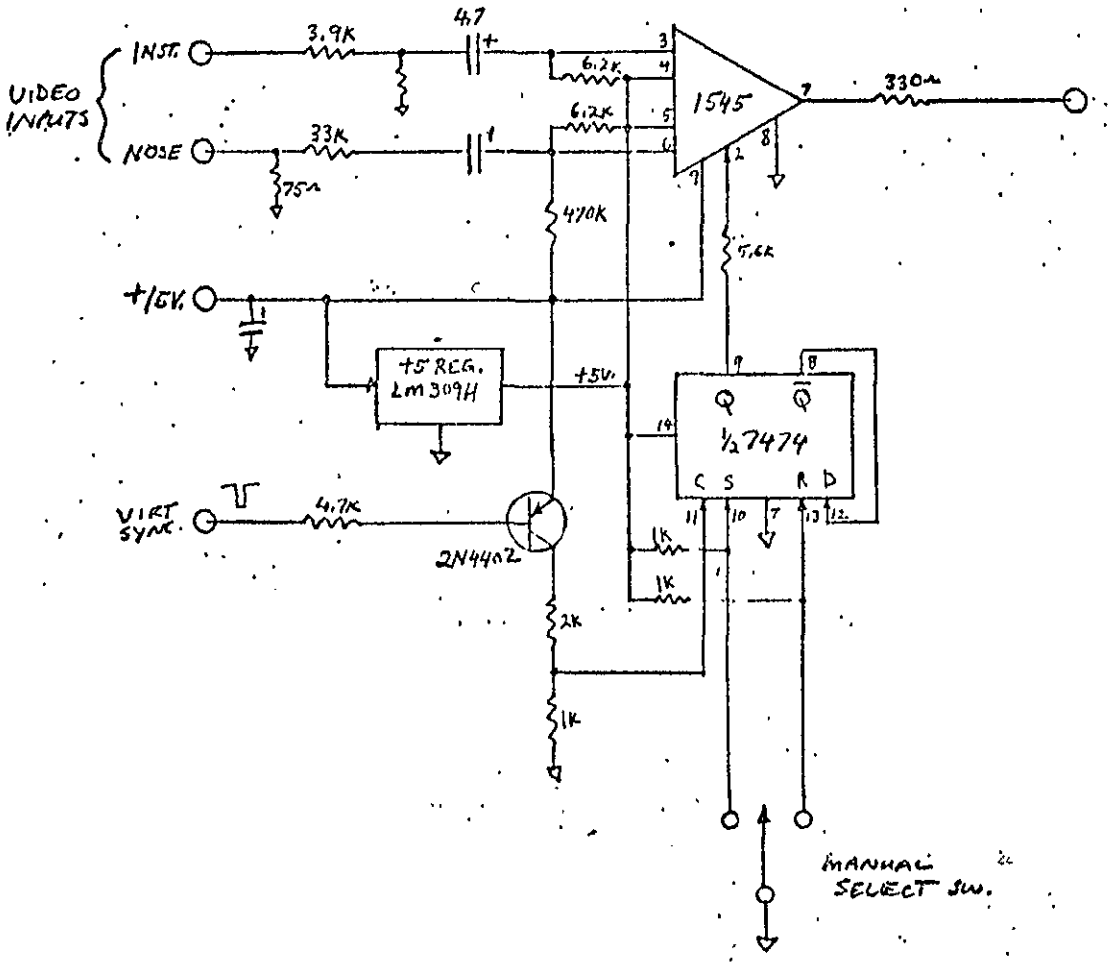

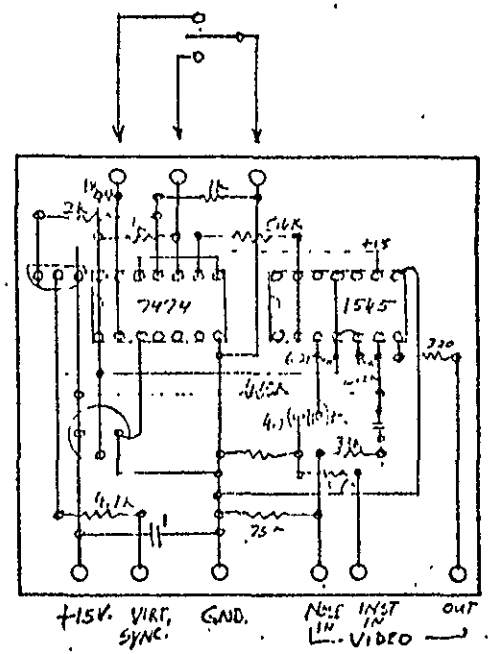

VIDEO ENCODER
(INST. PKG.)
FIGURE 3.17

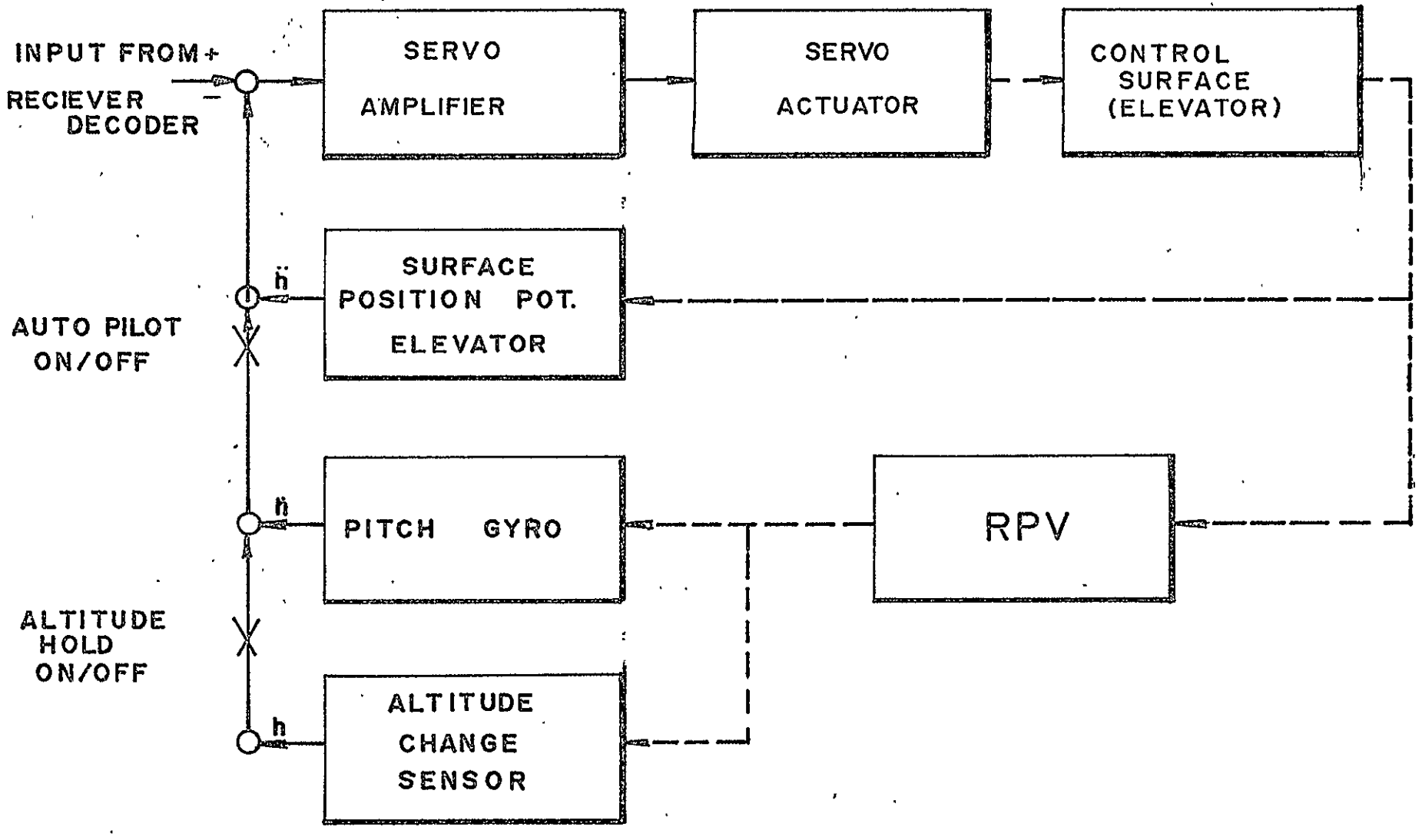

RPV CONTROL DIAGRAM (PITCH)

FIGURE 3.18

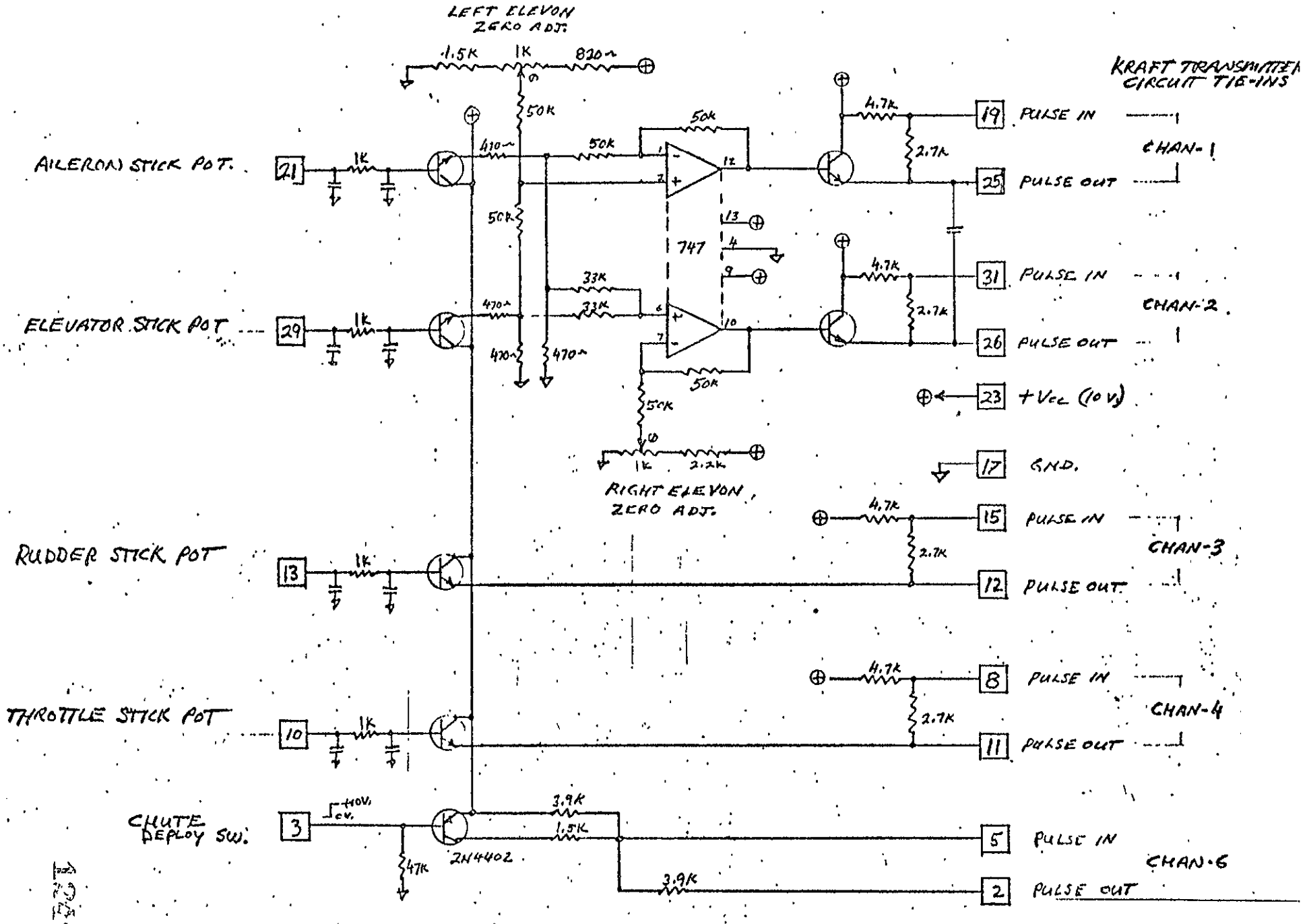

FLIGHT CONTROL CIRCUIT
(CONTROL CIRCUIT)
FIGURE 3.19

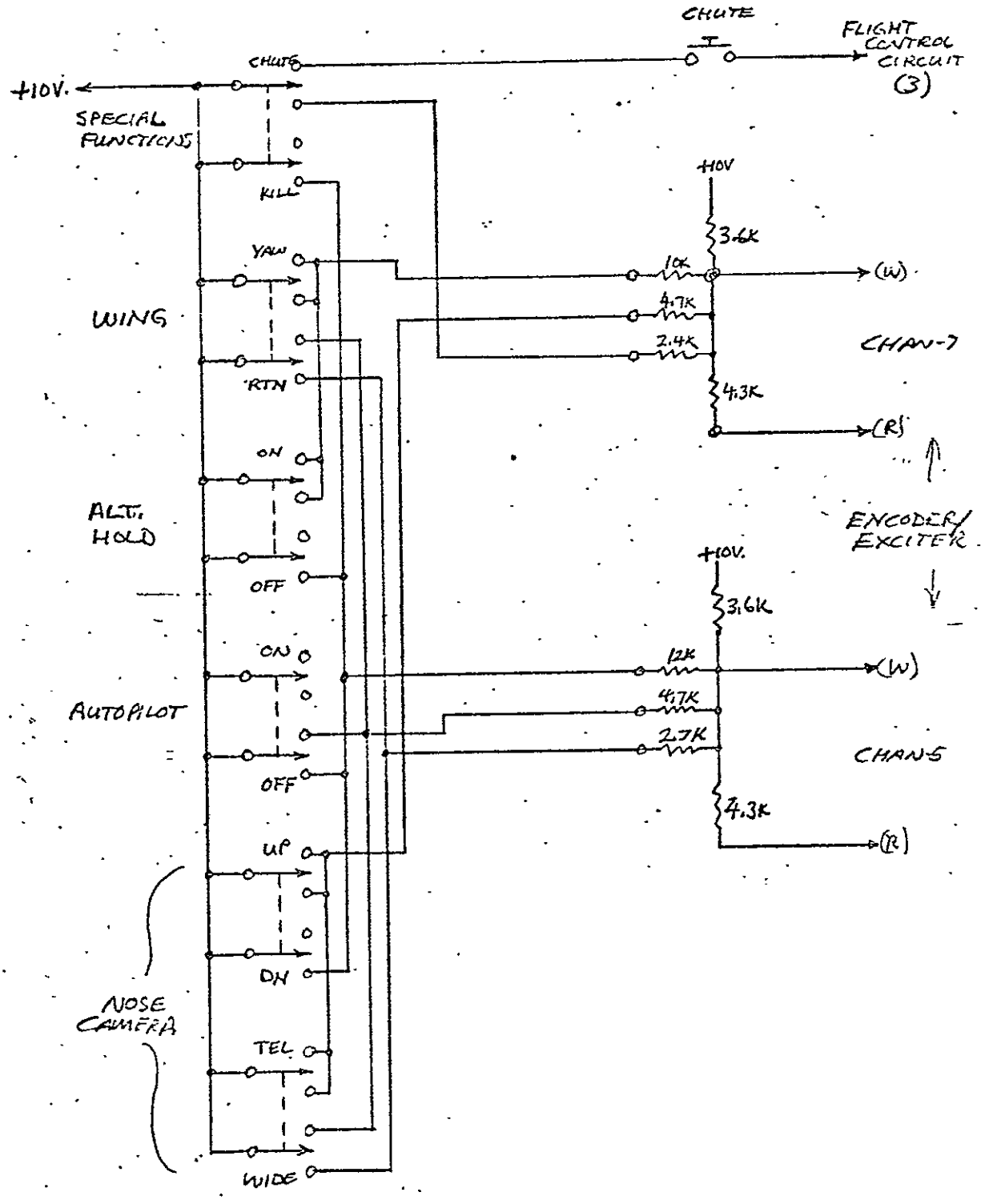

AUXILIARY SELECT PANEL

FIGURE 3.20

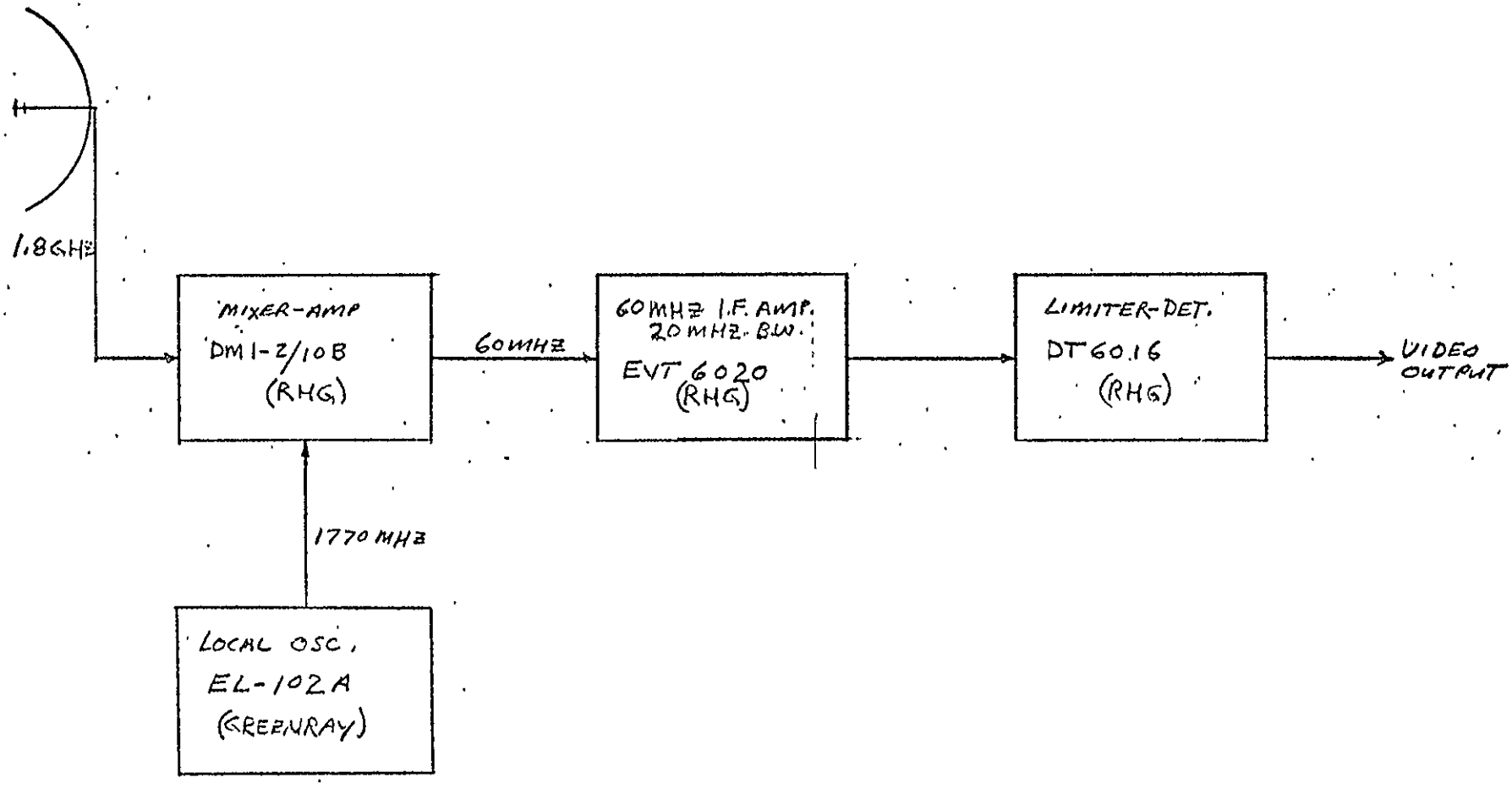

T. V. RECEIVER

FIGURE 3.21

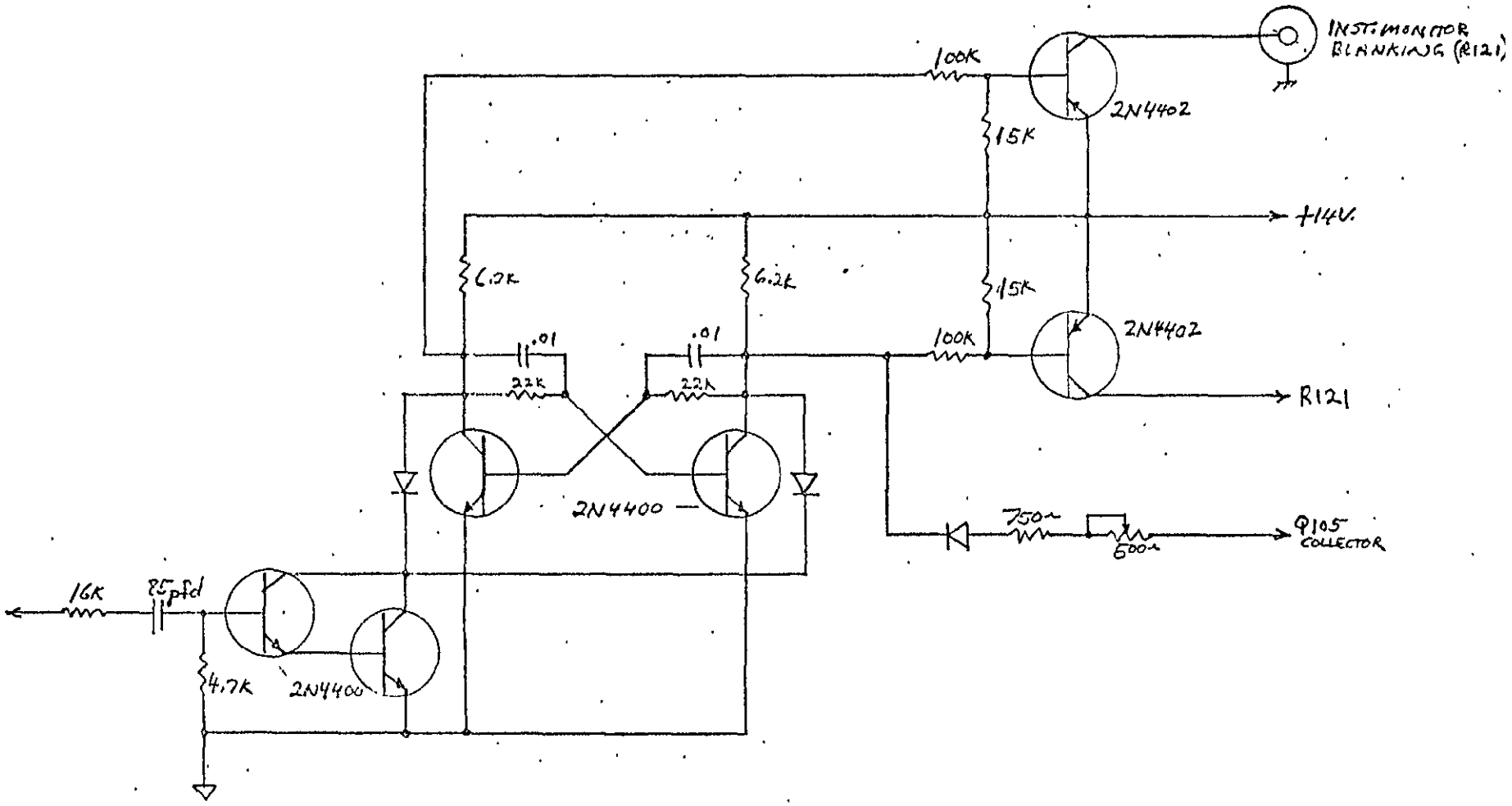

VIDEO DECODER
(NOSE MONITOR)

FIGURE 3.22

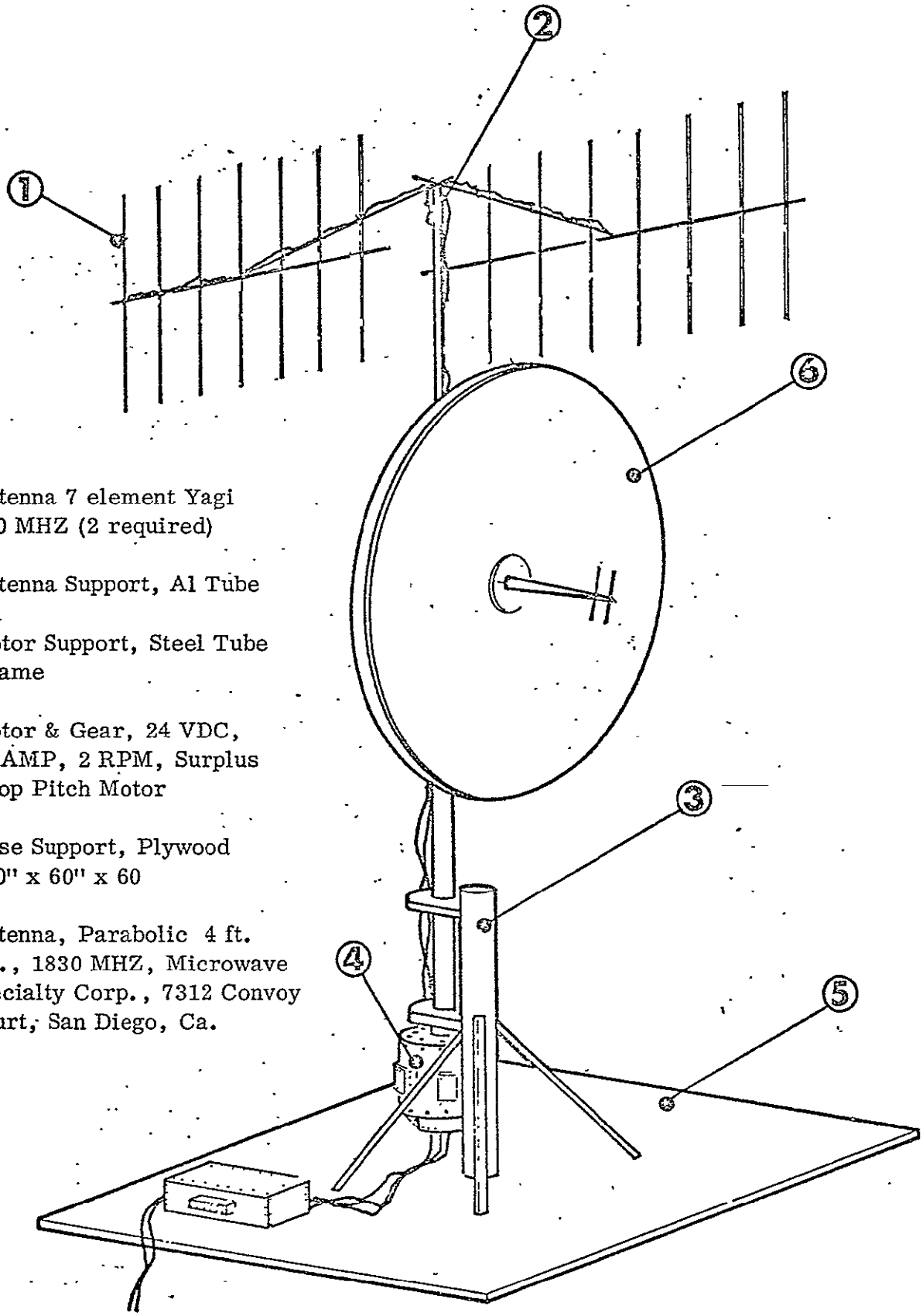

1. Antenna 7 element Yagi 240 MHZ (2 required)
2. Antenna Support, Al Tube
3. Motor Support, Steel Tube Frame
4. Motor & Gear, 24 VDC, 10 AMP, 2 RPM, Surplus Prop Pitch Motor
5. Base Support, Plywood 1.0" x 60" x 60
6. Antenna, Parabolic 4 ft. dia., 1830 MHZ, Microwave Specialty Corp., 7312 Convoy Court, San Diego, Ca.

TRACKING ANTENNA

FIGURE 3.23

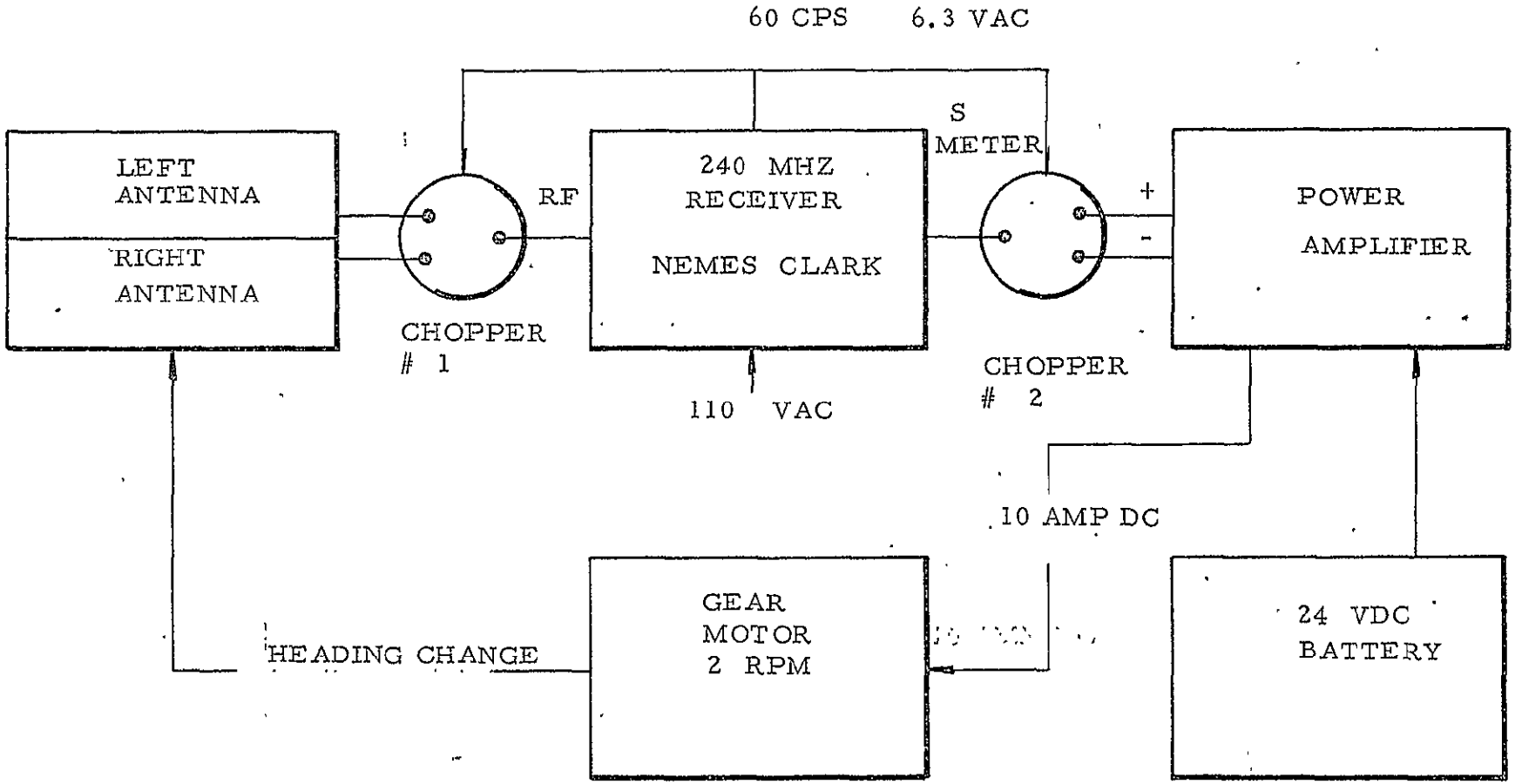

AIRCRAFT AUTO TRACKING BLOCK DIAGRAM

FIGURE 3.24

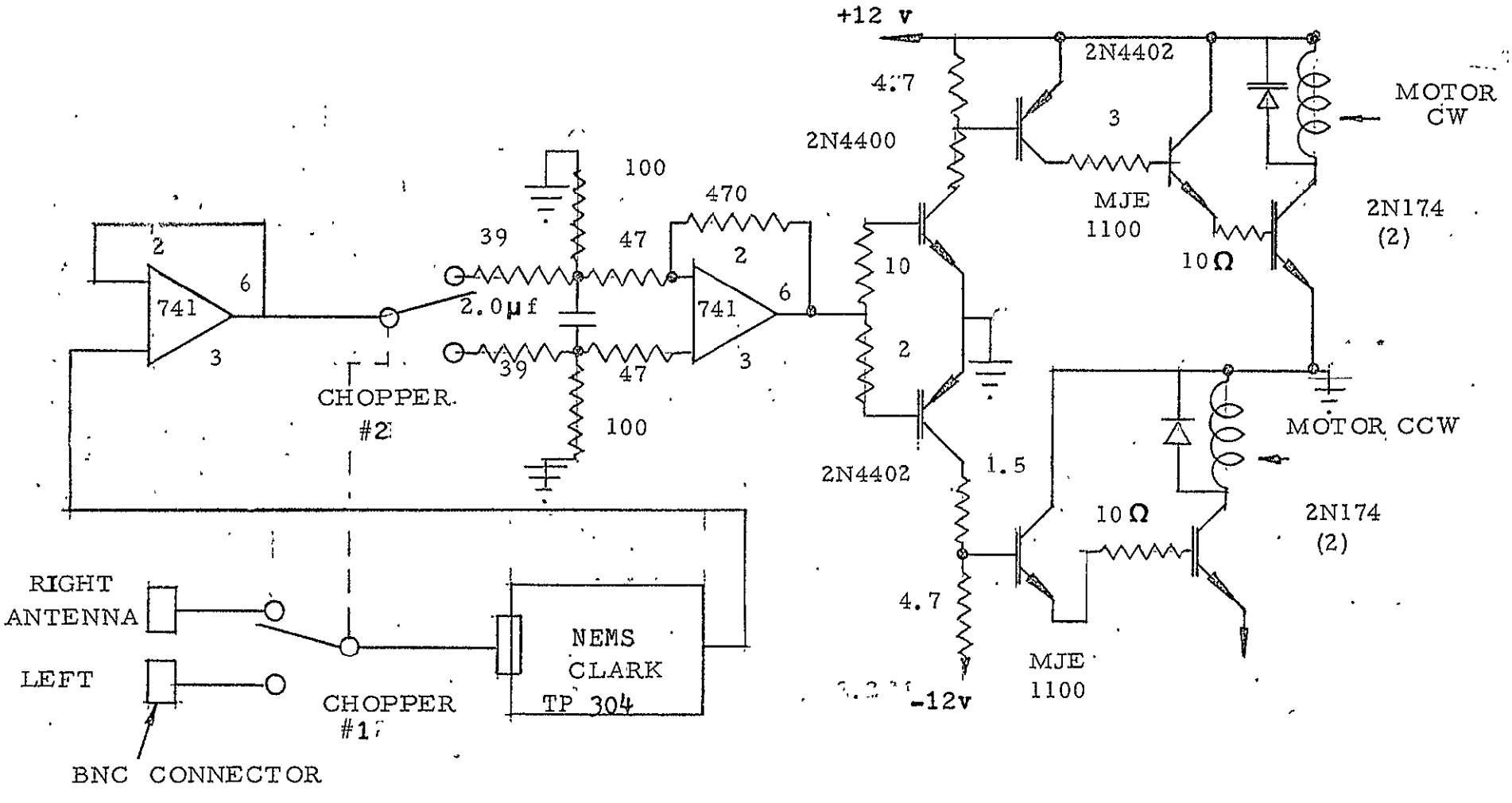

ALL RESISTOR IN
K Ω

TRACKING AMPLIFIER, 240 MHZ

FIGURE 3.25

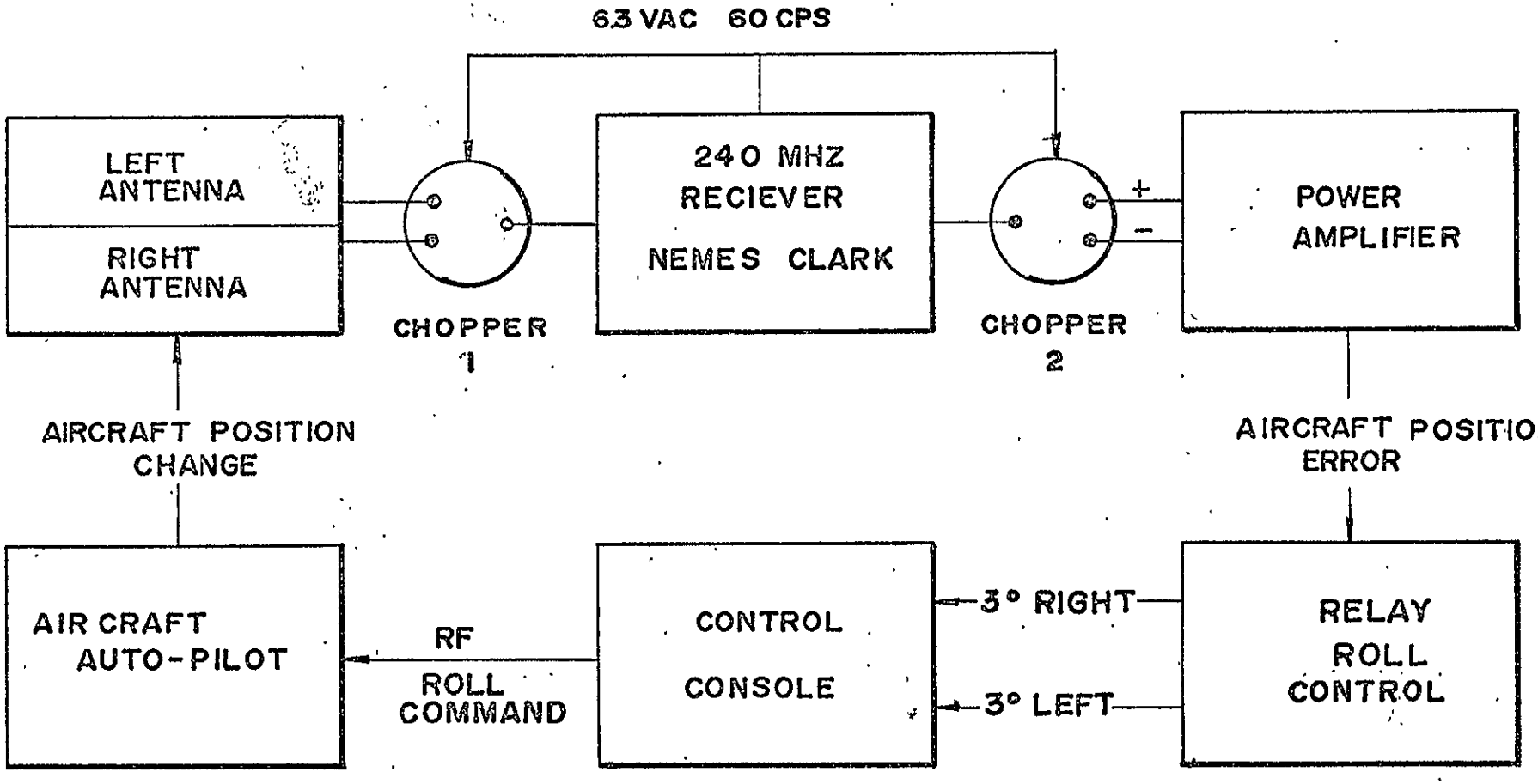

AIRCRAFT AUTO RETURN STEERING BLOCK DIAGRAM

FIGURE 3.26

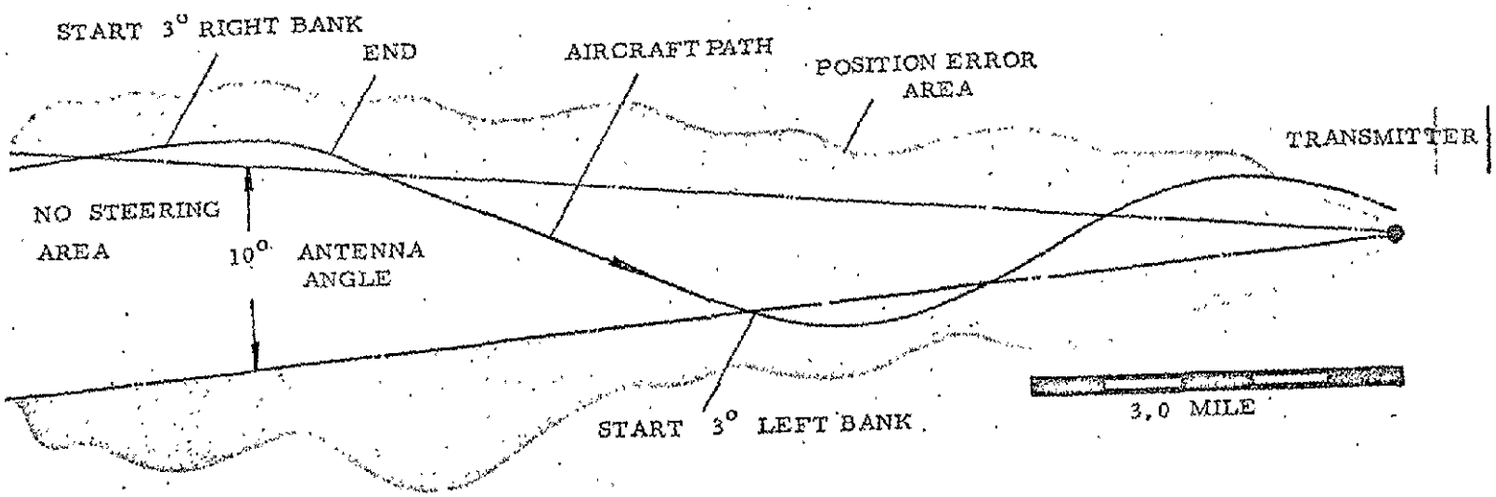

3° BANK ANGLE AT 100 MPH
TURN RADIUS 3 MILE

TYPICAL AIRCRAFT PATH, WITH AUTO RETURN STEERING

FIGURE 3.27

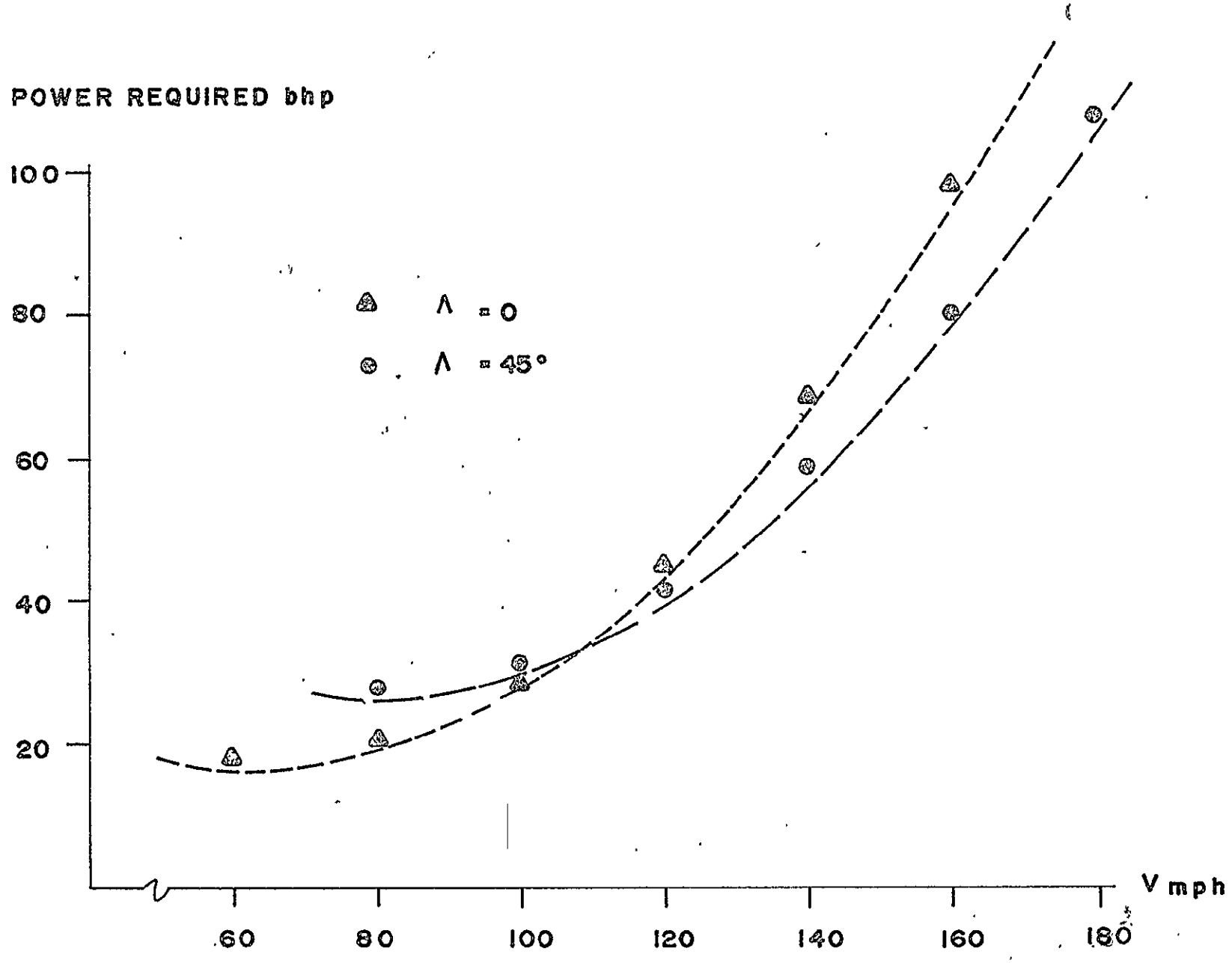

POWER REQUIRED

$\eta = 0.80$

FIGURE 5.1

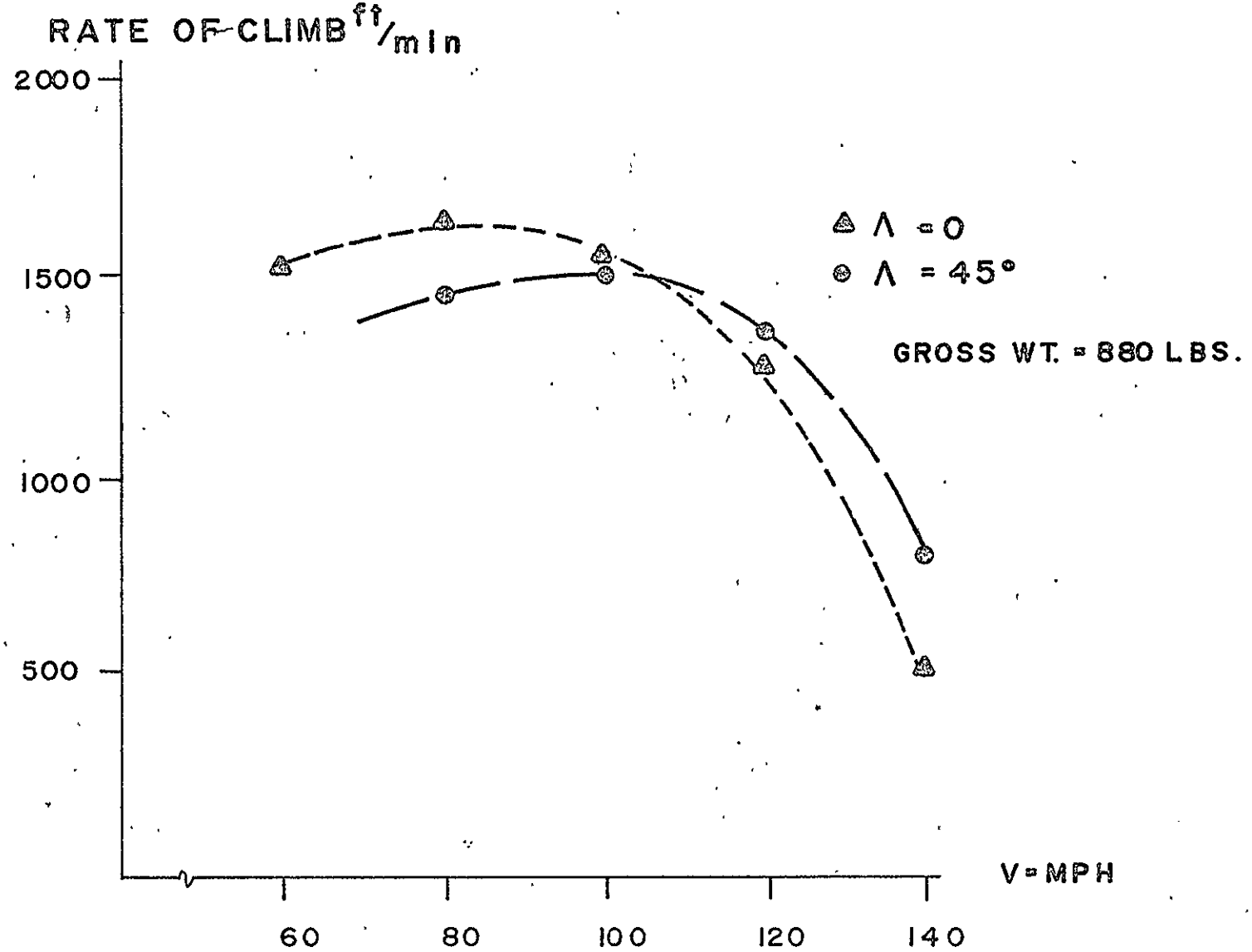

CLIMBING PERFORMANCE

FIGURE 5.2

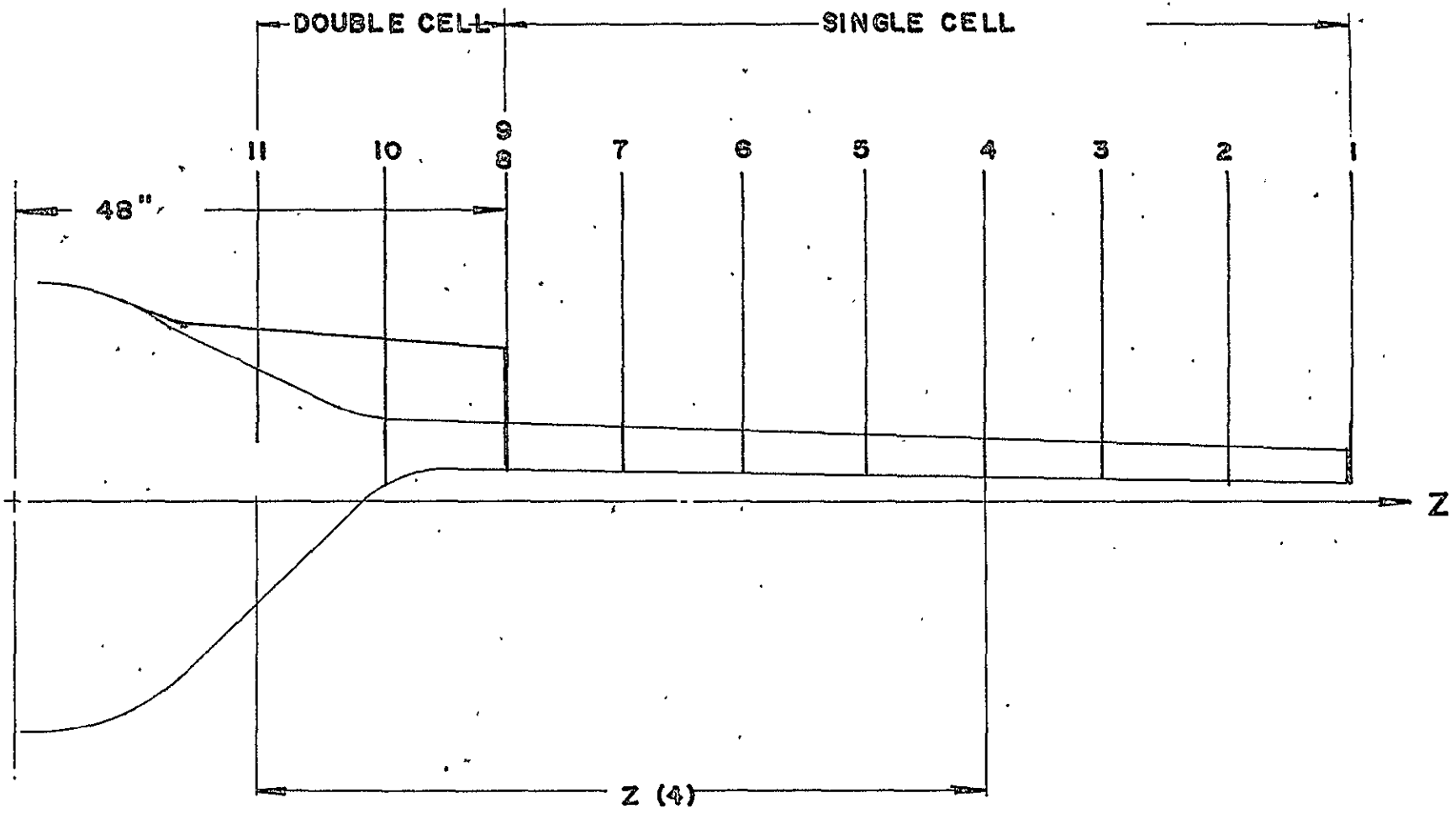

RING-SPAR LAYOUT

FIG. 6.1

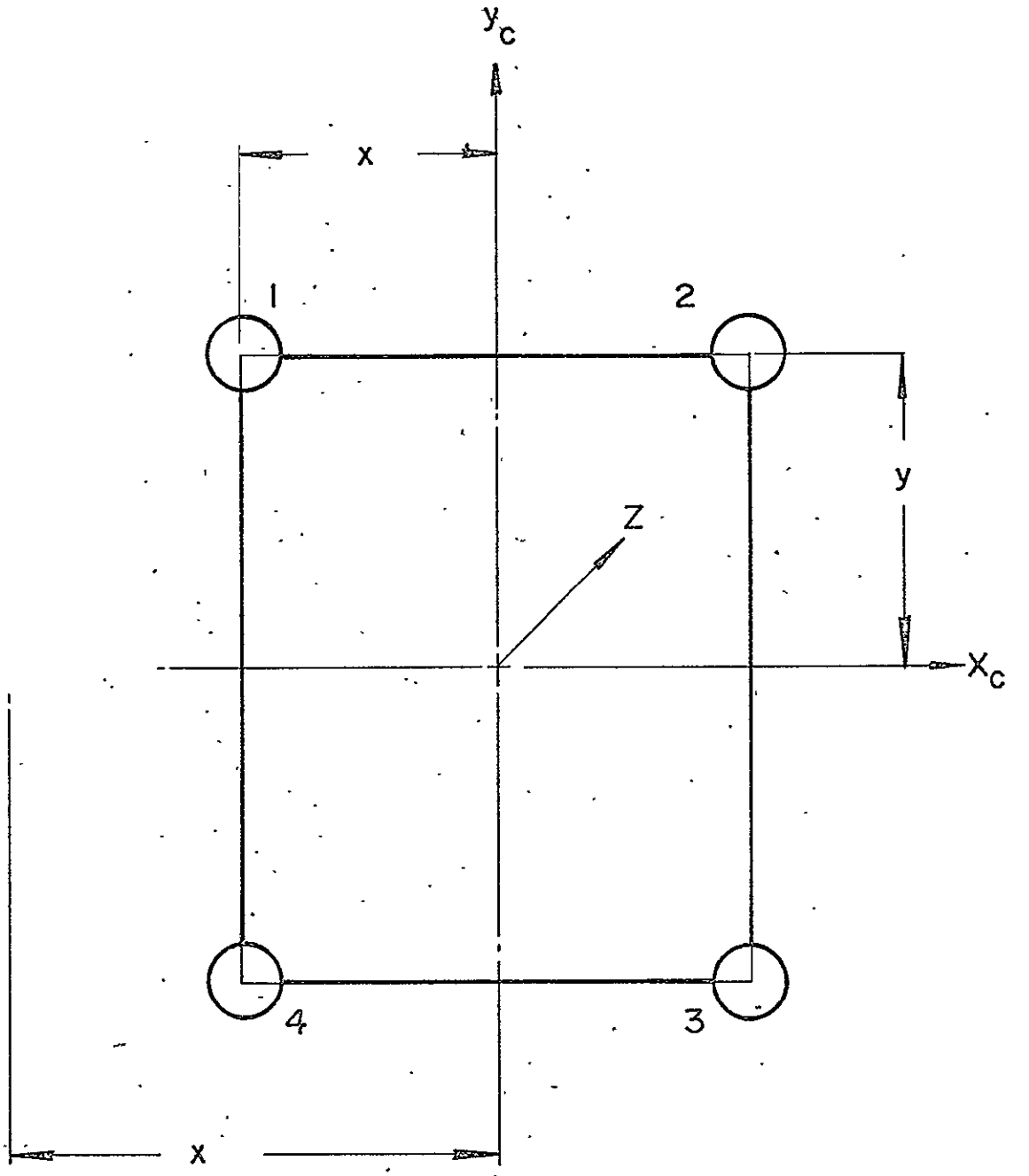

SINGLE CELL SECTIONS

FIG. 6.2

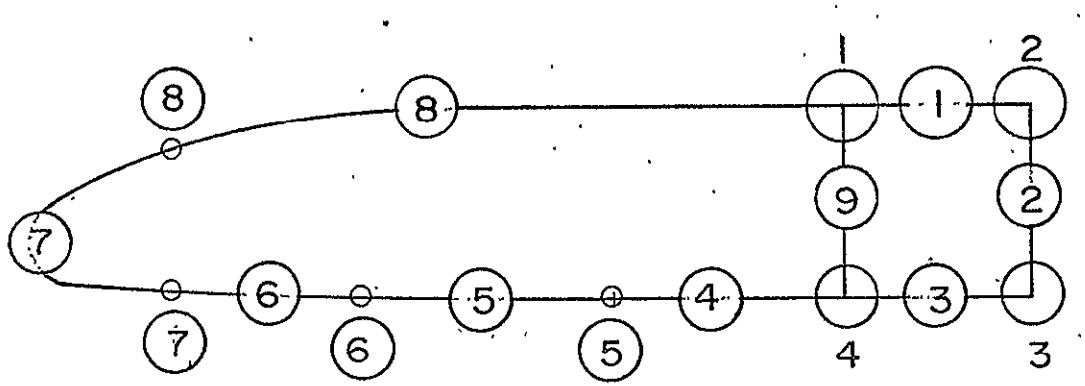

DOUBLE CELL SECTIONS

FIG. 6.3

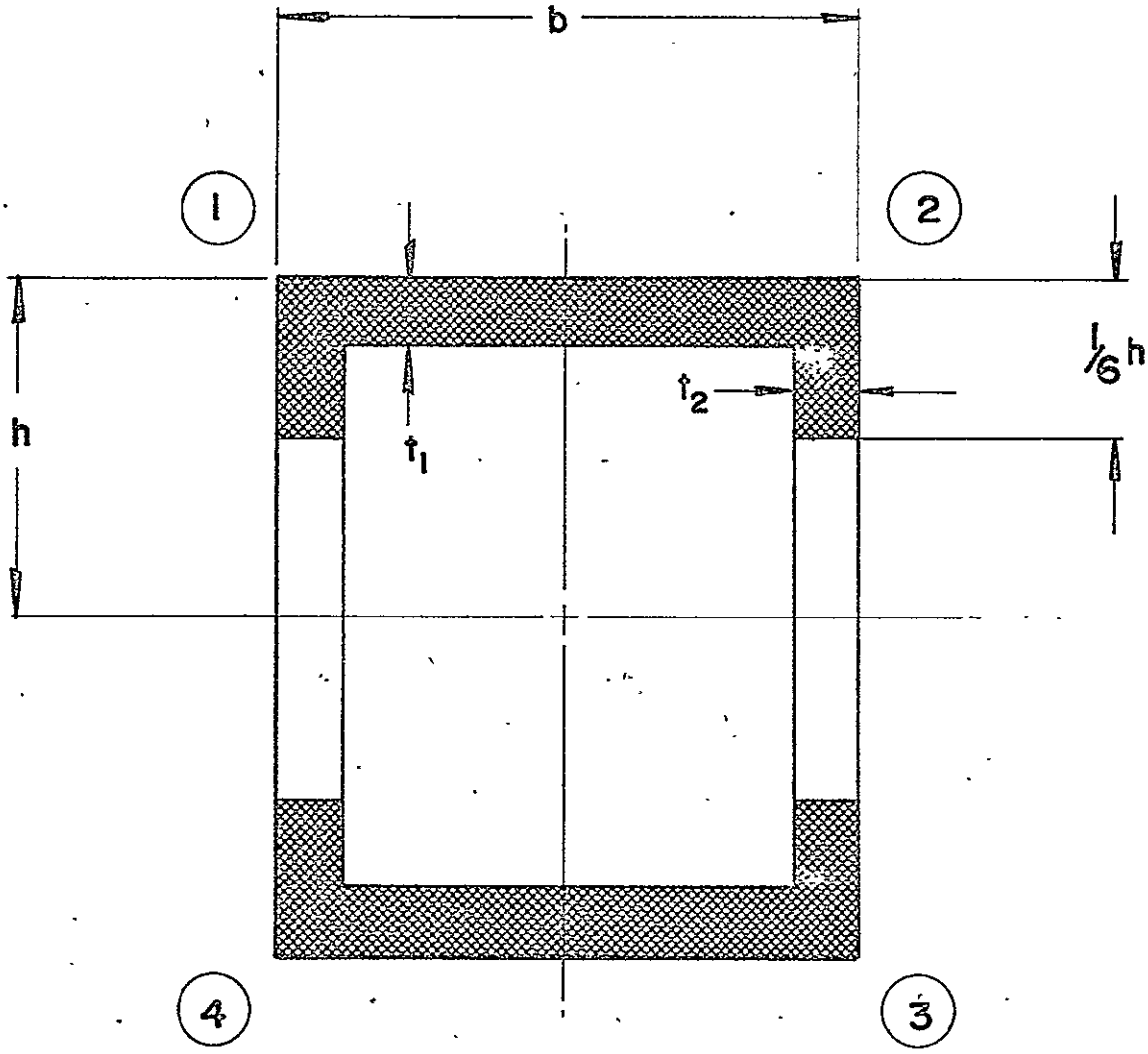

SPAR CAP GEOMETRY

FIG. 6.4

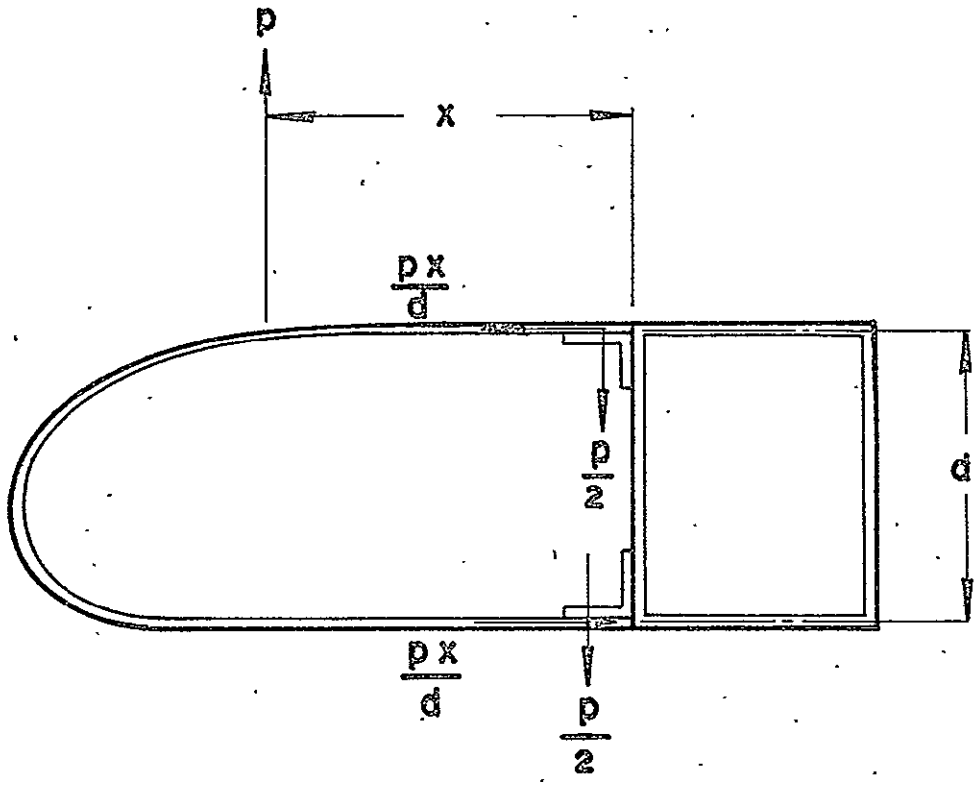

LEADING EDGE LOADS

FIG. 6.5

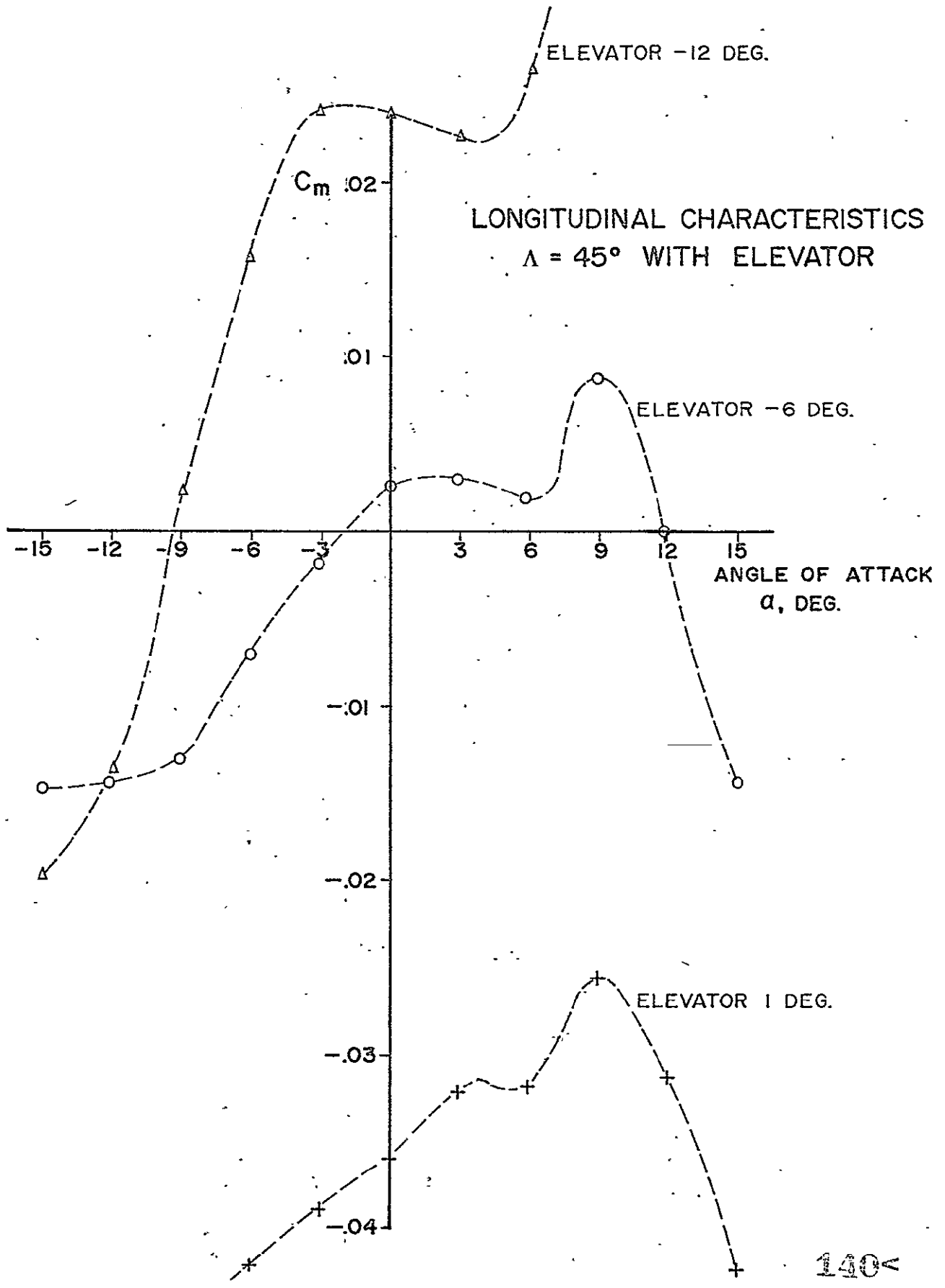
ELEVATOR −12 DEG.
C_m
.02
.01
−.01
−.02
−.03
−.04
LONGITUDINAL CHARACTERISTICS
Λ = 45° WITH ELEVATOR
ELEVATOR −6 DEG.
−15
−12
−9
−6
−3
3
6
9
12
15
ANGLE OF ATTACK
α, DEG.
ELEVATOR 1 DEG.

FIGURE 2.15 b

THE FOLLOWING PAGES ARE DUPLICATES OF ILLUSTRATIONS APPEARING ELSEWHERE IN THIS REPORT. THEY HAVE BEEN REPRODUCED HERE BY A DIFFERENT METHOD TO PROVIDE BETTER DETAIL